

# Analysis and Design of Conical Transmission Line Power Combiners

Dirk I.L. de Villiers



Dissertation presented for the degree of Doctor of Philosophy in Engineering at the  
University of Stellenbosch.

Promoters: Prof. P. Meyer and Prof. P.W. van der Walt  
December 2007

# Declaration

I, the undersigned, hereby declare that the work contained in this dissertation is my own original work and that I have not previously in its entirety or in part submitted it at any university for a degree.

D.I.L. de Villiers \_\_\_\_\_

Date \_\_\_\_\_

# Abstract

*Keywords* – Combiners, Radial Combiners, Conical Combiners, Conical Transmission Lines,  $N$ -way Combiners, Tapered Lines

This dissertation presents a technique for the design of  $N$ -way conical line power combiners, which offers significant advantages over existing axially symmetric combining techniques.

A full analytical study of conical transmission lines is done, and evaluated results are presented. These include a proof of the cutoff frequency equation, and plots of the field patterns, of higher order modes which are unavailable in literature.

A coaxial fed conical line combiner for 10 inputs is proposed, designed and evaluated. The design technique relies on the uniform transmission line characteristics of the conical lines to eliminate the need for complex full wave optimisation, typically needed in the design of the more commonly used radial line combiners. Circuit models are instead employed to achieve a wide matched bandwidth by using optimised stepped impedance coaxial lines to feed the combining structure. The prototype developed at  $X$ -band displays more than an octave bandwidth with a return loss of better than -14.5 dB. Using tapered line matching sections increases the power handling capability of the combiner by eliminating sharp edges, and allows for tolerance insensitive manufacture of the structure by widening conductor spacings. Such a 10-way prototype is developed at  $X$ -band which displays a -18.7 dB return loss bandwidth of 47% with very low losses.

A study is done to determine the limitations on the design of general  $N$ -way combiners, and the results are incorporated into the design technique. The full process is demonstrated by the design and simulation of a 30-way combiner at  $K_u$ -band which displays a simulated -20 dB return loss bandwidth of 34%.

The design technique is simple to execute and requires very little full wave analysis. Results obtained with the manufactured combiners are better than those of any previously published axially symmetric combiners.

# Opsomming

*Sleutelwoorde* – Kombineerders, Radiale Kombineerders, Koniese Kombineerders, Koniese Transmissielyne,  $N$ -rigting Kombineerders, Tapse Lyne

Hierdie proefskrif stel 'n tegniek voor vir die ontwerp van  $N$ -rigting koniese lyn kombineerders wat verskeie voordele bied bo bestaande aksiaal simmetriese kombinerings tegnieke.

'n Volledige analitiese studie van koniese transmissielyne word gedoen, en die berekende resultate word voorgelê. Dit sluit in 'n bewys vir die vergelyking van die afknipfrekwensie, sowel as plots van die veldpatrone, van die hoër orde modusse wat onbeskikbaar is in die literatuur.

'n Koaksiaal gevoerde koniese lyn kombineerder vir 10 intrees word voorgestel, ontwerp en getoets. Die ontwerp tegniek maak staat op die uniforme transmissielyn eienskappe van koniese lyne om komplekse volgolf optimering uit te skakel, wat tipies benodig word in die ontwerp van die meer algemeen gebruikte radiale kombineerders. 'n Wye bandwydte word verkry deur stroombaanmodelle van die trapwyse impedansie koaksiale lyne, wat die struktuur voer, te optimeer. Die ontwikkelde prototipe behaal meer as 'n oktaaf bandwydte by  $X$ -band, met 'n weerkaatskoeffisiënt van beter as -14.5 dB. Deur tapse lyn aanpassingsnetwerke in te span, word die drywingsvermoë van die struktuur verhoog deur skerp randte uit te skakel, en word voorsiening gemaak vir toleransie onafhanklike vervaardiging van die struktuur deur die spasieëring tussen die geleiers te verhoog. 'n Tien-rigting prototipe is ontwikkel by  $X$ -band wat 'n -18.7 dB weerkaatskoeffisiënt bandwydte van 47% behaal, met baie lae verliese.

Die ontwerp tegniek word verder uitgebrei deur 'n studie te doen van die beperkings van die tegniek op algemene  $N$ -rigting kombineerders. Die volledige proses word gedemonstreer deur die ontwerp en simulatie van 'n 30-rigting kombineerder by  $K_u$ -band, wat 'n gesimuleerde -20 dB weerkaatskoeffisiënt bandwydte van 34% behaal.

Die ontwerp tegniek is eenvoudig om uit te voer en vereis baie min volgolf analiese. Resultate bereik met die vervaardigde kombineerders is beter as die van enige vooraf gepubliseerde aksiaal simmetriese kombineerders.

# Acknowledgements

This work would not have been possible without the help and support of others, and I would like to express my deepest gratitude to:

- Professors Petrie Meyer and P.W. van der Walt, my promoters, for their unfailing support, leadership, encouragement, advice, and insight throughout the course of this project.
- My mother for always lending an interested ear and an encouraging word whether or not she understood the deeper intricacies of the problem - be it an engineering problem, girl problem or washing stain problem!
- My father for teaching me the valuable lesson of first getting the ball near the hole before you try to get it in the hole, without which I would probably still be struggling with some small negligible little problem and missing the big picture...
- Stephanie Zietsman for her loyal friendship and handy obsession with English spelling and grammar rules for the proofreading.
- Kristiaan Schreve for his help with the drawings of the first prototype.
- Wessel Crouwkamp and Ulrich Büttner for their valuable advice and help with the manufacturing of the prototypes.
- Computer Simulation Technology and Applied Wave Research for the use of their software licences.
- The Wilhelm Frank Trust and Reutech Radar Systems for financial support of the project.
- Everyone who has shared the office over the last three years, Thomas, Nicola, Marlize, Shaun, Parick, Tinus, André, and Madelé for their friendship, advice and contributions.
- All my friends for being my friends who I can laugh with and moan to in the good times and the bad...

# Contents

<b>List of Tables</b>	<b>ix</b>
<b>List of Figures</b>	<b>x</b>
<b>1 Introduction</b>	<b>1</b>
1.1 Background on Axially Symmetric Combiners . . . . .	1
1.2 About the Dissertation . . . . .	3
1.3 Layout of the Dissertation . . . . .	4
<b>2 Theoretical Analysis of Conical Transmission Lines</b>	<b>6</b>
2.1 Physical Description of a Conical Transmission Line . . . . .	7
2.2 Wave Equation and Solution in Spherical Coordinates . . . . .	7
2.2.1 Direct Approach . . . . .	7
2.2.2 Solutions Using Vector Potentials . . . . .	9
2.2.3 Transverse Electric and Magnetic Solutions . . . . .	10
2.3 Conical Transmission Line Boundary Conditions . . . . .	14
2.3.1 Transverse Electric Modes . . . . .	15
2.3.2 Transverse Magnetic Modes . . . . .	17
2.3.3 Transverse Electromagnetic Modes . . . . .	18
2.4 Associated Legendre Function and Transcendental Equation Solutions . . . . .	20

2.4.1	Use of the Associated Legendre Function of the Second Kind in the Transcendental Equations . . . . .	21
2.4.2	Solving the Associated Legendre Functions . . . . .	22
2.4.3	Solving the Transcendental Equations . . . . .	25
2.5	Modal Cutoff Frequencies . . . . .	26
2.5.1	Definition of Cutoff Wavelength . . . . .	26
2.5.2	Numerical Results . . . . .	30
2.6	Modal Plots . . . . .	32
2.6.1	Travelling Wave Solutions . . . . .	32
2.6.2	Standing Wave Solutions . . . . .	34
2.7	Conclusion . . . . .	39
<b>3</b>	<b>A Basic 10-Way Conical Line Combiner</b>	<b>42</b>
3.1	Ideal $N$ -way TEM Combiners . . . . .	42
3.2	Basic Configuration of the Structure . . . . .	44
3.3	Central Conical to Coaxial Transition . . . . .	45
3.4	Peripheral Input Port Feeds . . . . .	49
3.5	Input and Output Matching Networks . . . . .	51
3.5.1	Input Matching Section . . . . .	53
3.5.2	Output Matching Section . . . . .	54
3.6	Summary of the Step-by-Step Design Procedure . . . . .	56
3.7	Construction and Measurement . . . . .	57
3.8	Isolation . . . . .	61
3.9	Electric Field Strength and Peak Power Considerations . . . . .	63
3.10	Conclusion . . . . .	65

<b>4</b>	<b>Design of a 10-Way Tapered Line Combiner</b>	<b>66</b>
4.1	Peripheral Input Port Feeds and Matching . . . . .	67
4.2	Conical Line Design . . . . .	69
4.2.1	Determination of Maximum Conical Line Length . . . . .	69
4.2.2	Design of the Klopfenstein Taper . . . . .	71
4.2.3	Higher Order Mode Cutoff Frequencies . . . . .	75
4.2.4	Simulation of the Combining Structure . . . . .	76
4.3	Central Output Port Matching . . . . .	78
4.3.1	Transmission Matrix Modelling . . . . .	78
4.3.2	Coaxial Taper Optimisation . . . . .	79
4.4	Summary of the Step-by-Step Design Procedure . . . . .	80
4.5	Construction and Measurement . . . . .	83
4.6	Isolation . . . . .	86
4.7	Electric Field Strength and Peak Power Considerations . . . . .	88
4.8	Conclusion . . . . .	90
<b>5</b>	<b>General Design Strategy</b>	<b>91</b>
5.1	Effect of Size Variations in a Constant Impedance Combining Structure . . . . .	91
5.1.1	Effects of Varying Size on the Reflection Coefficient . . . . .	92
5.1.2	Effects of Varying Size on the Transmission Coefficient . . . . .	96
5.2	Effect of Different Impedance Matching Tapers in the Conical Line of the Combining Structure . . . . .	98
5.2.1	Effect of Tapers in Electrically Small Structures . . . . .	99
5.2.2	Effect of Tapers in Electrically Large Structures . . . . .	101
5.3	Effect of the First Order Peripheral Input Port Matching Sections . . . . .	102
5.3.1	Effect of First Order Input Match on Electrically Small Combiners . . . . .	102

5.3.2 Effect of First Order Input Match on Electrically Large Combiners . . . . 103

5.4 Summary of General Design Guidelines and Critical Evaluation of Previous Designs 105

5.4.1 Summary of General Design Guidelines . . . . . 105

5.4.2 Critical Evaluation of Previous Designs . . . . . 106

5.5 Design and Simulation of a 30-Way Combiner . . . . . 107

5.6 Conclusion . . . . . 111

**6 Conclusion 113**

**A Derivatives of Some Special Functions 115**

A.1 Derivatives of the Associated Legendre Functions . . . . . 115

A.2 Derivatives the Modified Spherical Bessel Functions . . . . . 115

**Bibliography 117**

# List of Tables

2.1	TE <sub><i>m</i>1</sub> transcendental equation roots showing cutoff wavelengths occur when circumference is approximately an integral number of wavelengths. . . . .	33
2.2	Comparison of analytical and simulated results for the resonant frequencies of the first fourteen modes in a conical cavity. . . . .	39
5.1	Comparison of the theoretical quarter wavelength backshort reflection zero frequency with the simulated value in an 8 Ω 10-way combiner for small values of <i>r<sub>p</sub></i> . . . . .	93
5.2	Comparison of the theoretical quarter wavelength backshort reflection zero frequency with the simulated value in a 5 Ω 16-way combiner for small values of <i>r<sub>p</sub></i> . . . . .	93
5.3	Comparison of the cutoff radius of the TE <sub><i>N</i>/2,1</sub> mode at the theoretical centre frequency of the structure to the total size of the structure at the <i>S</i> <sub>11</sub> transition point. . . . .	95
5.4	Comparison of the theoretical half wavelength backshort transmission zero frequency with the simulated value in an 8 Ω 10-way combiner. . . . .	98

# List of Figures

2.1	Geometry of a conical transmission line. . . . .	7
2.2	Characteristic impedance of a conical line versus cone half-angles. . . . .	20
2.3	Comparison of the computed results of the Legendre function of the first kind using a recursive scheme to those found without using recursion. . . . .	24
2.4	Comparison of the P- and mixed-type transcendental functions for $m = 1$ , $\theta_1 = 85.23^\circ$ and $\theta_2 = 90^\circ$ . . . . .	25
2.5	Normalised TE wave impedance of a conical transmission line. . . . .	28
2.6	Normalised cutoff wavelength of higher order modes in a conical transmission line with $\theta_2 = 10^\circ$ . . . . .	31
2.7	Normalised cutoff wavelength of higher order modes in a conical transmission line with $\theta_2 = 22.5^\circ$ . . . . .	31
2.8	Spatial variation of cutoff frequencies for the first 15 $TE_{m1}$ modes in a $5 \Omega$ conical line with $\theta_2 = 90^\circ$ . . . . .	33
2.9	Variation of the $\theta$ dependent factors of the $TE_{21}$ modal fields close to $\theta = 90^\circ$ . . . . .	34
2.10	Normalised absolute value (in dB) of the TEM modal fields at 10 GHz. . . . .	35
2.11	Normalised absolute value (in dB) of the $TE_{11}$ E-field at 10 GHz. . . . .	35
2.12	Normalised absolute value (in dB) and direction of the $TE_{11}$ H-field at 10 GHz. . . . .	36
2.13	Normalised absolute value (in dB) of the $TE_{21}$ E-field at 10 GHz. . . . .	36
2.14	Normalised absolute value (in dB) and direction of the $TE_{21}$ H-field at 10 GHz. . . . .	37
2.15	Normalised absolute value (in dB) of the $TE_{51}$ E-field at 10 GHz. . . . .	37
2.16	Normalised absolute value (in dB) and direction of the $TE_{51}$ H-field at 10 GHz. . . . .	38

2.17	Normalised absolute value of the E-field of the $TM_{001}$ mode at 3.00 GHz. . . . .	40
2.18	Normalised absolute value of the E-field of the $TE_{211}$ mode at 4.98 GHz. . . . .	40
2.19	Normalised absolute value of the E-field of the $TE_{312}$ mode at 9.37 GHz. . . . .	41
2.20	Normalised absolute value of the E-field of the $TE_{113}$ mode 9.88 GHz. . . . .	41
3.1	Simplified transmission line model of a reactive $N$ -way combiner. . . . .	43
3.2	Cutoff frequency of first three higher order modes in a $5 \Omega$ conical transmission line. . . . .	44
3.3	Error in $Z_0$ as a function of $\theta_2$ with a $0.5^\circ$ error in $\theta_1$ . . . . .	45
3.4	Basic configuration of the power combiner. . . . .	46
3.5	10-Way combiner port position and numbers. . . . .	46
3.6	Construction of conical to coaxial transition profile. . . . .	47
3.7	Reflection from conical/coaxial transitions. . . . .	49
3.8	Electric field size in the conical/coaxial transitions at 10 GHz with an input power of 1 W and $R_1 = 3.22$ mm and $R_2 = 3.5$ mm. . . . .	50
3.9	CST-MWS screen shot of 10-way power combiner showing central conical to coaxial transition and peripheral feeding probes. The background material as well as the grey parts are perfect electrical conductors (PEC), the blue part is vacuum, and the yellow parts are teflon. Ports are represented by red rectangles. . . . .	52
3.10	CST-MWS simulation of 10-way power combiner common central port reflection coefficient. . . . .	52
3.11	Schematic representation of circuit to be optimised in MWO. . . . .	52
3.12	Sketch of an extended dielectric SMA connector inserted into the top of the metal structure to form two short transmission lines. . . . .	53
3.13	Stepped impedance coaxial line feeding the conical line. . . . .	55
3.14	Simulated reflection coefficient of matched 10-way conical power combiner. . . . .	56
3.15	Rounded corner detail of the conical line. . . . .	57

3.16	CST-MWS simulation reflection coefficient of matched 10-way combiner with rounded corner. . . . .	57
3.17	2-D section view of the conical combiner showing all connectors, feeding probes and fastening screws. . . . .	58
3.18	Photographs of the constructed 10-way combiner. . . . .	59
3.19	Comparison between the simulated and measured reflection coefficient of a 10-way combiner. . . . .	60
3.20	Measured transmission coefficients in the operating band of a 10-way combiner ( $S_{n1}$ with $n = 2, 3, \dots, 11$ ). . . . .	60
3.21	Simulated and measured isolation in the operating band of a 10-way combiner. . . . .	60
3.22	Measured loss of a 10-way combiner. . . . .	61
3.23	Normalised absolute value (in dB) and direction of the simulated H-field at zero-time in a 10-way conical combiner at 10 GHz when port 2 (see Fig. 3.5) is driven and the other ports are terminated. . . . .	62
3.24	Normalised absolute value (in dB) of the time averaged simulated H-field in a 10-way conical combiner at 10 GHz when port 2 (see Fig. 3.5) is driven and the other ports are terminated. . . . .	63
3.25	2-D section view of the normalised magnitude (in dB relative to 12.3 kV/m) of the TEM E-field in a 10-way combiner at 10 GHz with 1 W of input power. . . . .	64
3.26	Magnitude of the TEM E-field along a curve on the surface of the inner conductor of the central line from the central output port to one of the peripheral input ports of a 10-way stepped impedance combiner at 10 GHz with 1 W of input power. . . . .	65
4.1	Sketch of an extended dielectric SMA connector inserted into the top of the metal structure forming the peripheral feeding line matching network. . . . .	67
4.2	MWO simulated reflection coefficient looking into an $80 \Omega$ line matched to a $50 \Omega$ load through a quarter wavelength $60.1 \Omega$ partially filled coaxial line. . . . .	68
4.3	Transmission coefficient of an $8 \Omega$ 10-way combiner showing the transmission zero effect with changing dimensions. . . . .	70

4.4	Normalised amplitude of the electric field patterns in an $8 \Omega$ combiner at the transmission zero frequency, and an eigenmode of a similar $8 \Omega$ conical transmission line with peripheral feeding probes inserted. . . . .	70
4.5	Characteristic impedance of a 20 mm Klopfenstein taper matching an $8 \Omega$ load to a $25 \Omega$ line. . . . .	73
4.6	2-D profile of the ideal and linear approximated smoothed Klopfenstein taper in a conical line without a central conical to coaxial transition. The red part is the ideal taper, and the black part the linear approximated smooth taper. . . . .	74
4.7	2-D profile showing the smoothed edge of the conical line Klopfenstein taper. The red part is the ideal taper, and the black part the linear approximated smooth taper. . . . .	74
4.8	Comparison of the reflection coefficients of an ideal and a smoothed Klopfenstein taper, as well as an ideal Hecken taper. . . . .	74
4.9	Spatial variation of the cutoff frequency of the first 4 $TE_{m1}$ modes in a Klopfenstein tapered conical line. . . . .	75
4.10	Spatial variation of the cutoff frequency of the first few modes with electric field variations in the $\theta$ -direction in a Klopfenstein tapered conical line. . . . .	76
4.11	CST-MWS screen shot of tapered 10-way combiner showing central conical to coaxial transition and peripheral feeding lines and ports. The background material as well as the grey parts are PEC, the blue part is vacuum, and the yellow parts are teflon. Ports are represented by red rectangles. . . . .	77
4.12	CST-MWS simulated results of the combining structure. . . . .	77
4.13	Schematic representation of optimisation model for tapered central output line matching section. . . . .	78
4.14	2-D profile of the coaxial taper showing optimisation variables. . . . .	80
4.15	Comparison of the simulated reflection coefficients of a matched 10-way tapered line conical power combiner. . . . .	81
4.16	MATLAB generated 2-D profile of the final coaxial taper showing optimisation variable positions. . . . .	81
4.17	2-D section view of the tapered line conical combiner showing all connectors, feeding probes and fastening screws. . . . .	83

4.18	Photographs of the constructed 10-way tapered line combiner. . . . .	84
4.19	Comparison between the simulated and measured reflection coefficient of a tapered line 10-way combiner. . . . .	85
4.20	Measured transmission coefficients in the operating band of a tapered line 10-way combiner ( $S_{n1}$ with $n = 2, 3, \dots, 11$ ). . . . .	85
4.21	Simulated and measured isolation in the operating band of a tapered line 10-way combiner. . . . .	86
4.22	Measured loss in the operating band of a tapered line 10-way combiner. . . . .	86
4.23	Normalised absolute value (in dB) and direction of the simulated H-field pattern at zero-time in a 10-way tapered line conical combiner at 10 GHz when port 2 (see Fig. 3.5) is driven and the other ports are terminated. . . . .	87
4.24	Normalised absolute value (in dB) of the time averaged simulated H-field pattern in a 10-way tapered line conical combiner at 10 GHz when port 2 (see Fig. 3.5) is driven and the other ports are terminated. . . . .	88
4.25	2-D section view of the normalised magnitude (in dB relative to 5.7 kV/m) of the TEM E-field in a 10-way tapered line combiner at 10 GHz with 1 W of input power. . . . .	89
4.26	Comparison of the magnitudes of the TEM E-fields, evaluated along a curve on the surface of the inner conductor of the central line from the central output port to one of the peripheral input ports, of a 10-way tapered line combiner with a 10-way stepped impedance combiner at 10 GHz with 1 W of input power. . . . .	89
5.1	Simulated reflection coefficients of several $8 \Omega$ 10-way combiners of different radial sizes and backshort lengths. . . . .	92
5.2	Simulated reflection coefficients of several $5 \Omega$ 16-way combiners of different sizes and backshort lengths. . . . .	94
5.3	Simulated reflection coefficients of several $4 \Omega$ 20-way combiners of different sizes and backshort lengths. . . . .	95
5.4	Simulated transmission coefficients of several $8 \Omega$ 10-way combiners of different radial sizes and backshort lengths. . . . .	97

5.5	Normalised absolute value of the electric field at the resonant transmission zero frequency (17.1 GHz) of an electrically large 16-way combiner with $r_p = 50$ mm and $r_b = 7.5$ mm. . . . .	99
5.6	Reflection coefficients of electrically small ( $r_p = 30.7$ mm and $r_b = 7.5$ mm) 15 $\Omega$ common port 16-way combiners with varying return loss conical line impedance tapers. . . . .	100
5.7	Reflection coefficients of electrically small ( $r_p = 30.7$ mm and $r_b = 6.3$ mm) 15 $\Omega$ common port 16-way combiners, tuned to 10 GHz, with varying return loss conical line impedance tapers. . . . .	100
5.8	Reflection coefficients of electrically large ( $r_p = 31.5$ mm and $r_b = 7.5$ mm) 25 $\Omega$ common port 10-way combiners with varying return loss conical line impedance tapers. . . . .	101
5.9	Reflection coefficients of electrically large ( $r_p = 31.5$ mm and $r_b = 8.5$ mm) 25 $\Omega$ common port 10-way combiners, tuned to about 10 GHz, with varying return loss conical line impedance tapers. . . . .	102
5.10	Comparison of the reflection coefficients caused by adding non-ideal and ideal first order input matching sections to an electrically small ( $r_p = 35$ mm and $r_b = 6.5$ mm) 20-way combiner containing a -27 dB conical line taper. . . . .	103
5.11	Comparison of reflection coefficients caused by adding non-ideal first order matching sections to an electrically large ( $r_p = 31.5$ mm) 10-way combiner, containing a -28 dB conical line taper, for different backshort lengths. . . . .	104
5.12	Comparison of reflection coefficients caused by adding ideal first order matching sections to an electrically large ( $r_p = 31.5$ mm) 10-way combiner, containing a -28 dB conical line taper, for different backshort lengths. . . . .	104
5.13	CST-MWS screen shot of tapered 30-way combiner showing central conical to coaxial transition and peripheral feeding lines and ports. The background material as well as the grey parts are PEC, the blue part is vacuum, and the yellow parts are teflon. Ports are represented by red rectangles. . . . .	108
5.14	Common central port reflection coefficient of a tapered 30-way combiner with the peripheral input matching sections included. . . . .	108
5.15	Comparison of the simulated reflection coefficients of a matched 30-way tapered line conical power combiner. . . . .	109

5.16	Simulated transmission coefficient of a 30-way conical line combiner. . . . .	110
5.17	Simulated minimum isolation between port 2 and port $n$ in the band 10.5–14.5 GHz of a 30-way conical combiner. The same port numbering convention is used as in Fig. 3.5. . . . .	110
5.18	Normalised absolute value (in dB) and direction of the simulated H-field at zero-time in a 30-way tapered line conical combiner at 12.5 GHz when port 2 (see Fig. 3.5) is driven and the other ports are terminated. . . . .	111
5.19	Normalised absolute value (in dB) of the time averaged simulated H-field in a 30-way tapered line conical combiner at 12.5 GHz when port 2 (see Fig. 3.5) is driven and the other ports are terminated. . . . .	112

# Chapter 1

## Introduction

### 1.1 Background on Axially Symmetric Combiners

Due to the vast improvement of the power output capability of solid state amplifiers in the microwave frequency range, there has been considerable interest in recent years in finding highly efficient and scalable approaches to combining the signals from a large number of such amplifiers. Such a system of several combined solid state amplifiers can be used as a substitute for travelling wave tube (TWT) amplifiers which are bulky, difficult to bias, and expensive. Also, when several solid state amplifiers are used in an amplification system, and one or more of these fail, the system could still be operable, whereas if a TWT is used and it fails, complete system failure will occur.

Power combiners can typically be divided into three broad classes, ie. corporate combiners, chain combiners, and axially symmetric or  $N$ -way combiners [1, 2]. Axially symmetric power combiners offer a number of advantages over the corporate or chain-type combiners, especially for a large number of combining ports ( $N \geq 8$ ); the most important being lower loss and smaller size due to the minimisation of path lengths, and improved amplitude and phase balance due to the symmetry [3]. Axially symmetric combiners include all combining structures in which the feed ports are placed symmetrically around a central output port, and can be implemented as radial lines, coaxial lines, planar lines, and as presented in this work, conical lines. Of these, planar line types exhibit substantially higher loss and lower power handling capability than the other three, and will not be considered further.

In radial combiners, the energy travels in the radial direction between the central port and the axially symmetric peripheral ports within a cylindrical parallel plate transmission line (radial line). Radial line combiners have been thoroughly investigated in the literature, and several computer algorithms and strategies for their analysis and design have been developed. These design strategies include design using simplified circuit models of the structure [4], electromag-

netic (EM) field analysis of the structure [5], and combinations of these two methods [3, 6]. Several microwave radial combiners have been reported, including 30-way combiners built at 12.5 GHz demonstrating a 25% bandwidth with a return loss of around -13 dB [3, 7], a 20-way combiner built at 14 GHz demonstrating a 57% bandwidth with a -17 dB return loss [5], and 8- and 16-way combiners built at 10 GHz demonstrating -20 dB return loss bandwidths of respectively 33% and 25% [6]. The combiners in [6] use a conical line in the transition between the central coaxial line and the radial line.

The main problem with a radial line is that, although it supports a dominant transverse electromagnetic (TEM) mode, the impedance of this mode varies strongly with radius, forming a non-uniform transmission line [8, 9]. Because of this radial dependence, the input impedance is not equal to the characteristic impedance of the line and, for a finite length radial line, it is generally complex. These factors limit the performance and make the design of radial combiners difficult and normally full wave optimisation-based.

This is not a problem in coaxial combiners, where an oversized coaxial transmission line is normally used as the combining structure. In a coaxial combiner the input ports are placed symmetrically around a coaxial structure on a plane perpendicular to the axis of the coaxial system, and the energy travels axially between the input ports and a coaxial output port. Since a coaxial line supports a uniform TEM transmission line mode (constant characteristic transmission line impedance), it has the advantage that normal transmission line theory can be used for the matching of the low impedance line at input ports to a higher impedance (typically 50  $\Omega$ ) output port. An 18-way coaxial combiner has been demonstrated at *L*-band, which obtained a 15% bandwidth with a return loss of better than -20 dB [10].

The uniform transmission line characteristics, and therefore design simplicity, of coaxial combiners make them very attractive, but for combiners with many input ports (typically  $N > 20$ ), accurate construction of the low impedance coaxial line becomes very difficult. Also, when many input ports are desired, especially at higher frequencies, the common path length becomes long since some form of tapered coaxial line is normally needed to increase the size of the outer conductor enough to allow adequate space for the input ports [10]. This is also seen in the design of an 8-diode *X*-band combiner in [2, 11] where 8 diodes, which act as the power generating devices, are mounted in a conically tapered coaxial line. A 15% bandwidth is reported, but very little design information is given. Also, the structure is designed specifically as an IMPATT diode combiner, and must be completely redesigned if input ports are required.

In this dissertation, it is shown that the problems associated with both radial and coaxial combiners can be solved by using conical lines instead, whilst retaining the very desirable characteristics of uniform TEM transmission line propagation offered by coaxial lines, and the form

factor of the radial types. A conical line power combiner is very similar to a radial combiner, except that a conical transmission line is used. Conical transmission lines have the significant advantage that they support a uniform TEM transmission line mode, and therefore have a constant characteristic transmission line impedance against radial distance. This greatly simplifies the design and modelling of the structure for broadband applications compared to that of a radial combiner. It also allows for a simple, broadband coaxial to conical line transition [12]. The precision construction of the conical transmission line has historically been more difficult than the construction of a simple parallel plate radial line, however modern computer numerical control (CNC)–lathes are able to machine conical structures effortlessly. While it would seem as if conical lines should be the medium of choice for axially symmetric combiners, only a single instance could be found in the literature where a conical line was used as the combining structure, and that in 1978 [13]. In this paper, a conical combiner was built at  $Ku$ -band to combine the power from 8 GaAs IMPATT diodes mounted in rectangular waveguides placed at one end of the conical line, to generate 17.9 W of output power at 14.6 GHz [2, 13]. No information is however given on the design of the structure, and very little on performance. Twenty years later, Van der Walt [12] suggests in a paper that conical lines can be used to combine coaxial ports, but again no design information is given. Aside from these references, literature is devoid of any approaches or algorithms for the design of conical line combiners. It is the aim of this dissertation to present such a design approach.

## 1.2 About the Dissertation

In this dissertation a technique for the design of conical line power combiners with coaxial input and output ports is proposed. The technique is developed through the design of a constant impedance conical line 10-way combiner with optimised stepped impedance matching networks in the input and output feed lines. A -14.5 dB return loss bandwidth of 74% is achieved at  $X$ -band, which is much superior to the results obtained by similar radial line combiners in the literature. Improvements are further presented to allow for easier manufacturing and assembly of the structure, and for higher peak power handling capability, by employing a tapered conical transmission line in the combining structure, and an optimised tapered line output matching section. A 10-way combiner of this type is designed and constructed displaying a -18.7 dB return loss bandwidth of 47%. The design technique proposed here is simple to execute, calls for very little full wave analysis of the structure, and only uses circuit model optimisation to achieve the required broadband operation. The simplicity of the design technique is further demonstrated by the design and simulation of a 30-way tapered line conical combiner at  $K_u$ -band which shows a simulated -20 dB return loss bandwidth of 34%.

The primary contributions of this dissertation are:

- A technique for the design of  $N$ -way constant impedance conical line power combiners with optimised stepped impedance input and output port matching sections [14],
- A technique for the design of  $N$ -way tapered conical line power combiners with optimised tapered line output matching sections [15].
- A study of the design limitations for conical transmission line power combiners [16].

A secondary contribution of the dissertation is a complete analysis of higher order modes in conical transmission lines including:

- A proof of the cutoff wavelength equation,
- Information on the numerical computation of the cutoff wavelengths [17],
- Analytical field plots of some higher order modes which are unavailable in the literature.

### 1.3 Layout of the Dissertation

The dissertation commences with a detailed theoretical analysis of conical transmission lines in Chapter 2. A physical description of a conical transmission line is given, and then Maxwell's equations are solved in the spherical coordinate system with the conical line boundary conditions imposed, to give analytical field results for the natural modes in such a line. A technique for solving the associated Legendre functions is given, and analytical field plots of some higher order modes in a conical transmission line are shown after a discussion on the gradual cutoff wavelength observed in conical transmission lines. Finally, some comparisons to numerical simulation results of the fields are made.

Chapter 3 discusses the design of a 10-way constant impedance conical line combiner with optimised stepped impedance matching sections in the input and output feed lines. The entire design process is discussed in detail and the simulated and measured results of the constructed combiner are presented.

In Chapter 4, a tapered conical line combiner with an optimised tapered output line matching section is proposed. Again the entire design process is discussed step-by-step and the simulated and measured results are presented.

Finally, an expansion of the developed design technique is given in Chapter 5 to include the design of general  $N$ -way combiners. A study is done of the behaviour of combiners of different

electrical sizes to include the effect of higher order modes into the general design technique, and also to determine the limitations thereof. The chapter is concluded with the design and simulation of a 30-way combiner to validate the general design technique. The dissertation ends with a brief conclusion in Chapter 6.

## Chapter 2

# Theoretical Analysis of Conical Transmission Lines

The theory for waves guided within conical structures was first developed more than sixty years ago by Schelkunoff [18, 19]. This theory has been repeated and expanded by many workers since, including Marcuvitz [8] (who termed it a ‘Conical Waveguide’), Harrington [20], and more recently Balanis [21] (who termed it a ‘Bi-Conical Transmission Line’). None of these, however, include any numerical data because of the complexity of the calculations required. In 2001 Weil *et al.* [22] published some numerical data on the cutoff frequency of the higher order modes present in such a transmission line. These results are, however, only presented for some of the higher order modes, and are therefore quite limited. No other presentation of numerical data could be found in literature.

In this chapter a thorough description and theoretical analysis of coaxial transmission lines of conical geometry (conical transmission lines) is presented. A complete mathematical description, including computation and numerical data, of the cutoff frequency and field distributions of the TEM and higher order modes present in such a line is given. The cutoff phenomena in conical lines is not of the abrupt kind like normal guides, but occurs gradually. Standard texts all use the same simple equation to calculate a single frequency which they designate as the cutoff frequency, without providing real motivation as to why that particular point is chosen. Here, a simple proof is presented for the validity of that choice. Since no literature could be found describing the shape of these modes, analytical results are compared with simulated numerical results. Plots of the analytical solutions are made using The Mathworks’ MATLAB Version 6.5, and full wave simulated results are obtained by Computer Simulation Technology’s Microwave Studio (CST-MWS) Versions 3 and 2006B. As far as the author could ascertain, this is the only detailed treatment of conical lines which contains evaluated analytical results for the field patterns of the higher order modes.

## 2.1 Physical Description of a Conical Transmission Line

A conical transmission line is best analysed using the spherical coordinate system. The geometry of a conical transmission line as well as the definition of the spherical coordinate system are shown in Fig. 2.1.

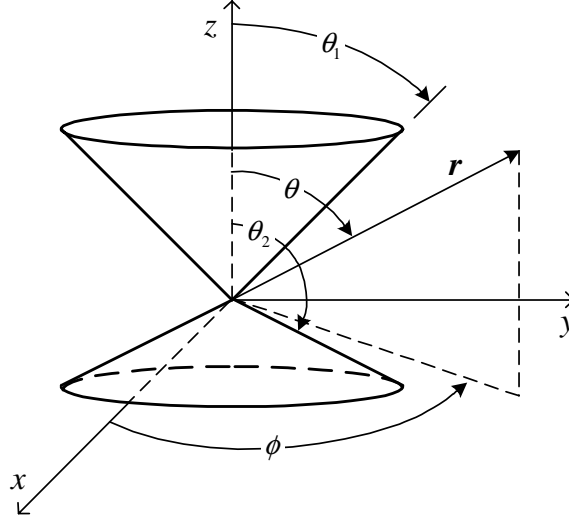


Fig. 2.1. Geometry of a conical transmission line.

The feed point of the line is between the apices of the two cones described by the half angles  $\theta_1$  and  $\theta_2$ . This structure is also representative of a bi-conical antenna [23, 24], especially if the difference between  $\theta_2$  and  $\theta_1$  is large. As this difference becomes smaller, the structure acts more like a transmission line (radiates less), and this is the case that will be presented here.

## 2.2 Wave Equation and Solution in Spherical Coordinates

The derivation of fields in spherical coordinates is well-known and appears in many textbooks. For the sake of clarity, it is repeated here in some detail, following the exposition of [21].

### 2.2.1 Direct Approach

The first of Maxwell's equations can be written in differential form in terms of time harmonic fields in a lossless, isotropic, source-free medium as

$$\nabla \times \mathbf{E} = -j\omega\mu\mathbf{H} \quad (2.1)$$

$$\nabla \times \mathbf{H} = j\omega\epsilon\mathbf{E}, \quad (2.2)$$

and constitute two equations in two unknowns, the electric field vector  $\mathbf{E}$ , and the magnetic field vector  $\mathbf{H}$ . Taking the curl of (2.1) and using (2.2) gives

$$\nabla \times \nabla \times \mathbf{E} = -j\omega\mu\nabla \times \mathbf{H} = \omega^2\mu\epsilon\mathbf{E}, \quad (2.3)$$

which is an equation in  $\mathbf{E}$ . This can be simplified through the use of a vector identity

$$\nabla \times \nabla \times \mathbf{A} = \nabla(\nabla \cdot \mathbf{A}) - \nabla^2 \mathbf{A} \quad (2.4)$$

to yield

$$\nabla^2 \mathbf{E} + \omega^2\mu\epsilon\mathbf{E} = 0, \quad (2.5)$$

using the fact that  $\nabla \cdot \mathbf{E} = 0$  in a source-free region. Equation (2.5) is known as the wave equation, or Helmholtz equation for  $\mathbf{E}$ . A similar equation can be derived for  $\mathbf{H}$  in the same manner. A constant  $\beta = \omega\sqrt{\mu\epsilon}$  is defined and called the wavenumber, or phase constant of the medium with units 1/m.

A general set of solutions to the wave equation (2.5) is now sought in the spherical coordinate system. The method of separation of variables will be used to obtain such a set of solutions. A general solution for the electric field in spherical coordinates can be written as

$$\mathbf{E}(r, \theta, \phi) = E_r(r, \theta, \phi)\hat{\mathbf{r}} + E_\theta(r, \theta, \phi)\hat{\boldsymbol{\theta}} + E_\phi(r, \theta, \phi)\hat{\boldsymbol{\phi}}. \quad (2.6)$$

Substituting (2.6) into the vector wave equation (2.5) produces

$$\nabla^2(E_r\hat{\mathbf{r}} + E_\theta\hat{\boldsymbol{\theta}} + E_\phi\hat{\boldsymbol{\phi}}) = -\beta^2(E_r\hat{\mathbf{r}} + E_\theta\hat{\boldsymbol{\theta}} + E_\phi\hat{\boldsymbol{\phi}}). \quad (2.7)$$

Since

$$\begin{aligned} \nabla^2(\hat{\mathbf{r}}E_r) &\neq \hat{\mathbf{r}}\nabla^2 E_r \\ \nabla^2(\hat{\boldsymbol{\theta}}E_\theta) &\neq \hat{\boldsymbol{\theta}}\nabla^2 E_\theta \\ \nabla^2(\hat{\boldsymbol{\phi}}E_\phi) &\neq \hat{\boldsymbol{\phi}}\nabla^2 E_\phi, \end{aligned} \quad (2.8)$$

(2.7) does not reduce to three simple scalar wave equations. To reduce (2.7) to three scalar partial differential equations, (2.5) must be rewritten using the vector identity (2.4) as

$$\nabla(\nabla \cdot \mathbf{E}) - \nabla \times \nabla \times \mathbf{E} = -\beta^2 \mathbf{E}. \quad (2.9)$$

In (2.9) all the operators on the left can be performed in any coordinate system. By substituting (2.6) into (2.9) and performing some lengthy mathematical manipulations, (2.9) reduces to three scalar partial differential equations of the form

$$\begin{aligned} \nabla^2 E_r - \frac{2}{r^2} \left( E_r + E_\theta \cot \theta + \csc \theta \frac{\partial E_\phi}{\partial \phi} + \frac{\partial E_\theta}{\partial \theta} \right) &= -\beta^2 E_r \\ \nabla^2 E_\theta - \frac{1}{r^2} \left( E_\theta \csc^2 \theta - 2 \frac{\partial E_r}{\partial \theta} + 2 \cot \theta \csc \theta \frac{\partial E_\phi}{\partial \phi} \right) &= -\beta^2 E_\theta \\ \nabla^2 E_\phi - \frac{1}{r^2} \left( E_\phi \csc^2 \theta - 2 \csc \theta \frac{\partial E_r}{\partial \phi} - 2 \cot \theta \csc \theta \frac{\partial E_\theta}{\partial \phi} \right) &= -\beta^2 E_\phi. \end{aligned} \quad (2.10)$$

### 2.2.2 Solutions Using Vector Potentials

Since all the equations in (2.10) are coupled, it would be most difficult to solve in its present form. Instead a solution will be constructed using vector potentials,  $\mathbf{A}$  and  $\mathbf{F}$ . Since in a source-free region the magnetic flux density is solenoidal ( $\nabla \cdot \mathbf{B} = 0$ ), it can be represented as the curl of another vector because it obeys the vector identity

$$\nabla \cdot (\nabla \times \mathbf{A}) = 0, \quad (2.11)$$

where  $\mathbf{A}$  is an arbitrary vector called the magnetic vector potential. Thus the definition of  $\mathbf{A}$  is given by

$$\mathbf{B}_{\mathbf{A}} = \mu \mathbf{H}_{\mathbf{A}} = \nabla \times \mathbf{A}, \quad (2.12)$$

where the subscript  $\mathbf{A}$  indicates a field quantity due to  $\mathbf{A}$ . Substituting (2.12) into Maxwell's equation (2.1) and rearranging produces

$$\nabla \times (\mathbf{E}_{\mathbf{A}} + j\omega \mathbf{A}) = 0. \quad (2.13)$$

Introducing the vector identity

$$\nabla \times (-\nabla \psi_e) = 0 \quad (2.14)$$

into (2.13) gives

$$\mathbf{E}_{\mathbf{A}} = -\nabla \psi_e - j\omega \mathbf{A}, \quad (2.15)$$

where  $\psi_e$  represents an arbitrary electric scalar potential function that is a function of position. Taking the curl of both sides of (2.12) and using the vector identity (2.4) leads to

$$\mu \nabla \times \mathbf{H}_{\mathbf{A}} = \nabla(\nabla \cdot \mathbf{A}) - \nabla^2 \mathbf{A} \quad (2.16)$$

in a homogeneous medium. Substituting (2.15) into Maxwell's equation (2.2) and equating to (2.16) produces

$$\nabla^2 \mathbf{A} + \beta^2 \mathbf{A} = \nabla(\nabla \cdot \mathbf{A} + j\omega \mu \epsilon \psi_e), \quad (2.17)$$

or using the vector identity (2.4)

$$\nabla \times \nabla \times \mathbf{A} - \beta^2 \mathbf{A} = -j\omega \mu \epsilon \nabla \psi_e \quad (2.18)$$

in a source free region ( $J = 0$ ). Since only the curl of  $\mathbf{A}$  was defined, and a vector can only be uniquely defined by both its curl and its divergence, the divergence of  $\mathbf{A}$  must be defined. The divergence of a vector is independent of its curl, thus the divergence of  $\mathbf{A}$  can be arbitrarily defined so as to simplify (2.17). This is accomplished by choosing

$$\nabla \cdot \mathbf{A} = -j\omega \mu \epsilon \psi_e, \quad (2.19)$$

which is known as the Lorenz gauge. Substitution of the Lorenz gauge (2.19) into (2.17) yields the vector wave equation

$$\nabla^2 \mathbf{A} + \beta^2 \mathbf{A} = 0. \quad (2.20)$$

In addition (2.15) reduces to

$$\mathbf{E}_A = -j\omega \mathbf{A} - j \frac{1}{\omega\mu\epsilon} \nabla(\nabla \cdot \mathbf{A}). \quad (2.21)$$

A similar argument can be followed with the electric vector potential  $\mathbf{F}$ , since in a source-free region the electric flux density is solenoidal ( $\nabla \cdot \mathbf{D} = 0$ ). Using (2.11) the definition of  $\mathbf{F}$  is

$$\mathbf{D}_F = \epsilon \mathbf{E}_F = -\nabla \times \mathbf{F}, \quad (2.22)$$

where the subscript  $\mathbf{F}$  indicates a field quantity due to  $\mathbf{F}$ . Substituting (2.22) into Maxwell's equation (2.2) and using the vector identity (2.14) produces

$$\mathbf{H}_F = -\nabla \psi_m - j\omega \mathbf{F}, \quad (2.23)$$

where  $\psi_m$  represents an arbitrary magnetic scalar potential function that is a function of position. Using a procedure analogous to the one used above for  $\mathbf{A}$ , it can readily be shown that

$$\nabla \times \nabla \times \mathbf{F} - \beta^2 \mathbf{F} = -j\omega\mu\epsilon \nabla \psi_m, \quad (2.24)$$

$$\nabla^2 \mathbf{F} + \beta^2 \mathbf{F} = 0 \quad (2.25)$$

and also

$$\mathbf{H}_F = -j\omega \mathbf{F} - \frac{j}{\omega\mu\epsilon} \nabla(\nabla \cdot \mathbf{F}). \quad (2.26)$$

The total fields are found as a superposition of the fields due to  $\mathbf{A}$  and  $\mathbf{F}$  as

$$\mathbf{E} = \mathbf{E}_A + \mathbf{E}_F = -j\omega \mathbf{A} - j \frac{1}{\omega\mu\epsilon} \nabla(\nabla \cdot \mathbf{A}) - \frac{1}{\epsilon} \nabla \times \mathbf{F} \quad (2.27)$$

$$\mathbf{H} = \mathbf{H}_A + \mathbf{H}_F = \frac{1}{\mu} \nabla \times \mathbf{A} - j\omega \mathbf{F} - j \frac{1}{\omega\mu\epsilon} \nabla(\nabla \cdot \mathbf{F}). \quad (2.28)$$

### 2.2.3 Transverse Electric and Magnetic Solutions

Should the case be taken where  $\mathbf{A} = 0$  and  $\mathbf{F} = \psi \hat{\mathbf{z}}$ , it can be seen from (2.27) that the E-field is reduced to

$$\mathbf{E} = -\frac{\psi}{\epsilon} \nabla \times \hat{\mathbf{z}}, \quad (2.29)$$

which clearly has no component in the  $z$ -direction. This constitutes a transverse electric mode with respect to the  $z$ -direction ( $\text{TE}^z$ ). Also when  $\mathbf{F} = 0$  and  $\mathbf{A} = \psi \hat{\mathbf{z}}$  the H-field becomes

$$\mathbf{H} = \frac{\psi}{\mu} \nabla \times \hat{\mathbf{z}}, \quad (2.30)$$

which has no component in the  $z$ -direction. This constitutes a transverse magnetic mode with respect to the  $z$ -direction (TM <sup>$z$</sup> ). It will be shown that  $\psi$  can be chosen sufficiently general to express any TE or TM field in a homogeneous source-free region. Also, since the  $z$ -direction is arbitrary, the above results can be applied to any orthogonal coordinate system.

The TE <sup>$r$</sup>  solution in the spherical coordinate system can now be found by setting

$$\mathbf{F} = F_r(r, \theta, \phi) \hat{\mathbf{r}} \quad (2.31)$$

$$\mathbf{A} = 0. \quad (2.32)$$

Expanding (2.24) using (2.31) leads to

$$\begin{aligned} \nabla \times \nabla \times \mathbf{F} = & \left\{ \frac{1}{r \sin \theta} \left[ \frac{\partial}{\partial \theta} \left( -\frac{\sin \theta}{r} \frac{\partial F_r}{\partial \theta} \right) - \frac{\partial}{\partial \phi} \left( \frac{1}{r \sin \theta} \frac{\partial F_r}{\partial \phi} \right) \right] \right\} \hat{\mathbf{r}} \\ & + \left[ \frac{1}{r} \left( \frac{\partial^2 F_r}{\partial r \partial \theta} \right) \right] \hat{\boldsymbol{\theta}} + \left( \frac{1}{r \sin \theta} \frac{\partial^2 F_r}{\partial r \partial \phi} \right) \hat{\boldsymbol{\phi}} \end{aligned} \quad (2.33)$$

$$\nabla \psi_m = \frac{\partial \psi_m}{\partial r} \hat{\mathbf{r}} + \frac{1}{r} \frac{\partial \psi_m}{\partial \theta} \hat{\boldsymbol{\theta}} + \frac{1}{r \sin \theta} \frac{\partial \psi_m}{\partial \phi} \hat{\boldsymbol{\phi}}. \quad (2.34)$$

By comparing the  $\hat{\mathbf{r}}$ ,  $\hat{\boldsymbol{\theta}}$  and  $\hat{\boldsymbol{\phi}}$  components of (2.33) and (2.34), (2.24) can be reduced to three partial differential equations

$$\frac{1}{r \sin \theta} \left[ -\frac{\partial}{\partial \theta} \left( \frac{\sin \theta}{r} \frac{\partial F_r}{\partial \theta} \right) - \frac{\partial}{\partial \phi} \left( \frac{1}{r \sin \theta} \frac{\partial F_r}{\partial \phi} \right) \right] - \beta^2 F_r = -j\omega\mu\epsilon \frac{\partial \psi_m}{\partial r}, \quad (2.35)$$

$$\frac{\partial^2 F_r}{\partial r \partial \theta} = \frac{\partial}{\partial \theta} \left( \frac{\partial F_r}{\partial r} \right) = \frac{\partial}{\partial \theta} (-j\omega\mu\epsilon \psi_m) \quad (2.36)$$

and

$$\frac{\partial^2 F_r}{\partial r \partial \phi} = \frac{\partial}{\partial \phi} \left( \frac{\partial F_r}{\partial r} \right) = \frac{\partial}{\partial \phi} (-j\omega\mu\epsilon \psi_m). \quad (2.37)$$

Equations (2.36) and (2.37) are satisfied simultaneously if

$$\frac{\partial F_r}{\partial r} = -j\omega\mu\epsilon \psi_m \Rightarrow \psi_m = -\frac{1}{j\omega\mu\epsilon} \frac{\partial F_r}{\partial r}. \quad (2.38)$$

Substituting (2.38) into (2.35) leads to the uncoupled partial differential equation for  $F_r$

$$\frac{\partial^2 F_r}{\partial r^2} + \frac{1}{r^2 \sin \theta} \frac{\partial}{\partial \theta} \left( \sin \theta \frac{\partial F_r}{\partial \theta} \right) + \frac{1}{r^2 \sin^2 \theta} \frac{\partial^2 F_r}{\partial \phi^2} + \beta^2 F_r = 0 \quad (2.39)$$

which can be written in succinct form as

$$(\nabla^2 + \beta^2) \frac{F_r}{r} = 0. \quad (2.40)$$

A similar procedure can be followed for the TM <sup>$r$</sup>  solution by setting

$$\mathbf{A} = A_r(r, \theta, \phi) \hat{\mathbf{r}} \quad (2.41)$$

$$\mathbf{F} = 0 \quad (2.42)$$

to find

$$(\nabla^2 + \beta^2) \frac{A_r}{r} = 0. \quad (2.43)$$

Thus for TE and TM solutions, the vector wave equations (2.20) and (2.25) reduce to the scalar wave equation

$$\nabla^2 \psi + \beta^2 \psi = 0, \quad (2.44)$$

which can be solved in any coordinate system, where

$$\psi = \begin{cases} \frac{F_r}{r} & \text{for TE}^r \text{ modes} \\ \frac{A_r}{r} & \text{for TM}^r \text{ modes.} \end{cases} \quad (2.45)$$

The solution to (2.44) in spherical coordinates can be found by assuming a separable solution for  $\psi(r, \theta, \phi)$  of the form

$$\psi(r, \theta, \phi) = f(r)g(\theta)h(\phi). \quad (2.46)$$

Expanding (2.44) and substituting (2.46) yields

$$gh \frac{1}{r^2} \frac{\partial}{\partial r} \left( r^2 \frac{\partial f}{\partial r} \right) + fh \frac{1}{r^2 \sin \theta} \frac{\partial}{\partial \theta} \left( \sin \theta \frac{\partial g}{\partial \theta} \right) + fg \frac{1}{r^2 \sin^2 \theta} \frac{\partial^2 h}{\partial \phi^2} = -\beta^2 fgh. \quad (2.47)$$

Dividing both sides by  $fgh$ , multiplying by  $r^2 \sin^2 \theta$ , and replacing the partials by ordinary differentials reduces (2.47) to

$$\frac{\sin^2 \theta}{f} \frac{d}{dr} \left( r^2 \frac{df}{dr} \right) + \frac{\sin \theta}{g} \frac{d}{d\theta} \left( \sin \theta \frac{dg}{d\theta} \right) + \frac{1}{h} \frac{d^2 h}{d\phi^2} = -(\beta r \sin \theta)^2. \quad (2.48)$$

Since the last term on the left side of (2.48) is only a function of  $\phi$ , it can be set equal to

$$\frac{1}{h} \frac{d^2 h}{d\phi^2} = -m^2 \Rightarrow \frac{d^2 h}{d\phi^2} = -m^2 h \quad (2.49)$$

where  $m$  is a constant. Substituting (2.49) into (2.48), dividing both sides by  $\sin^2 \theta$  and simplifying reduces (2.48) to

$$\frac{1}{f} \frac{d}{dr} \left( r^2 \frac{df}{dr} \right) + (\beta r)^2 + \frac{1}{g \sin \theta} \frac{d}{d\theta} \left( \sin \theta \frac{dg}{d\theta} \right) - \left( \frac{m}{\sin \theta} \right)^2 = 0. \quad (2.50)$$

Now the last two terms on the left side of (2.50) are only functions of  $\theta$ , and they can be set equal to

$$\frac{1}{g \sin \theta} \frac{d}{d\theta} \left( \sin \theta \frac{dg}{d\theta} \right) - \left( \frac{m}{\sin \theta} \right)^2 = -\nu(\nu + 1), \quad (2.51)$$

where  $\nu$  is a constant. Equation (2.51) is known as the associated Legendre equation [20, 25, 26, 27]. Substituting (2.51) into (2.50) reduces it to

$$\frac{1}{f} \frac{d}{dr} \left( r^2 \frac{df}{dr} \right) + (\beta r)^2 - \nu(\nu + 1) = 0, \quad (2.52)$$

which is closely related to the Bessel differential equation [20, 25, 26, 27].

Solutions to the differential equations (2.52), (2.51) and (2.49) take the forms, respectively, of

$$f_1(r) = A_1 j_\nu(\beta r) + B_1 y_\nu(\beta r) \quad (2.53)$$

or

$$f_2(r) = C_1 h_\nu^{(1)}(\beta r) + D_1 h_\nu^{(2)}(\beta r), \quad (2.54)$$

and

$$g_1(\theta) = A_2 P_\nu^m(\cos \theta) + B_2 P_\nu^m(-\cos \theta) \quad \nu \neq \text{integer} \quad (2.55)$$

or

$$g_2(\theta) = C_2 P_\nu^m(\cos \theta) + D_2 Q_\nu^m(\cos \theta), \quad (2.56)$$

and

$$h_1(\phi) = A_3 e^{-jm\phi} + B_3 e^{+jm\phi} \quad (2.57)$$

or

$$h_2(\phi) = C_3 \cos m\phi + D_3 \sin m\phi. \quad (2.58)$$

In (2.53)  $j_\nu(\beta r)$  and  $y_\nu(\beta r)$  are referred to, respectively, as the spherical Bessel functions of the first and second kind of order  $\nu$ . They are used to represent radial standing waves, and they are related, respectively, to the corresponding regular Bessel functions  $J_{\nu+1/2}(\beta r)$  and  $Y_{\nu+1/2}(\beta r)$  by

$$j_\nu(\beta r) = \sqrt{\frac{\pi}{2\beta r}} J_{\nu+1/2}(\beta r) \quad (2.59)$$

$$y_\nu(\beta r) = \sqrt{\frac{\pi}{2\beta r}} Y_{\nu+1/2}(\beta r) \quad (2.60)$$

In (2.54)  $h_\nu^{(1)}(\beta r)$  and  $h_\nu^{(2)}(\beta r)$  are referred to, respectively, as the spherical Hankel functions of the first and second kind of order  $\nu$ . They are used to represent radial travelling waves, and they are related, respectively, to the corresponding regular Hankel functions  $H_{\nu+1/2}^{(1)}(\beta r)$  and  $H_{\nu+1/2}^{(2)}(\beta r)$  by

$$h_\nu^{(1)}(\beta r) = \sqrt{\frac{\pi}{2\beta r}} H_{\nu+1/2}^{(1)}(\beta r) \quad (2.61)$$

$$h_\nu^{(2)}(\beta r) = \sqrt{\frac{\pi}{2\beta r}} H_{\nu+1/2}^{(2)}(\beta r) \quad (2.62)$$

In (2.56)  $P_\nu^m(\cos \theta)$  and  $Q_\nu^m(\cos \theta)$  are referred to, respectively, as the associated Legendre functions of the first and second kind of degree  $\nu$  and order  $m$ .

The solutions needed, however, are not for  $\psi(r, \theta, \phi)$ , but for

$$\left. \begin{array}{l} F_r(r, \theta, \phi) \\ A_r(r, \theta, \phi) \end{array} \right\} = r\psi(r, \theta, \phi) = rf(r)g(\theta)h(\phi) = \hat{f}(r)g(\theta)h(\phi). \quad (2.63)$$

The most convenient solution is to represent the factor  $rf(r) = \hat{f}(r)$  not by the spherical Bessel  $[j_\nu(\beta r), y_\nu(\beta r)]$  or Hankel  $[h_\nu^{(1)}(\beta r), h_\nu^{(2)}(\beta r)]$  functions, but by another form of the spherical Bessel and Hankel functions denoted by  $\hat{B}_\nu(\beta r)$  [for either  $\hat{J}_\nu(\beta r), \hat{Y}_\nu(\beta r), \hat{H}_\nu^{(1)}(\beta r)$  or  $\hat{H}_\nu^{(2)}(\beta r)$ ]. These are related to the regular spherical Bessel and Hankel functions denoted by  $b_\nu(\beta r)$  [for either  $j_\nu(\beta r), y_\nu(\beta r), h_\nu^{(1)}(\beta r)$  or  $h_\nu^{(2)}(\beta r)$ ] by

$$\hat{B}_\nu(\beta r) = \beta r b_\nu(\beta r) = \beta r \sqrt{\frac{\pi}{2\beta r}} B_{\nu+1/2}(\beta r) = \sqrt{\frac{\pi\beta r}{2}} B_{\nu+1/2}(\beta r), \quad (2.64)$$

where  $B_{\nu+1/2}(\beta r)$  is used to represent the regular cylindrical Bessel or Hankel functions of  $J_{\nu+1/2}(\beta r), Y_{\nu+1/2}(\beta r), H_{\nu+1/2}^{(1)}(\beta r)$  and  $H_{\nu+1/2}^{(2)}(\beta r)$ . These new spherical Bessel and Hankel functions were introduced by Schelkunoff [19] and satisfy the differential equation

$$\left[ \frac{d^2}{dr^2} + \beta^2 - \frac{\nu(\nu+1)}{r^2} \right] \hat{B}_\nu = 0, \quad (2.65)$$

which is obtained by substituting  $b_\nu(\beta r) = \hat{B}_\nu(\beta r)/\beta r$  in

$$\frac{d}{dr} \left( r^2 \frac{db_\nu}{dr} \right) + [(\beta r)^2 - \nu(\nu+1)] b_\nu = 0. \quad (2.66)$$

Therefore the solutions for  $\hat{f}(r)$  of (2.63) are of the new form of the spherical Bessel or Hankel functions denoted by

$$\hat{f}_1(r) = A_1 \hat{J}_\nu(\beta r) + B_1 \hat{Y}_\nu(\beta r) \quad (2.67)$$

or

$$\hat{f}_2(r) = C_1 \hat{H}_\nu^{(1)}(\beta r) + D_1 \hat{H}_\nu^{(2)}(\beta r), \quad (2.68)$$

which are related to the regular Bessel and Hankel functions by (2.64). The total solution for  $F_r$  or  $A_r$  of (2.63) will be the product of the appropriate spherical wave functions representing  $\hat{f}(r), g(\theta)$  and  $h(\phi)$ .

## 2.3 Conical Transmission Line Boundary Conditions

The boundary conditions that a conical transmission line implies will now be enforced on the results found in Section 2.2 to find the possible field distributions of the different modes in such a line.

### 2.3.1 Transverse Electric Modes

The field patterns of the TE modes are found by enforcing (2.31) and (2.32) on equations (2.27) and (2.28) to yield

$$\mathbf{E} = -\frac{1}{\epsilon} \nabla \times \mathbf{F} \quad (2.69)$$

or

$$E_r = 0 \quad (2.70)$$

$$E_\theta = -\frac{1}{\epsilon} \frac{1}{r \sin \theta} \frac{\partial F_r}{\partial \phi} \quad (2.71)$$

$$E_\phi = \frac{1}{\epsilon} \frac{1}{r} \frac{\partial F_r}{\partial \theta} \quad (2.72)$$

and

$$\mathbf{H} = \frac{1}{j\omega\mu\epsilon} \nabla \times \nabla \times \mathbf{F} \quad (2.73)$$

or

$$H_r = \frac{1}{j\omega\mu\epsilon} \left( \frac{\partial^2}{\partial r^2} + \beta^2 \right) F_r \quad (2.74)$$

$$H_\theta = \frac{1}{j\omega\mu\epsilon} \frac{1}{r} \frac{\partial^2 F_r}{\partial r \partial \theta} \quad (2.75)$$

$$H_\phi = \frac{1}{j\omega\mu\epsilon} \frac{1}{r \sin \theta} \frac{\partial^2 F_r}{\partial r \partial \phi}, \quad (2.76)$$

where  $F_r/r$  is a solution to (2.40).

The solutions for  $F_r$  are now chosen from the solutions to the differential equations (2.52), (2.51) and (2.49) for a conical transmission line with standing waves in  $\phi$  and travelling waves in the  $r$ -direction. The  $r$ -dependent solution is therefore chosen as (2.68), and the  $\phi$ -dependent solution as (2.58). Since  $\theta = 0^\circ$  and  $\theta = 180^\circ$  are not included in the solution domain, (2.55) or (2.56) can be chosen as the  $\theta$ -dependent solution, and the former is chosen in order for the results to be consistent with those given in [20] and [21] (When  $\theta = 0^\circ$  and  $\theta = 180^\circ$  are included in the solution domain, only  $P_\nu^m(\cos \theta)$ , with  $\nu$  an integer, would suffice as the  $\theta$ -dependent solution [20]). Assuming the source is placed at the apex and generates outward travelling waves [ $C_1 = 0$  in (2.68) because  $\hat{H}_\nu^{(1)}(\beta r) \rightarrow j^{-(\nu+1)} e^{j\beta r}$  as  $\beta r \rightarrow \infty$ ],  $F_r$  can be written as

$$F_r(r, \theta, \phi) = D_1 \hat{H}_\nu^{(2)}(\beta r) [A_2 P_\nu^m(\cos \theta) + B_2 P_\nu^m(-\cos \theta)] [C_3 \cos m\phi + D_3 \sin m\phi], \quad (2.77)$$

where  $m = \text{integer}$  ( $m = 0, 1, 2, \dots$ ) because of the condition that  $F_r(r, \theta, 0) = F_r(r, \theta, 2\pi)$ .

The values of  $\nu$  can be determined by applying the boundary conditions

$$E_\phi(r, \theta = \theta_1, \phi) = E_\phi(r, \theta = \theta_2, \phi) = 0. \quad (2.78)$$

Expanding (2.72) gives

$$E_\phi = \frac{D_1}{\epsilon} \frac{1}{r} \hat{H}_\nu^{(2)}(\beta r) \left[ A_2 \frac{dP_\nu^m(\cos \theta)}{d\theta} + B_2 \frac{dP_\nu^m(-\cos \theta)}{d\theta} \right] [C_3 \cos m\phi + D_3 \sin m\phi]. \quad (2.79)$$

Applying the first boundary condition of (2.78) leads to

$$E_\phi(r, \theta_1, \phi) = \frac{D_1}{\epsilon} \frac{1}{r} \hat{H}_\nu^{(2)}(\beta r) \left[ A_2 \frac{dP_\nu^m(\cos \theta_1)}{d\theta_1} + B_2 \frac{dP_\nu^m(-\cos \theta_1)}{d\theta_1} \right] [C_3 \cos m\phi + D_3 \sin m\phi] = 0, \quad (2.80)$$

and the second boundary condition of (2.78) leads to

$$E_\phi(r, \theta_2, \phi) = \frac{D_1}{\epsilon} \frac{1}{r} \hat{H}_\nu^{(2)}(\beta r) \left[ A_2 \frac{dP_\nu^m(\cos \theta_2)}{d\theta_2} + B_2 \frac{dP_\nu^m(-\cos \theta_2)}{d\theta_2} \right] [C_3 \cos m\phi + D_3 \sin m\phi] = 0. \quad (2.81)$$

Equations (2.80) and (2.81) are satisfied only when

$$A_2 \frac{dP_\nu^m(\cos \theta_1)}{d\theta_1} + B_2 \frac{dP_\nu^m(-\cos \theta_1)}{d\theta_1} = 0 \quad (2.82)$$

$$A_2 \frac{dP_\nu^m(\cos \theta_2)}{d\theta_2} + B_2 \frac{dP_\nu^m(-\cos \theta_2)}{d\theta_2} = 0, \quad (2.83)$$

which is satisfied provided the determinant of (2.82) and (2.83) vanishes, that is

$$\frac{dP_\nu^m(\cos \theta_1)}{d\theta_1} \frac{dP_\nu^m(-\cos \theta_2)}{d\theta_2} - \frac{dP_\nu^m(-\cos \theta_1)}{d\theta_1} \frac{dP_\nu^m(\cos \theta_2)}{d\theta_2} = 0. \quad (2.84)$$

Therefore, the values of  $\nu$  are found as solutions to (2.84), which will be pursued in Section 2.4.

The values of the constants  $A_2$  and  $B_2$  can now easily be found from the under-determined system (2.82) and (2.83) as

$$A_2 = -B_2 \frac{\frac{d}{d\theta_1} P_\nu^m(\cos \theta_1)}{\frac{d}{d\theta_1} P_\nu^m(-\cos \theta_1)} = -B_2 \frac{\frac{d}{d\theta_2} P_\nu^m(\cos \theta_2)}{\frac{d}{d\theta_2} P_\nu^m(-\cos \theta_2)}, \quad (2.85)$$

with any one of  $A_2$  or  $B_2$  chosen arbitrarily.

The TE electric and magnetic fields can now be found using (2.69) to (2.76). Since the  $\cos m\phi$  and  $\sin m\phi$  parts of the solution (2.58) represent orthogonal degenerate modes, only the  $\cos m\phi$  part will be kept in the following results for clarity. Unnecessary constants will also be merged.

The TE electric and magnetic fields are

$$E_r = 0 \quad (2.86)$$

$$E_\theta = \frac{1}{\epsilon} \frac{\hat{H}_\nu^{(2)}(\beta r)}{r \sin \theta} [A_2 P_\nu^m(\cos \theta) + B_2 P_\nu^m(-\cos \theta)] [m \sin m\phi] \quad (2.87)$$

$$E_\phi = \frac{1}{\epsilon} \frac{\hat{H}_\nu^{(2)}(\beta r)}{r} \left[ A_2 \frac{dP_\nu^m(\cos \theta)}{d\theta} + B_2 \frac{dP_\nu^m(-\cos \theta)}{d\theta} \right] \cos m\phi \quad (2.88)$$

$$H_r = \frac{1}{j\omega\mu\epsilon} \left[ \frac{d^2}{dr^2} \hat{H}_\nu^{(2)}(\beta r) + \beta^2 \hat{H}_\nu^{(2)}(\beta r) \right] [A_2 P_\nu^m(\cos \theta) + B_2 P_\nu^m(-\cos \theta)] \cos m\phi \quad (2.89)$$

$$H_\theta = \frac{1}{j\omega\mu\epsilon} \frac{1}{r} \frac{d}{dr} \hat{H}_\nu^{(2)}(\beta r) \left[ A_2 \frac{dP_\nu^m(\cos \theta)}{d\theta} + B_2 \frac{dP_\nu^m(-\cos \theta)}{d\theta} \right] \cos m\phi \quad (2.90)$$

$$H_\phi = \frac{1}{j\omega\mu\epsilon} \frac{1}{r \sin \theta} \frac{d}{dr} \hat{H}_\nu^{(2)}(\beta r) [A_2 P_\nu^m(\cos \theta) + B_2 P_\nu^m(-\cos \theta)] [-m \sin m\phi], \quad (2.91)$$

with the derivatives of the Hankel and associated Legendre functions given in Appendix A.

### 2.3.2 Transverse Magnetic Modes

The field patterns of the TM modes are found by enforcing (2.41) and (2.42) on equations (2.27) and (2.28) to yield

$$\mathbf{E} = \frac{1}{j\omega\mu\epsilon} \nabla \times \nabla \times \mathbf{A} \quad (2.92)$$

or

$$E_r = \frac{1}{j\omega\mu\epsilon} \left( \frac{\partial^2}{\partial r^2} + \beta^2 \right) A_r \quad (2.93)$$

$$E_\theta = \frac{1}{j\omega\mu\epsilon} \frac{1}{r} \frac{\partial^2 A_r}{\partial r \partial \theta} \quad (2.94)$$

$$E_\phi = \frac{1}{j\omega\mu\epsilon} \frac{1}{r \sin \theta} \frac{\partial^2 A_r}{\partial r \partial \phi} \quad (2.95)$$

and

$$\mathbf{H} = \frac{1}{\mu} \nabla \times \mathbf{A} \quad (2.96)$$

or

$$H_r = 0 \quad (2.97)$$

$$H_\theta = \frac{1}{\mu} \frac{1}{r \sin \theta} \frac{\partial A_r}{\partial \phi} \quad (2.98)$$

$$H_\phi = -\frac{1}{\mu} \frac{1}{r} \frac{\partial A_r}{\partial \theta}, \quad (2.99)$$

where  $A_r/r$  is a solution to (2.43).

Following a similar procedure to that of the previous section, it can be shown that for TM modes  $A_r$  reduces to

$$A_r(r, \theta, \phi) = D_1 \hat{H}_\nu^{(2)}(\beta r) [A_2 P_\nu^m(\cos \theta) + B_2 P_\nu^m(-\cos \theta)] [C_3 \cos m\phi + D_3 \sin m\phi], \quad (2.100)$$

where  $m = \text{integer}$  ( $m = 0, 1, 2, \dots$ ).

The values of  $\nu$  can be determined by applying the boundary conditions (2.78) to (2.100) to find

$$P_\nu^m(\cos \theta_1)P_\nu^m(-\cos \theta_2) - P_\nu^m(-\cos \theta_1)P_\nu^m(\cos \theta_2) = 0. \quad (2.101)$$

The values of  $\nu$  are found as solutions to (2.101), which will be pursued in Section 2.4.

The TM electric and magnetic fields can now be found using (2.92) to (2.99). It will be shown that these modes only exist at much higher frequencies than the TE modes for the structures to be considered, and therefore the full expansions will not be repeated here.

### 2.3.3 Transverse Electromagnetic Modes

The lowest order (or the dominant) mode of the conical transmission line is the one for which  $m = \nu = 0$ . For this mode both (2.84) and (2.101) are satisfied with trivial solutions (see Section 2.4.1) and the potential components (2.77) and (2.100) vanish. It is usually most convenient to represent the TEM mode by the  $\text{TM}_{00}$  which is defined, using (2.56) to represent  $g(\theta)$ , by [20]

$$(A_r)_{00} = B_{00} \hat{H}_0^{(2)}(\beta r) Q_0(\cos \theta) \quad (2.102)$$

since  $P_0^0(\cos \theta) = P_0(\cos \theta) = 1$ . The Legendre polynomial  $Q_0(\cos \theta)$  can also be represented by [25, 26]

$$Q_0(\cos \theta) = \ln \left[ \cot \left( \frac{\theta}{2} \right) \right]. \quad (2.103)$$

Using (2.64), and knowing that [20]

$$h_0^{(2)}(\beta r) = -\frac{e^{-j\beta r}}{j\beta r}, \quad (2.104)$$

the spherical Hankel function  $\hat{H}_0^{(2)}(\beta r)$  can be replaced by its zero-order form

$$\hat{H}_0^{(2)}(\beta r) = j e^{-j\beta r}. \quad (2.105)$$

Using (2.103) and (2.105) reduces (2.102) to

$$(A_r)_{00} = j B_{00} \ln \left[ \cot \left( \frac{\theta}{2} \right) \right] e^{-j\beta r}. \quad (2.106)$$

The corresponding electric and magnetic field components are given, according to (2.92) through (2.99), by [21]

$$E_r = \frac{1}{j\omega\mu\epsilon} \left( \frac{\partial^2}{\partial r^2} + \beta^2 \right) A_r = 0 \quad (2.107)$$

$$E_\theta = \frac{1}{j\omega\mu\epsilon} \frac{1}{r} \frac{\partial^2 A_r}{\partial r \partial \theta} = jB_{00} \frac{\beta}{\omega\mu\epsilon} \frac{1}{r \sin \theta} e^{-j\beta r} \quad (2.108)$$

$$E_\phi = \frac{1}{j\omega\mu\epsilon} \frac{1}{r \sin \theta} \frac{\partial^2 A_r}{\partial r \partial \phi} = 0 \quad (2.109)$$

$$H_r = 0 \quad (2.110)$$

$$H_\theta = \frac{1}{\mu} \frac{1}{r \sin \theta} \frac{\partial A_r}{\partial \phi} = 0 \quad (2.111)$$

$$H_\phi = -\frac{1}{\mu} \frac{1}{r} \frac{\partial A_r}{\partial \theta} = jB_{00} \frac{1}{\mu} \frac{1}{r \sin \theta} e^{-j\beta r}. \quad (2.112)$$

The wave impedance in the radial direction can be found from these equations as

$$Z_w^{+r} = \frac{E_\theta}{H_\phi} = \frac{\beta}{\omega\epsilon} = \sqrt{\frac{\mu}{\epsilon}} = \eta, \quad (2.113)$$

which is the same as the intrinsic impedance of the medium. A characteristic line impedance, which is defined in terms of voltages and currents, can also be defined as  $Z_0 = \frac{V(r)}{I(r)}$ . The voltage between two corresponding points on the cones, a distance  $r$  from the origin, is found by integrating the electric field along a path of constant  $r$  as

$$\begin{aligned} V(r) &= \int_{\theta_1}^{\theta_2} \mathbf{E} \cdot d\boldsymbol{\ell} = \int_{\theta_1}^{\theta_2} (E_\theta \hat{\boldsymbol{\theta}}) \cdot (r \hat{\boldsymbol{\theta}} d\theta) \\ &= \int_{\theta_1}^{\theta_2} E_\theta r d\theta = jB_{00} \frac{\beta e^{-j\beta r}}{\omega\mu\epsilon} \int_{\theta_1}^{\theta_2} \frac{d\theta}{\sin \theta} \\ &= jB_{00} \frac{\beta e^{-j\beta r}}{\omega\mu\epsilon} \ln \left[ \frac{\cot \left( \frac{\theta_1}{2} \right)}{\cot \left( \frac{\theta_2}{2} \right)} \right]. \end{aligned} \quad (2.114)$$

The current on the surface of the cones, a distance  $r$  from the origin, is found by

$$I(r) = \oint_C \mathbf{H} \cdot d\boldsymbol{\ell} = \int_0^{2\pi} (H_\phi \hat{\boldsymbol{\phi}}) \cdot (r \sin \theta \hat{\boldsymbol{\phi}} d\phi) = \int_0^{2\pi} H_\phi r \sin \theta d\phi = jB_{00} \frac{2\pi e^{-j\beta r}}{\mu}. \quad (2.115)$$

The characteristic impedance can now be found from the ratio of (2.114) and (2.115) as

$$Z_0 = \frac{V(r)}{I(r)} = \frac{\beta}{2\pi\omega\epsilon} \ln \left[ \frac{\cot \left( \frac{\theta_1}{2} \right)}{\cot \left( \frac{\theta_2}{2} \right)} \right] = \frac{\eta}{2\pi} \ln \left[ \frac{\cot \left( \frac{\theta_1}{2} \right)}{\cot \left( \frac{\theta_2}{2} \right)} \right] = Z_{in}. \quad (2.116)$$

From 2.116, one of the most useful properties of conical lines is evident, namely the constant nature of  $Z_0$  with respect to  $r$ . This is in contrast with the often used radial lines, where  $Z_0$  is

a strong function of radial distance from the origin. Since the characteristic impedance is not a function of radial distance, it also represents the input impedance of an infinite line at its feed terminals. It is apparent that the transmission line in Fig. 2.1 is inherently a very broad band structure since its characteristic or input impedance is only a function of the geometry of the structure (the angle of the cones) and not of frequency. A plot of the input impedance versus the half-angle relationship  $\theta_2/\theta_1$  is shown in Fig. 2.2 for a range of  $\theta_2$  values.

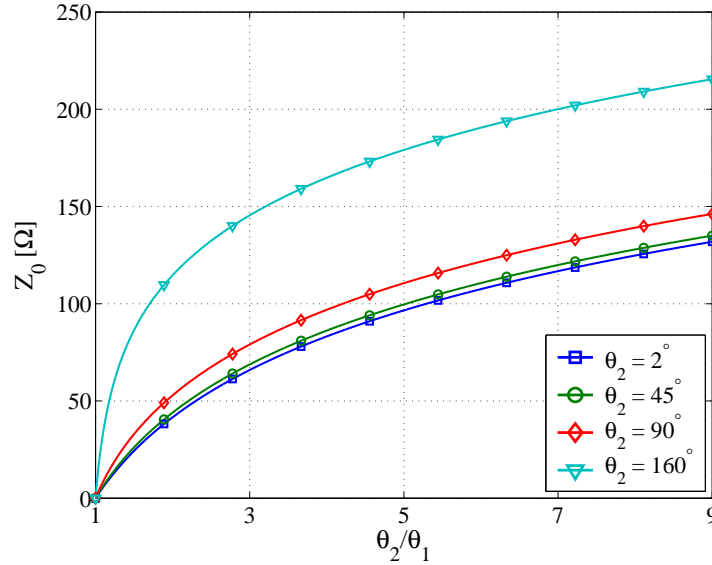


Fig. 2.2. Characteristic impedance of a conical line versus cone half-angles.

## 2.4 Associated Legendre Function and Transcendental Equation Solutions

Since very limited numerical results are available in the literature [22], and in order to obtain numerical results for the field distributions of the higher order modes in any conical transmission line, the transcendental equations (2.84) and (2.101) have to be solved for  $\nu$ . This requires accurate solutions of the nonnegative integer order associated Legendre functions up to very high positive real degrees (typically up to  $\nu > 50$ ). To accommodate all conical lines [ $\theta_1, \theta_2 \in (0, 180)^\circ$  with  $\theta_2 > \theta_1$ ], the argument of the functions should include all real  $z \in (-1, 1)$ . This is a very difficult task. A powerful mathematical software package such as Wolfram Research's *Mathematica* can be used to find these solutions, but for those without access to such software packages this section presents a systematic development which brings together a number of algorithms for solving the associated Legendre functions with different limitations on the parameters.

It is shown in [27] that when  $\text{Re}(\nu) \geq -0.5$ ,  $\text{Re}(\mu) \geq 0$ , and  $z$  ranges in the right half plane,  $P_\nu^{-\mu}(z)$  and  $Q_\nu^\mu(z)$  can be used to find any of the functions  $P_\nu^{\pm\mu}(z)$ ,  $P_{-\nu-1}^{\pm\mu}(z)$ ,  $Q_\nu^{\pm\mu}(z)$  or

$Q_{-\nu-1}^{\pm\mu}(z)$  through the use of connection formulas and recursion in  $\mu$  and  $\nu$ . The algorithms for calculating  $P_{\nu}^{-\mu}(z)$  and  $Q_{\nu}^{\mu}(z)$  are given in [28].

A less general method, though more suited to the problem at hand, is presented in [29]. When  $\nu$  is not an integer,  $P_{\nu}^m(x)$  and  $P_{\nu}^m(-x)$  are linearly independent and can be used to calculate  $Q_{\nu}^m(x)$  [where  $m$  is now a nonnegative integer and  $x \in (-1, 1)$ ]. The method uses two formulas to calculate  $P_{\nu}^m(x)$  for non-integer degrees in the ranges  $x \in (-1, -0.35)$  and  $x \in [-0.35, 1)$  respectively for  $\nu < 2$ . Forward recursion in  $\nu$  is applied for the higher degrees. To calculate the associated Legendre functions of integer order and degrees (also known as associated Legendre polynomials), recursion methods are used with the starting values given by known polynomials in  $x$ . This method for calculating the associated Legendre functions of the first and second kinds (the reason for calculating the second kind functions is given in the following subsection) is given in this section, as well as some comparisons of the results to those found with *Mathematica*.

#### 2.4.1 Use of the Associated Legendre Function of the Second Kind in the Transcendental Equations

Using the transcendental equations as given by (2.84) and (2.101) has the advantage that only  $P_{\nu}^m(\pm x)$  has to be computed. The problem with these equations is, however, that they have trivial solutions at integer values of  $\nu$ . This can be seen in the symmetry relation [29]

$$\frac{P_n^m(-z)}{P_n^m(z)} = (-1)^{n-m}, \quad (2.117)$$

with  $n$  a nonnegative integer. Substituting (2.117) into (2.84) and (2.101) shows the trivial solutions at integer orders and degrees for the transcendental equations. In order to find the non-trivial roots of these equations a search must be done between all the integers in the range of interest which will require a large number of function evaluations in the root finding algorithm. By rather choosing (2.56) as the solution for the  $\theta$ -varying field instead of (2.55), this problem can be avoided. This will result in two new transcendental equations, which have identical roots to the non-integer roots of (2.84) and (2.101), namely

$$\frac{dP_{\nu}^m(\cos \theta_1)}{d\theta_1} \frac{dQ_{\nu}^m(\cos \theta_2)}{d\theta_2} - \frac{dQ_{\nu}^m(\cos \theta_1)}{d\theta_1} \frac{dP_{\nu}^m(\cos \theta_2)}{d\theta_2} = 0 \quad (2.118)$$

and

$$P_{\nu}^m(\cos \theta_1)Q_{\nu}^m(\cos \theta_2) - Q_{\nu}^m(\cos \theta_1)P_{\nu}^m(\cos \theta_2) = 0. \quad (2.119)$$

The  $\theta$ -derivatives of the associated Legendre functions in (2.118) are given in Appendix A. Notice that when  $\nu = n$  and  $m > n$  trivial solutions are again found for (2.118) and (2.119) since  $P_n^m(z) = Q_n^m(z) = 0$ . Only the roots where  $\nu > m - 1$  will therefore be considered.

An alternative way of deriving (2.119) is simply to substitute the relation [29]

$$Q_\nu^m(x) = \frac{\pi}{2} \frac{P_\nu^m(x) \cos(\nu + m)\pi - P_\nu^m(-x)}{\sin(\nu + m)\pi} \quad (2.120)$$

into (2.101) to reduce it to

$$\frac{2}{\pi} \sin[(m + \nu)\pi] [P_\nu^m(\cos \theta_1) Q_\nu^m(\cos \theta_2) - Q_\nu^m(\cos \theta_1) P_\nu^m(\cos \theta_2)] = 0. \quad (2.121)$$

Since (2.121) also has trivial roots at the integer degrees ( $\nu \in \mathbb{Z}$ ), the sin part is divided out of the solution to leave

$$\frac{2}{\pi} [P_\nu^m(\cos \theta_1) Q_\nu^m(\cos \theta_2) - Q_\nu^m(\cos \theta_1) P_\nu^m(\cos \theta_2)] = 0. \quad (2.122)$$

This is the same result as (2.119) except for the constant factor. The same result also applies to the TE case in (2.118). All plots of the transcendental functions (2.118) and (2.119) will be done with the  $2/\pi$  factor included.

### 2.4.2 Solving the Associated Legendre Functions

The associated Legendre function of the first kind is defined as [27]

$$P_\nu^\mu(z) = \left(\frac{1+z}{1-z}\right)^{\mu/2} \left[ {}_2\tilde{F}_1\left(-\nu, \nu + 1; 1 - \mu; \frac{1-z}{2}\right) \right] \quad (2.123)$$

in terms of the regularised hypergeometric function given by

$${}_2\tilde{F}_1(a, b; c; z) = \sum_{k=0}^{\infty} \frac{(a)_k (b)_k z^k}{\Gamma(c+k) k!} \quad |z| < 1, \quad (2.124)$$

the Pochhammer symbol defined by

$$(a)_k = \frac{\Gamma(a+k)}{\Gamma(a)}, \quad (2.125)$$

and the gamma function defined by

$$\Gamma(z) = \int_0^{\infty} e^{-t} t^{z-1} dt \quad (\text{Re } z > 0). \quad (2.126)$$

Since  $Q_\nu^m(x)$  can easily be obtained from  $P_\nu^m(x)$  and  $P_\nu^m(-x)$  using (2.120) when  $\nu$  is not an integer, it is sufficient to only calculate  $P_\nu^m(x)$  and  $P_\nu^m(-x)$  from the definition. Formulas for the integral order case,  $P_\nu^m(x)$ , are [29]

$$P_\nu^m(x) = (-1)^m \frac{(1-x^2)^{m/2}}{2^m m!} \frac{\Gamma(\nu+m+1)}{\Gamma(\nu-m+1)} \sum_{k=0}^{\infty} \frac{(-\nu+m)_k (\nu+1+m)_k}{k! (m+1)_k} \left(\frac{1-x}{2}\right)^k \quad (2.127)$$

which converges quickly for  $x \in (0, 1)$ , and

$$\begin{aligned}
P_\nu^m(x) = & -\frac{\sin \nu \pi}{\pi} (m-1)! \left(\frac{1-x}{1+x}\right)^{m/2} \sum_{k=0}^{m-1} \frac{(-\nu)_k (\nu+1)_k}{k! (1-m)_k} \left(\frac{1+x}{2}\right)^k \\
& + \frac{\sin \nu \pi}{\pi} \frac{(1-x^2)^{m/2}}{2^m m!} \frac{\Gamma(\nu+m+1)}{\Gamma(\nu-m+1)} \sum_{k=0}^{\infty} \frac{(-\nu+m)_k (\nu+1+m)_k}{k! (k+m)!} \left(\frac{1+x}{2}\right)^k \\
& \times \left[ \psi(-\nu+m+k) + \psi(\nu+1+m+k) - \psi(1+m+k) - \psi(1+k) + \ln \frac{1+x}{2} \right]
\end{aligned} \tag{2.128}$$

which converges quickly for  $x \in (-1, 0)$ . The first term of (2.128) drops out when  $m = 0$ . The digamma function denoted by  $\psi(z)$  is given by

$$\psi(z) = \frac{d[\ln \Gamma(z)]}{dz} = \frac{\Gamma'(z)}{\Gamma(z)}. \tag{2.129}$$

For the integral degree case, (2.128) reduces to a polynomial with a finite summation

$$P_n^m(x) = (-1)^n \frac{\Gamma(n+m+1)}{\Gamma(n-m+1)} \frac{(1-x^2)^{m/2}}{2^m m!} \sum_{k=0}^{n-m} \frac{(-n+m)_k (n+1+m)_k}{k! (k+m)!} \left(\frac{1+x}{2}\right)^k. \tag{2.130}$$

Direct summation of (2.127) is very difficult to do accurately because of the very large numbers generated by the gamma functions. Instead a function of the form

$$\sum_{k=0}^{\infty} \alpha_k x^k \tag{2.131}$$

can be written as

$$\begin{aligned}
\sum_{k=0}^K (\alpha)_k x^k &= (\alpha)_0 + x [(\alpha)_1 + x [\dots + x [(\alpha)_{K-1} + x(\alpha)_K]]] \\
&= (\alpha)_0 \left[ 1 + \frac{(\alpha)_1}{(\alpha)_0} x \left[ 1 + \frac{(\alpha)_2}{(\alpha)_1} x [\dots] \right] \right].
\end{aligned} \tag{2.132}$$

It can easily be shown that the ratios in (2.132) reduce to

$$\frac{(\alpha)_k}{(\alpha)_{k-1}} = \alpha + k - 1. \tag{2.133}$$

Since all the factors in (2.127) can be related to the Pochhammer symbol through (2.125), it is not necessary to solve the Pochhammer symbol in the summation. Instead, only multiplication of vectors of the form  $[\alpha+n-1]$ , with  $n = 1, 2, 3, 4, \dots, K$ , is needed.  $K$  can be chosen arbitrarily large, depending on the accuracy required. To calculate the infinite sums in (2.128), (2.132) can be expanded to include the extra functions with  $k$  dependence as

$$\begin{aligned}
\sum_{k=0}^K (\alpha)_k \beta(k) x^k &= (\alpha)_0 \beta(0) + x [(\alpha)_1 \beta(0) + x [\dots + x [(\alpha)_{K-1} \beta(K-1) + x(\alpha)_K \beta(K)]]] \\
&= (\alpha)_0 \beta(0) \left[ 1 + \frac{(\alpha)_1}{(\alpha)_0} \frac{\beta(1)}{\beta(0)} x \left[ 1 + \frac{(\alpha)_2}{(\alpha)_1} \frac{\beta(2)}{\beta(1)} x [\dots] \right] \right].
\end{aligned} \tag{2.134}$$

Since the digamma function does not become very large for large arguments, it is no problem to calculate it directly. The vectors used to represent the Pochhammer symbol (2.133) are simply point multiplied by the vectors representing the ratios  $\beta(k)/\beta(k-1)$  and used in (2.134).

This method for solving the associated Legendre function of the first kind is however only stable for  $\nu$  up to about 25. To find the results for larger  $\nu$  values a recursive scheme is used. A well known recursive relationship for the Legendre functions with varying degree is [29]

$$X_{\nu}^{\mu}(x) = \frac{1}{\nu - \mu} [(2\nu - 1)xX_{\nu-1}^{\mu}(x) - (\nu + \mu - 1)X_{\nu-2}^{\mu}(x)], \quad (2.135)$$

where  $X_{\nu}^{\mu}(z)$  can be used to represent either of the first or second kind functions i.e.  $P_{\nu}^{\mu}(z)$  or  $Q_{\nu}^{\mu}(z)$ . For non integer degrees  $\nu < 2$  (2.127) is used to find the function value for  $x \in (-0.35, 1)$  and (2.128) is used for  $x \in (-1, -0.35)$ . For the integer degrees  $n = 0$  and  $n = 1$  (2.130) is used to find the function value. The relationship in (2.135) is then used to find the values for higher degrees. A comparison of the results with and without recursion is shown in Fig. 2.3.

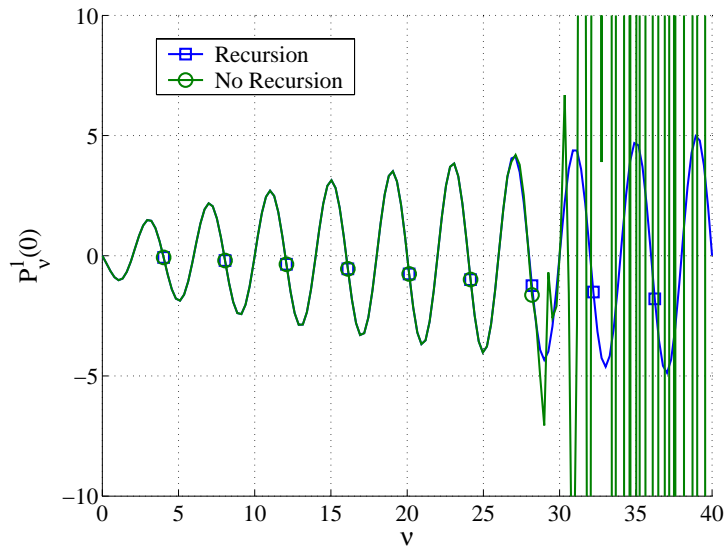


Fig. 2.3. Comparison of the computed results of the Legendre function of the first kind using a recursive scheme to those found without using recursion.

Calculating the associated Legendre function of the second kind for non-integer degrees is simply done by calculating the first kind functions as described above for positive and negative arguments and then using (2.120). For the integer degree case (associated Legendre polynomials of the second kind), the starting values  $Q_0^0(x)$ ,  $Q_1^0(x)$ ,  $Q_0^1(x)$  and  $Q_1^1(x)$  are calculated from the

known polynomials [29]

$$\begin{aligned}
 Q_0^0(x) &= \frac{1}{2} \ln \frac{1+x}{1-x} \\
 Q_1^0(x) &= \frac{x}{2} \ln \frac{1+x}{1-x} - 1 \\
 Q_0^1(x) &= -(1-x^2)^{-1/2} \\
 Q_1^1(x) &= -(1-x^2)^{1/2} \left( \frac{1}{2} \ln \frac{1+x}{1-x} + \frac{x}{1-x^2} \right).
 \end{aligned} \tag{2.136}$$

$Q_n^0(x)$  and  $Q_n^1(x)$  is then calculated for  $n = 2, 3, 4, \dots$  using (2.135), and  $Q_n^m(x)$  can then be calculated for  $m = 2, 3, 4, \dots$  using the recurrence relation [29]

$$X_\nu^\mu(x) = -\frac{2(\mu-1)}{\sqrt{1-x^2}} x X_\nu^{\mu-1}(x) - (\nu+\mu-1)(\nu-\mu+2) X_\nu^{\mu-2}(x). \tag{2.137}$$

### 2.4.3 Solving the Transcendental Equations

Plots showing the comparison between the transcendental functions using only the associated Legendre functions of the first kind [(2.84) and (2.101)] (P-type) and those using the both the first and the second kind [(2.118) and (2.119)] (mixed-type) are shown in Fig. 2.4

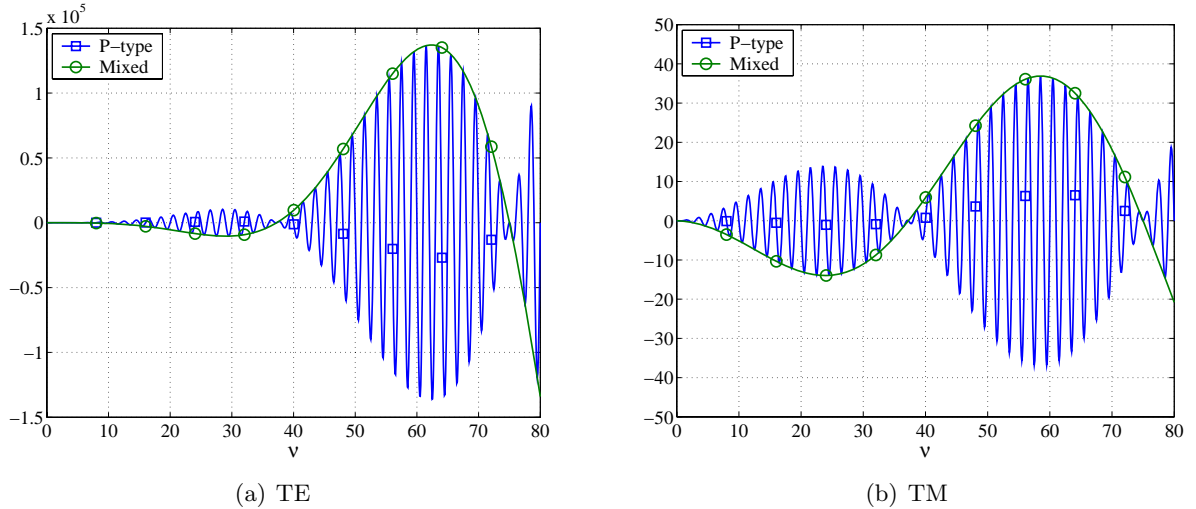


Fig. 2.4. Comparison of the P- and mixed-type transcendental functions for  $m = 1$ ,  $\theta_1 = 85.23^\circ$  and  $\theta_2 = 90^\circ$ .

From Fig. 2.4 it can clearly be seen that finding the roots of the mixed-type function is much simpler than finding the non-integer roots of the P-type function. A standard MATLAB function is used in the root finding algorithm to find the local minima of the absolute value of the transcendental functions in the areas where a sign change is observed in the function value when the function is evaluated in steps along the  $\nu$  axis.

The roots found by a MATLAB implementation of the above theory were compared to the roots found by using standard *Mathematica* functions for a wide range of the parameters. The first three TE and TM roots were calculated for  $m = 0, 1$  and  $2$  for the cases where first  $\theta_2$  was varied between  $10^\circ$  and  $90^\circ$  and  $\theta_1$  was chosen to give a  $50 \Omega$  line impedance, and also where  $\theta_2 = 22.5^\circ$  and  $\theta_1$  is varied to give line impedances of  $Z_0 = 10, 25, 50, 75, 100$  and  $125 \Omega$ . The line impedance is calculated using (2.116). Roots were also computed for  $\theta_2 = 90^\circ$  and  $\theta_1 = 85.231^\circ$  ( $5 \Omega$  line impedance) for  $m = 1 : 15$ . All the results agree to at least 5 significant digits.

## 2.5 Modal Cutoff Frequencies

### 2.5.1 Definition of Cutoff Wavelength

In a conical transmission line the concept of guide wavelength loses its customary significance because of the non-periodic nature of the field variation in the transmission direction ( $r$ -direction). Consequently, the usual relation between guide wavelength and cutoff wavelength is no longer valid. Normally the cutoff wavelength is defined at the point where the propagation constant goes from purely real to purely imaginary. This is also the point where the wave impedance changes from purely real to purely imaginary. In a conical transmission line, however, the wave impedance of the  $\text{TE}^r$  modes is given by

$$Z_w^{+r} = \frac{E_\theta}{H_\phi} = -\frac{E_\phi}{H_\theta} = -\frac{\hat{H}_\nu^{(2)}(\beta r)}{\frac{1}{j\omega\mu} \frac{d}{dr} \hat{H}_\nu^{(2)}(\beta r)} = -j\beta\eta \frac{\hat{H}_\nu^{(2)}(\beta r)}{\frac{d}{dr} \hat{H}_\nu^{(2)}(\beta r)}. \quad (2.138)$$

This impedance is complex for all values of the argument  $\beta r$ , with the imaginary part tending to zero and the real part to  $\eta$  as  $\beta r \rightarrow \infty$  (see Fig. 2.5 and [30, 31]). A similar result is obtained for the TM modes.

The conical transmission line therefore belongs to the class of waveguides that display gradual cutoff. Other waveguides in this class include radial waveguides [20], sectoral horns [9], and free space as a waveguide [20]. The point of gradual cutoff of a mode is not only dependent on frequency, but also on the spatial coordinates.

The radial wave impedance in a parallel-plate radial transmission waveguide is very similar to (2.138), except that the values of  $\nu$  are now restricted to integers  $n$ . The modified spherical Hankel functions are also replaced by normal Hankel functions. Harrington [20] shows that a mode is propagating when the wave impedance is predominantly real, and is non-propagating when the impedance is predominantly imaginary. He denotes the point where  $\beta\rho = n$  (with  $\rho$  being the distance from the origin in cylindrical coordinates) the point of gradual cutoff, since at this point the real part of the impedance starts to dominate the imaginary part. This means

a mode is propagating when  $\beta\rho > n$  and non-propagating when  $\beta\rho < n$ . Note that these gradual cutoffs occur when the circumference of the radial waveguide is an integral number of wavelengths.

The sectoral horn described by Ramo, Whinnery and Van Duzer [9] has the same radial wave impedance as a parallel-plate radial waveguide, with the order of the Hankel functions no longer restricted to integer values. The gradual cutoff is also described in terms of the real and imaginary components of the wave impedance and is again defined at the point  $\beta\rho = \nu$ .

When the spherical wave functions described in Section 2.2 are solved in a complete spherical shell region ( $0 \leq \theta \leq \pi$ ,  $0 \leq \phi \leq 2\pi$ ), only the associated Legendre function of the first kind of integral degree,  $P_{\nu=n}^{\mu}(\cos \theta)$ , must be chosen as the  $\theta$ -dependent solution in order for the fields to be finite everywhere. The rest of the solutions are the same as those described for the conical transmission line. The fields specified by these wave functions can be thought of as the modes of free space. When viewed in this manner, free space is often called a spherical waveguide, even though there is no material guiding the waves. Harrington [20] again denotes the point where  $\beta r = n$  as the point of gradual cutoff in exactly the same manner as for the parallel-plate radial transmission line. The gradual cutoff again occurs where the circumference is an integral number of wavelengths. Chu [32] described this gradual cutoff phenomenon in terms of a high pass filter ladder network by expanding the wave impedance of the modes using the recurrence formulas for spherical Bessel functions. Using this circuit model, it can be seen that when a mode is non-propagating, the energy in the circuit is mainly reactive, and when a mode is propagating, the energy is dissipated as real power. It is also clear that, for a fixed  $r$ , the higher the frequency, the more power is transmitted by a spherical waveguide mode.

For a conical transmission line a very similar expression is defined in the literature [8, 22] for the point of gradual cutoff (or cutoff wavelength,  $\lambda_c$ ) as

$$\lambda_c = \frac{2\pi r}{\sqrt{\nu(\nu+1)}}, \quad (2.139)$$

where  $\nu$  represents the the roots of the transcendental functions (2.84) and (2.101) for the TE and TM modes respectively. Equation (2.139) could be rewritten as

$$\beta r = \sqrt{\nu(\nu+1)}, \quad (2.140)$$

where it is now understood that the regions where  $\beta r < \sqrt{\nu(\nu+1)}$  the mode is below cutoff (non-propagating), and where  $\beta r > \sqrt{\nu(\nu+1)}$  the mode is above cutoff (propagating). A plot of the normalised real and imaginary wave impedance is shown for the case where  $\sqrt{\nu(\nu+1)} = 1$  in Fig. 2.5. From Fig. 2.5 it can be seen that the maximum value of the real impedance is reached when  $\beta r = \sqrt{\nu(\nu+1)} = 1$ . This is consistent with the remarks in [20, 9] that above cutoff the real wave impedance dominates the imaginary impedance of the mode.

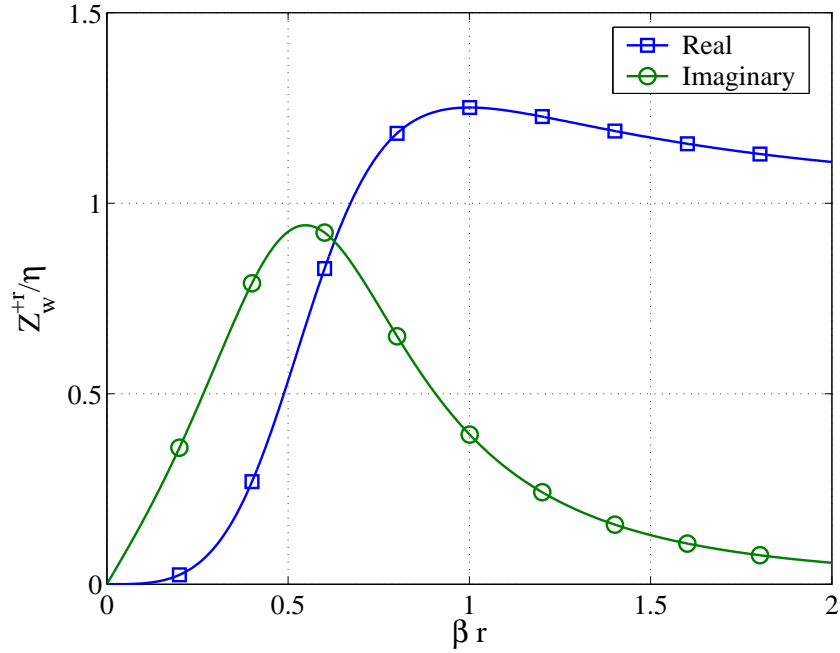


Fig. 2.5. Normalised TE wave impedance of a conical transmission line.

Another definition for gradual cutoff in conical lines is given by Marcuvitz [8, 33] in terms of the spatial decay of the mode fields. In conical transmission lines (and similar structures such as radial waveguides) there is an overall decrease in the amplitude of the waves in the  $r$ -direction due to spherical (or cylindrical) spreading of the waves. Marcuvitz states that in regions where  $\lambda < \lambda_c$  the mode fields decay spatially like  $1/r$  and hence may be termed propagating, and conversely, for  $\lambda > \lambda_c$  the mode fields decay faster than  $1/r$  and may therefore be termed non-propagating. No proof of this statement could be found in literature, and a simplified proof in terms of the Cauchy-Euler Equation [34, 35] will be presented here for a conical transmission line.

From (2.86) to (2.91) the  $r$ -direction spatial dependence of the TE-mode fields is proportional to  $\hat{H}_\nu^{(2)}(\beta r)/r$ . When (2.64) is considered, this spatial  $r$ -dependence is found to be proportional to  $\beta h_\nu^{(2)}(\beta r)$ . Equation (2.66) is the differential equation describing the  $r$ -dependence of the mode fields, yielding solutions of the form  $h_\nu^{(2)}(\beta r)$  [ $\beta h_\nu^{(2)}(\beta r)$  is also a solution since the  $\beta$  factor can just be eliminated from the equation]. This differential equation (2.66) can be rewritten as

$$r^2 \frac{d^2 f}{dr^2} + 2r \frac{df}{dr} + af = 0, \quad (2.141)$$

which is known as a second order Cauchy-Euler equation if  $a$  is independent of  $r$ . If  $a$  is chosen such that  $a = (\beta r)^2 - \nu(\nu + 1)$ , (2.141) is not a pure Cauchy-Euler equation, but it can still be used to prove Marcuvitz's statement. In terms of propagating and non-propagating regions

from (2.140), three possible cases for  $a$  exist, namely

$$a > 0 \quad \text{propagating,} \quad (2.142)$$

$$a = 0 \quad \text{cutoff,} \quad (2.143)$$

$$a < 0 \quad \text{non-propagating.} \quad (2.144)$$

These three cases will be considered in the Cauchy-Euler equation (2.141) with  $a$  taken as constant for the three cases. Solutions to (2.141) are found as  $f = r^m$ , where  $m$  is a solution of the auxiliary equation [34, 35]

$$m^2 + m + a = 0. \quad (2.145)$$

For distinct real roots to (2.145) the general solution to (2.141) is found as

$$f = c_1 r^{m_1} + c_2 r^{m_2}, \quad (2.146)$$

for repeated real roots as

$$f = c_1 r^{m_1} + c_2 r^{m_1} \ln r, \quad (2.147)$$

and for complex conjugate roots  $m = \mathcal{R} \pm j\mathcal{X}$  as

$$f = r^{\mathcal{R}} [c_1 \cos(\mathcal{X} \ln r) + c_2 \sin(\mathcal{X} \ln r)]. \quad (2.148)$$

The solutions to the auxiliary equation (2.145) are given by

$$m_{1,2} = \frac{-1 \pm \sqrt{1 - 4a}}{2}. \quad (2.149)$$

For the three different cases described in (2.142) to (2.144), the nature of the roots ( $m_{1,2}$ ) is as follows:

1. When  $a = 0$  the solutions to (2.149) are  $m_1 = 0$  and  $m_2 = -1$ . The solution to (2.141) would thus be from (2.146) proportional to  $f = 1/r$ .
2. When  $a < 0$  the dominant solution (largest absolute value) to (2.149) is always  $m_2 < -1$ , and the solutions will always be distinct and real. The dominant solution to (2.141) will thus be from (2.146) proportional to  $f = r^{m_2}$ , and this is seen to decay faster than  $1/r$ .
3. When  $a > 0$  the situation becomes a bit more complex. Any of the solutions of the forms (2.146) to (2.148) could be found to (2.149). For the case of distinct real roots, the dominant solution to (2.149) will always fall in the range  $-1 < m_2 < 0.5$ , yielding a solution to (2.141) of the form  $f = r^{m_2}$  that decays slower than  $1/r$ . Repeated roots are found for  $a = 0.25$  as  $m_1 = m_2 = -0.5$ , which from (2.147) again yields a solution to (2.141) which decays slower than  $1/r$ . The real part of the complex roots will always be  $\mathcal{R} = -0.5$ , which will according to (2.148) also yield a solution to (2.141) which decays slower than  $1/r$  on average.

The above results, together with the statements in (2.142) to (2.144), serves to prove Marcuvitz's statement that the propagating mode fields decay at (or slower than)  $1/r$ , and the non-propagating mode fields decay faster than  $1/r$ . It also serves as a useful explanation as to why (2.139) was chosen as the cutoff wavelength.

It is important to note that within waveguides with gradual cutoff properties at a specific frequency, the same mode can be propagating within a certain region of the waveguide, and be non-propagating in another region. This gives rise to the idea of a cutoff radius which is sometimes used in the literature to describe such waveguides. The cutoff radius of a mode is the minimum radius where the mode is propagating at a certain frequency, where it is again emphasised that there is a gradual transition from the non-propagating to the propagating region.

### 2.5.2 Numerical Results

As stated earlier, very little numerical data is available in the literature regarding the cutoff wavelengths of the higher order modes in a conical transmission line. This is mainly due to the difficulty involved in solving the transcendental equations (2.84) and (2.101). In 2001 Weil *et al.* [22] published a range of numerical results for the cutoff wavelengths, and qualitatively compared their results to similar results for a cylindrical coaxial transmission line. The new data for the conical transmission line was seen to be in good qualitative agreement with the well known data for the normal coaxial transmission line.

In order to check the accuracy of the roots found by the method described in Section 2.4, the results for the cutoff wavelength, which are directly dependent on the solutions for  $\nu$  as can be seen from (2.139), will be reproduced and compared to those by Weil *et al.* [22]. The different modes will be represented as  $TE_{mn}$  and  $TM_{mn}$  where  $m$  is an integer as previously defined in (2.77), and  $n$  represents the  $n$ th non-integer root of the transcendental equations (2.118) and (2.119) of order  $m$ , namely  $\nu_{mn}$ . The  $m$  modal subscript indicates variations in the  $\phi$ -direction and the  $n$  modal subscript indicates variations in the  $\theta$ -direction.

The data is computed for a relation between  $\theta_1$  and  $\theta_2$  to yield transmission line characteristic impedances of  $Z_0 = 10, 25, 50, 75, 100$  and  $125 \Omega$  from (2.116). The outer cone angle is chosen to be  $\theta_2 = 10^\circ$  and  $\theta_2 = 22.5^\circ$ . Plots will be shown for the normalised cutoff wavelength  $\lambda_c/r$  of the first three higher order  $TE_{m1}$  modes, as well as the  $TM_{01}$ ,  $TM_{11}$ ,  $TE_{12}$  and  $TM_{02}$  modes.

Figs. 2.6 and 2.7 correspond exactly to the plots published in [22]. These results prove the accuracy of the root finding procedure to be used for later calculations. It is interesting to note that the  $TE_{m1}$  modes dominate for low impedance lines ( $\theta_1 \approx \theta_2$ ), and that the cutoff

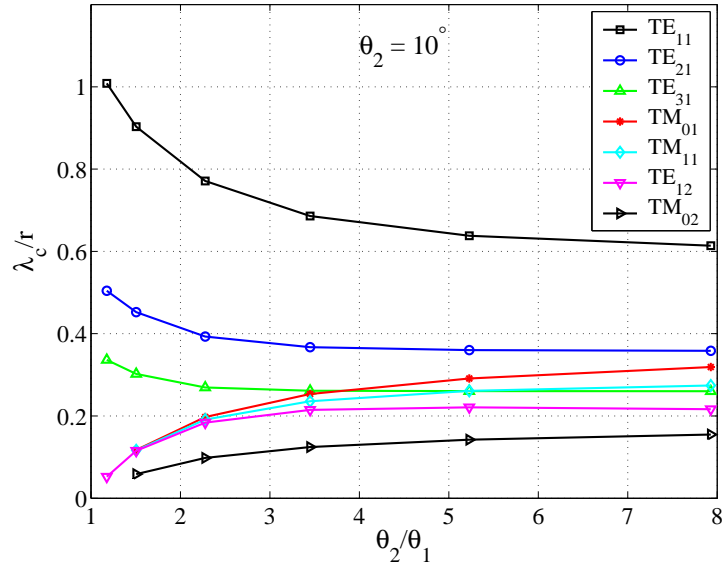


Fig. 2.6. Normalised cutoff wavelength of higher order modes in a conical transmission line with  $\theta_2 = 10^\circ$ .

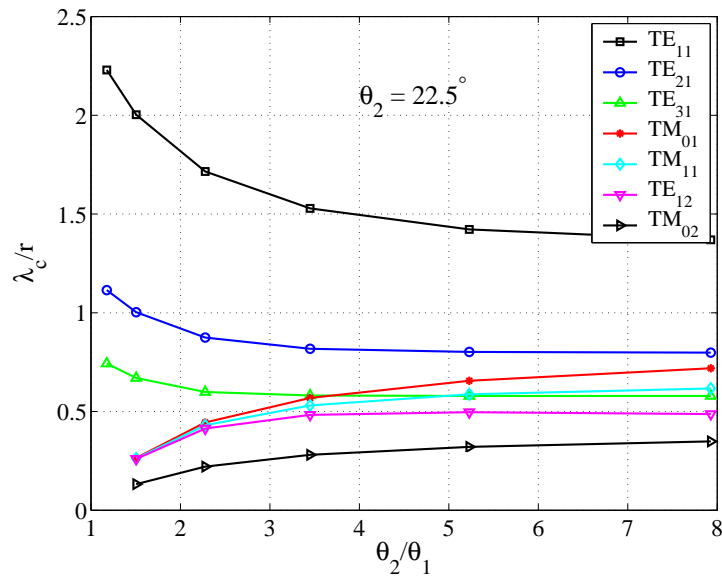


Fig. 2.7. Normalised cutoff wavelength of higher order modes in a conical transmission line with  $\theta_2 = 22.5^\circ$ .

wavelength of all the modes is longer for a larger  $\theta_2$ . These effects will be considered in more detail later.

## 2.6 Modal Plots

Very little data is available in the literature on the shape of higher order modes in conical transmission lines. Qualitative data exists for TE and TM modes in bi-conical antennas [18, 19, 23], but these structures typically have wide spacings between the cones ( $\theta_2 - \theta_1 = \text{large}$ ). This means the modes are usually plotted on the  $y$ - $z$  or  $x$ - $z$  planes, and no information about the spatial variation of the fields in the  $\phi$ -direction is seen. When a conical transmission line is used as a power combiner, the impedance of the line is typically very low and it can be seen from Fig. 2.2 that the spacings between the cones become very narrow ( $\theta_2 - \theta_1 = \text{small}$ ). Since the combining ports typically lie at a constant radius (or, along the  $\phi$ -axis), it is very important to know the spatial variation of the modal fields with respect to  $\phi$ . In this section these plots will be generated from the analytical model obtained earlier. All plots will be made with  $\theta_2 = 90^\circ$  in order to be able to plot the fields easily on the  $x$ - $y$  plane.

### 2.6.1 Travelling Wave Solutions

For the modal field plots, a geometry consistent with the proposed power combiner structure will be chosen. A line impedance of  $Z_0 = 5 \Omega$  with  $\theta_2 = 90^\circ$  and thus from (2.116)  $\theta_1 = 85.23^\circ$  is used. The outer radius of the line is chosen as  $r = 50$  mm.

Using these parameters the cutoff frequencies of the higher order modes are calculated at  $r = 50$  mm, since this is the region in the structure with the lowest cutoff frequency. This is found by substituting

$$f = \frac{c}{\lambda}, \quad (2.150)$$

where  $c$  is the speed of light in free space, into (2.139) to find

$$f_c = \frac{c\sqrt{\nu(\nu+1)}}{2\pi r}. \quad (2.151)$$

The lowest TM mode cutoff frequencies are found for the  $\text{TM}_{01}$ ,  $\text{TM}_{11}$  and the  $\text{TM}_{21}$  modes, and these are all around 36 GHz. These frequencies make intuitive sense, since the electric field of the TM modes must be zero at  $\theta = \theta_{1,2}$ , and in order to achieve that, the distance along an arc of constant  $r = 50$  mm from  $\theta = \theta_1$  to  $\theta = \theta_2$  (arc length) must be approximately half a wavelength. For a  $5 \Omega$  line the arc length at  $r = 50$  mm is 4.14 mm, which is half a wavelength at 36.2 GHz. This is much higher than the band of interest, and these modes can therefore be ignored. So too can the  $\text{TE}_{m2}$  and other  $\text{TE}_{mn}$  modes with  $n > 2$ , since the  $\text{TE}_{12}$  mode has the

lowest cutoff frequency of these modes of around 36 GHz (for the same reason as the TM modes –  $\theta$  variation of the electric field). The cutoff frequencies of the  $\text{TE}_{m1}$  modes are, however, much lower and these are plotted along the length of the transmission line for the first 15 modes in Fig. 2.8. Fig. 2.8 clearly illustrates the spatial dependence of the cutoff frequency of higher order

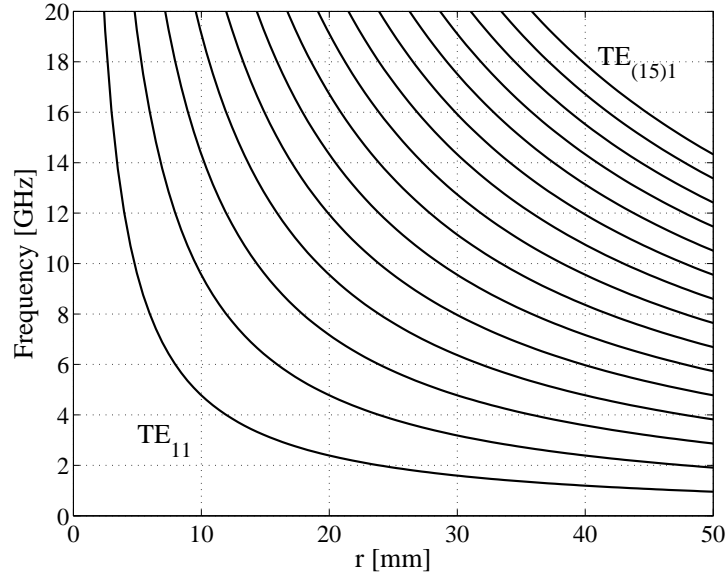


Fig. 2.8. Spatial variation of cutoff frequencies for the first 15  $\text{TE}_{m1}$  modes in a  $5 \Omega$  conical line with  $\theta_2 = 90^\circ$ .

modes in a conical transmission line. The regions where the modes are respectively propagating and non-propagating at a certain frequency are clearly visible. Again the cutoff wavelength of the  $\text{TE}_{m1}$  modes can be checked intuitively by noting that the roots of the transcendental equation (2.118),  $\nu_{mn}$ , when used in the equation for the cutoff wavelength (2.140), indicate that the cutoffs occur when the circumference of the conical transmission line is approximately an integral number of wavelengths (See Table 2.1).

TABLE 2.1

$\text{TE}_{m1}$  TRANSCENDENTAL EQUATION ROOTS SHOWING CUTOFF WAVELENGTHS OCCUR WHEN CIRCUMFERENCE IS APPROXIMATELY AN INTEGRAL NUMBER OF WAVELENGTHS.

$m$	$\nu_{m1}$	$2\pi r/\lambda_c$
1	0.62	1.00
2	1.56	2.00
3	2.54	3.00
4	3.54	4.00
5	4.53	5.01

The  $\theta$  dependent factor of the  $\text{TE}_{m1}$  mode fields [the Legendre function factors of (2.87) to (2.91)], vary very little in the region  $80^\circ < \theta < 90^\circ$ . A plot of a typical case ( $\text{TE}_{21}$ ) is shown in Fig. 2.9. It can be seen in Fig. 2.9 that the  $E_\phi$  and  $H_\theta$  components of the fields will be almost

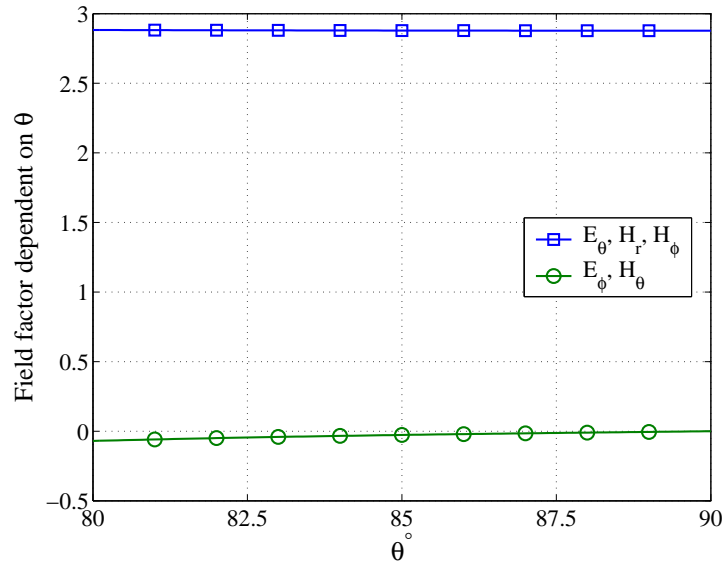


Fig. 2.9. Variation of the  $\theta$  dependent factors of the  $TE_{21}$  modal fields close to  $\theta = 90^\circ$ .

zero due to the very small  $\theta$  dependent factors. Therefore, the E-field will be mainly  $\theta$ -directed, and the H-field will have almost no component in the  $\theta$ -direction.

A plot on the  $x$ - $y$  plane of the first couple of  $TE_{m1}$  modes will therefore give a good representation of the higher order modal fields present in the described conical transmission line. Plots were generated in MATLAB, and the absolute value of the E-fields (all the E-fields are  $\theta$ -directed) and the absolute value and direction of the H-fields are shown for the TEM,  $TE_{11}$ ,  $TE_{21}$  and the  $TE_{51}$  modes at 10 GHz. Plots for the  $TE_{m1}$  modes are made at zero time ( $0^\circ$ ) and a quarter period later ( $90^\circ$ ) in order to clearly illustrate the behaviour of both the E- and the H-fields in their non-propagating regions. The cutoff radius is indicated by a black circle on the plots. The amplitude of the fields is shown on a dB scale.

In Figs. 2.10 to 2.16 the travelling wave properties of especially the lower order modes are clearly visible, with the wavefronts of these modes visible along the  $r$ -axis. It is also clear that large fields exist in the non-propagating regions, but they decay very quickly within these regions. Visually, these figures compare well to those produced by Schelkunoff [18, 19, 23] for modal field patterns in bi-conical antennas, and those produced by Harrington [20] for spherical waves in free space.

### 2.6.2 Standing Wave Solutions

In order to obtain quantitative data to compare the developed analytical results to, the eigenmode solver of CST-MWS can be used to obtain numerical standing wave solutions of a closed structure. If a normal conical transmission line is short circuited such a structure is obtained.

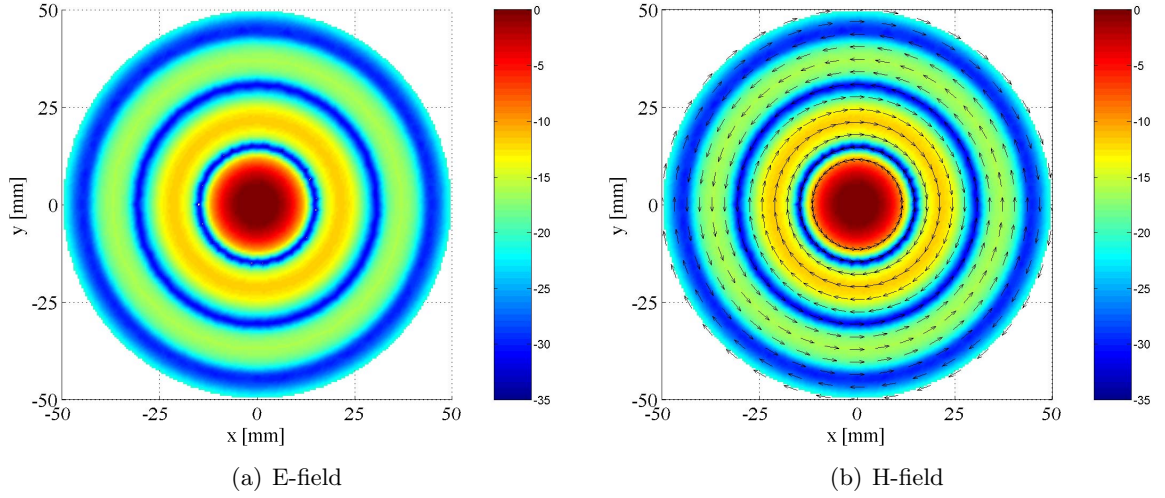


Fig. 2.10. Normalised absolute value (in dB) of the TEM modal fields at 10 GHz.

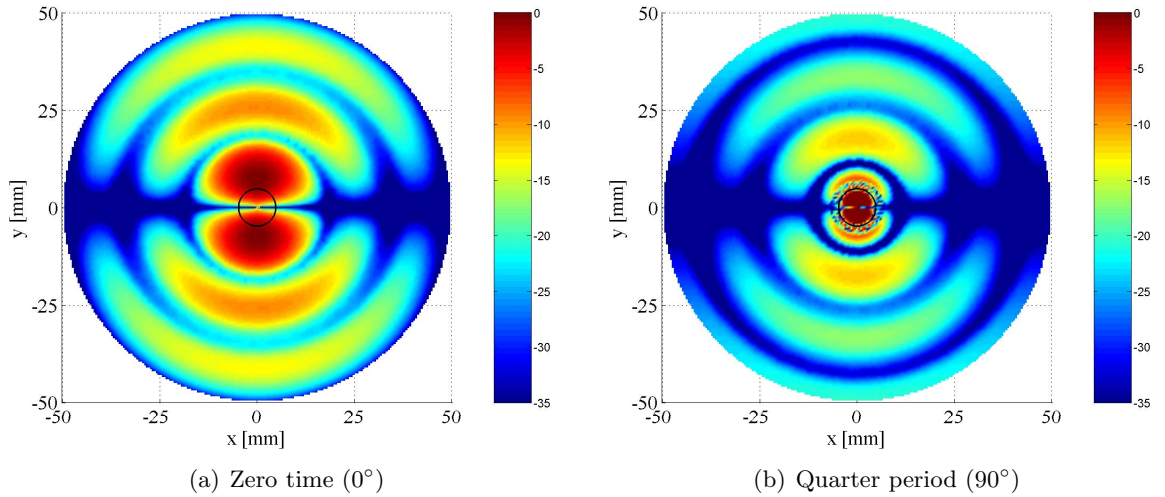


Fig. 2.11. Normalised absolute value (in dB) of the TE<sub>11</sub> E-field at 10 GHz.

This can easily be simulated in CST-MWS to obtain the resonant frequencies and field patterns of the higher order modes. An analytical model can be found by choosing the standing wave solution in the  $r$ -direction,  $\hat{f}_1(r)$  (2.67), to use in (2.77). The boundary condition on the  $\theta$ -axis stays the same as described in (2.78), and therefore all the solutions, (2.86) to (2.91), stay the same, except with the modified spherical Hankel functions  $[\hat{H}_\nu(\beta r)]$  replaced by modified spherical Bessel functions of the first kind  $[\hat{J}_\nu(\beta r)]$ . Only the  $\hat{J}_\nu(\beta r)$  part of the solution for  $\hat{f}_1(r)$  (2.67) is kept, since  $\hat{Y}_\nu(\beta r) \rightarrow \infty$  as  $r \rightarrow 0$ .

With the inclusion of the short circuit at  $r = r_0$  another boundary condition is introduced

$$E_\theta(r_0, \theta, \phi) = E_\phi(r_0, \theta, \phi) = 0. \quad (2.152)$$

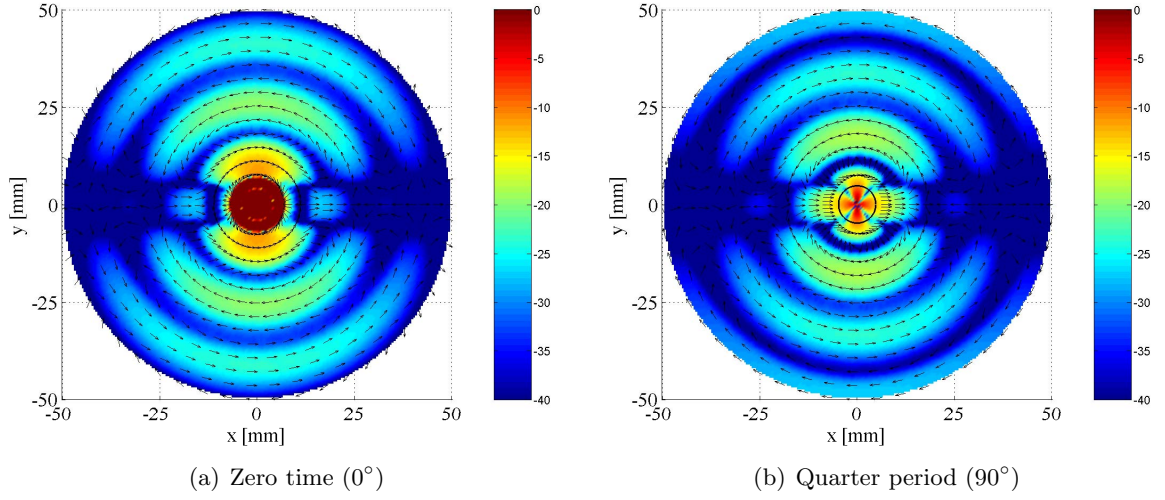


Fig. 2.12. Normalised absolute value (in dB) and direction of the  $TE_{11}$  H-field at 10 GHz.

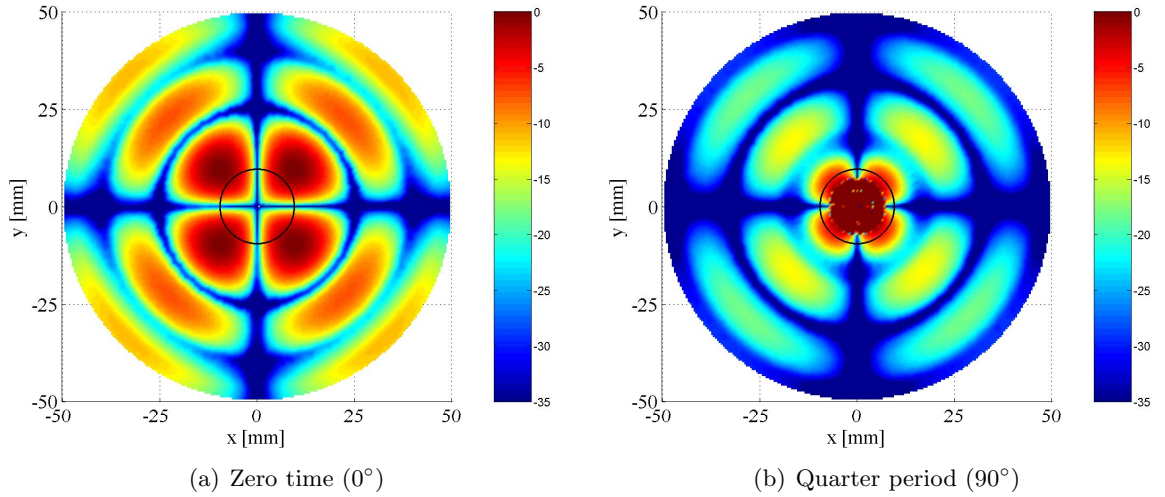


Fig. 2.13. Normalised absolute value (in dB) of the  $TE_{21}$  E-field at 10 GHz.

This can only be satisfied if

$$\hat{J}_\nu(\beta r_0) = \hat{J}_\nu(\zeta_{np}) = 0, \quad (2.153)$$

with  $\zeta_{np}$  representing the  $p$ th root of (2.153) with  $\nu$  chosen as the  $n$ th root of (2.118) for a certain integer  $m$  (only TE modes are considered for the same reasons as in the travelling wave case). The roots of (2.153) can easily be found with a simple root finding procedure in MATLAB. The resonant frequency of the  $TE_{mnp}$  mode is given by

$$f_{res} = \frac{c\beta}{2\pi}, \quad (2.154)$$

with  $\beta = \zeta_{np}/r_0$ .

As for the case of TEM travelling wave solutions (Section 2.3.3), the  $TM_{00p}$  modes are also present in the standing wave cavity structure. All the equations of Section 2.3.3 still hold,

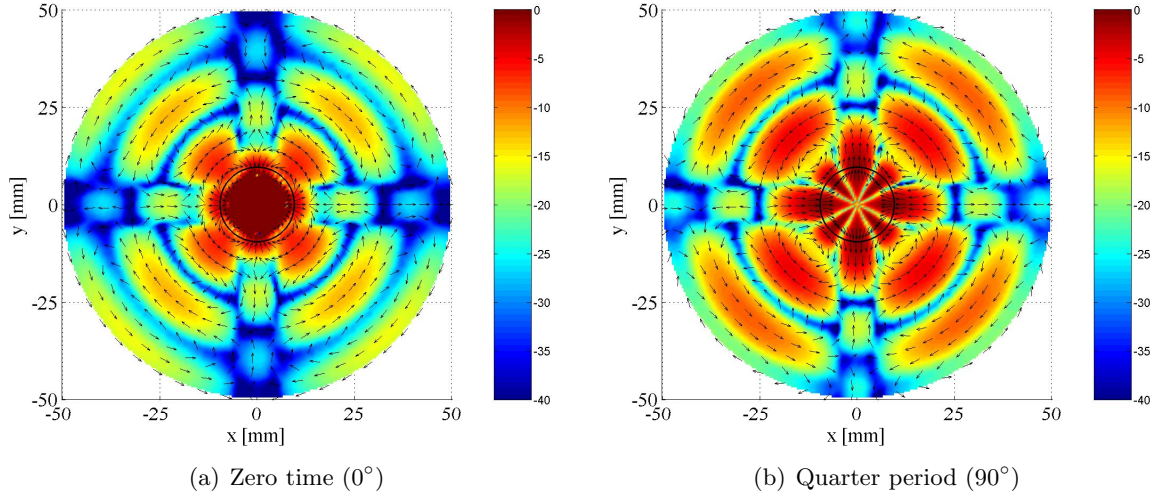


Fig. 2.14. Normalised absolute value (in dB) and direction of the  $TE_{21}$  H-field at 10 GHz.

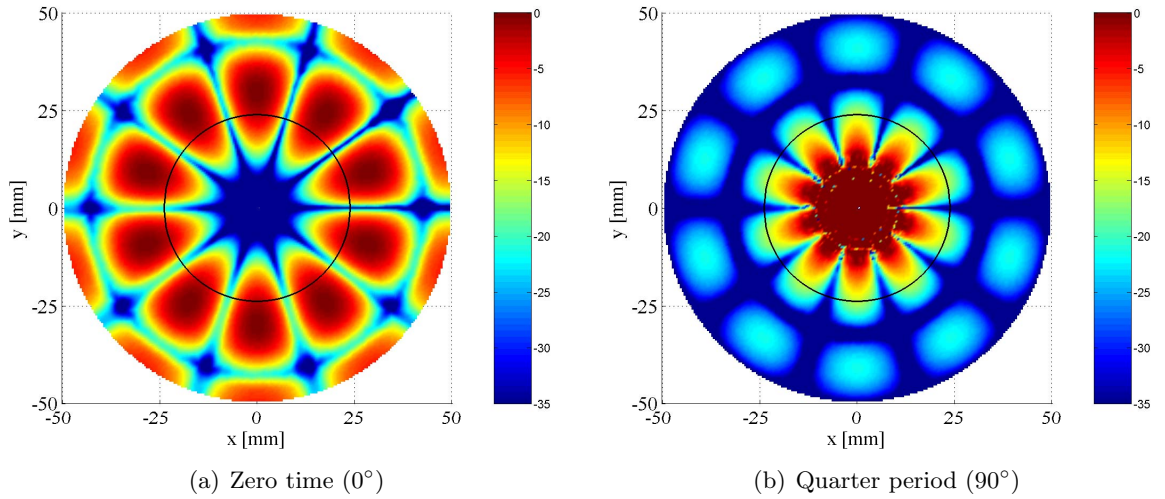


Fig. 2.15. Normalised absolute value (in dB) of the  $TE_{51}$  E-field at 10 GHz.

except that the travelling wave solution  $\hat{H}_0^{(2)}(\beta r)$  in (2.102) is replaced by the standing wave solution,  $A_{00}\hat{J}_0(\beta r) + B_{00}\hat{Y}_0(\beta r)$ , similar to the  $TE_{mnp}$  modes case. Using (2.64), and knowing that [20]

$$j_0(\beta r) = \frac{\sin \beta r}{\beta r} \quad (2.155)$$

$$y_0(\beta r) = -\frac{\cos \beta r}{\beta r}, \quad (2.156)$$

the spherical Bessel function of the first and second kind [ $\hat{J}_0(\beta r)$  and  $\hat{Y}_0(\beta r)$ ] can be replaced by their zero-order forms

$$\hat{J}_0(\beta r) = \sin \beta r \quad (2.157)$$

$$\hat{Y}_0(\beta r) = -\cos \beta r. \quad (2.158)$$

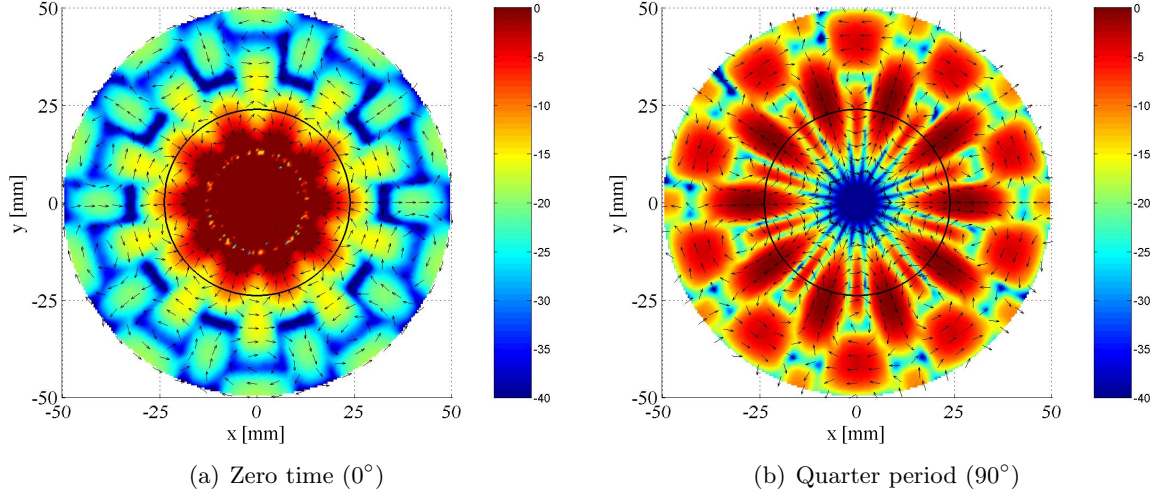


Fig. 2.16. Normalised absolute value (in dB) and direction of the  $TE_{51}$  H-field at 10 GHz.

The equation for the E-field (2.108) now becomes (for a finite field when  $r = 0$ )

$$E_{\theta} = jB_{00} \frac{\beta}{\omega\mu\epsilon} \frac{\sin \beta r}{r} \frac{1}{\sin \theta} \quad (2.159)$$

for the standing wave case. The boundary condition (2.152) can only be satisfied if

$$\frac{\sin \beta r}{r} = \frac{\sin \zeta_{np}}{r} = 0. \quad (2.160)$$

The  $p$ th root of (2.160) is thus  $p\pi$  and the resonant frequency of the  $TM_{00p}$  mode is found as

$$f_{res} = \frac{cp}{2r_0}. \quad (2.161)$$

For the structure described in Section 2.6.1 ( $Z_0 = 5 \Omega$ ,  $\theta_2 = 90^\circ$  and  $r_0 = 50$  mm), the analytical and CST-MWS simulation resonant frequencies of the first fourteen resonant modes are compared in Table 2.2. Note that all of the  $TE_{mnp}$  modes have two orthogonal degenerate modes, and only the resonant frequency of one of these is shown in Table 2.2. The results obtained in Table 2.2 are in very good agreement and only differ by about 0.2 % or less. These numerical results serve to prove the validity of the theory and root finding procedures. A comparison of the analytical and CST-MWS simulated E-fields is also included in Figs. 2.17 to 2.20 for the  $TM_{001}$ ,  $TE_{211}$ ,  $TE_{312}$  and  $TE_{113}$  modes at their respective resonant frequencies. The  $TE_{mnp}$  modes have two orthogonal degenerate modes, and only the  $\sin m\phi$  mode is shown in all the cases.

All of the analytical plots in Figs. 2.17 to 2.20 agree very well with the simulated results. The only discrepancy is in Fig. 2.17, where a zero in the simulated field is seen at the origin. This is due to the fact that in the simulation model no source was included at the apex of the cones, as was the original assumption in the derivation of the analytical model. Instead a short

TABLE 2.2

COMPARISON OF ANALYTICAL AND SIMULATED RESULTS FOR THE RESONANT FREQUENCIES OF THE FIRST FOURTEEN MODES IN A CONICAL CAVITY.

Mode	$f_{\text{res}}$ [GHz]		% Error
	Analytical	CST-MWS	
TM <sub>001</sub>	2.998	2.998	0.000
TE <sub>111</sub>	3.809	3.803	0.158
TE <sub>211</sub>	4.978	4.971	0.141
TM <sub>002</sub>	5.996	5.995	0.017
TE <sub>311</sub>	6.141	6.131	0.163
TE <sub>112</sub>	6.858	6.846	0.175
TE <sub>411</sub>	7.282	7.270	0.165
TE <sub>212</sub>	8.116	8.101	0.185
TE <sub>511</sub>	8.405	8.390	0.178
TM <sub>003</sub>	8.994	8.992	0.022
TE <sub>312</sub>	9.371	9.354	0.181
TE <sub>611</sub>	9.512	9.495	0.179
TE <sub>113</sub>	9.876	9.856	0.203
TE <sub>412</sub>	10.603	10.581	0.207

circuit exists at the apex in the simulation model due to the nature of the eigenmode solver in CST-MWS, and this causes the zero in the E-field at that point.

## 2.7 Conclusion

In this chapter a thorough description and theoretical analysis of conical transmission lines has been presented. The analytical solutions of the cutoff frequencies and the field patterns of the higher order modes in such a line are discussed, and calculation methods are given to find these solutions. Several plots of the results are shown, many of which could not be found in the literature. The analytical results found in this chapter compared very well to those found numerically with a full wave simulator. These analytical models of the possible field distributions in conical transmission lines can now be used to aid in the design of conical transmission line power combiners, as will be pursued in the following chapters of this dissertation.

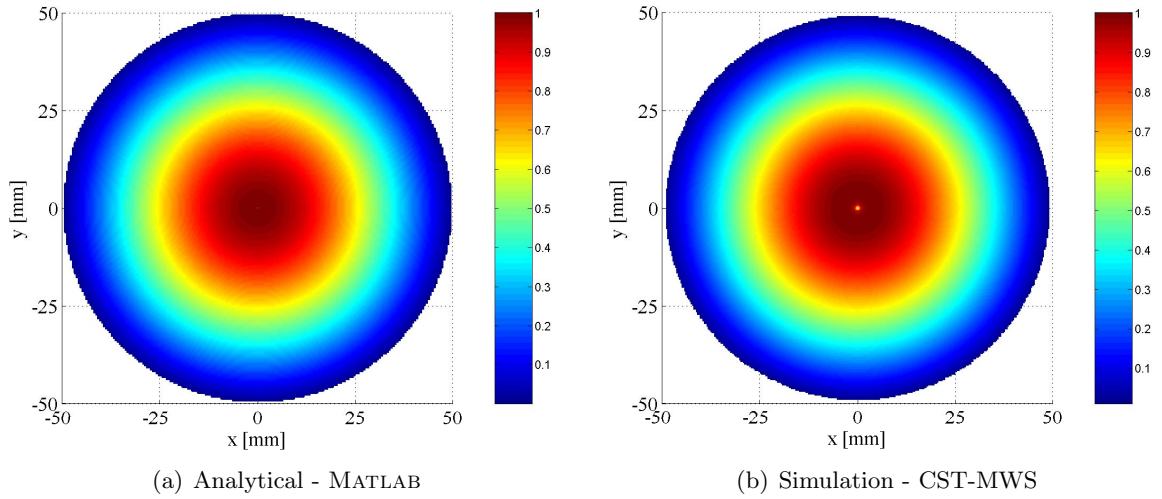


Fig. 2.17. Normalised absolute value of the E-field of the  $TM_{001}$  mode at 3.00 GHz.

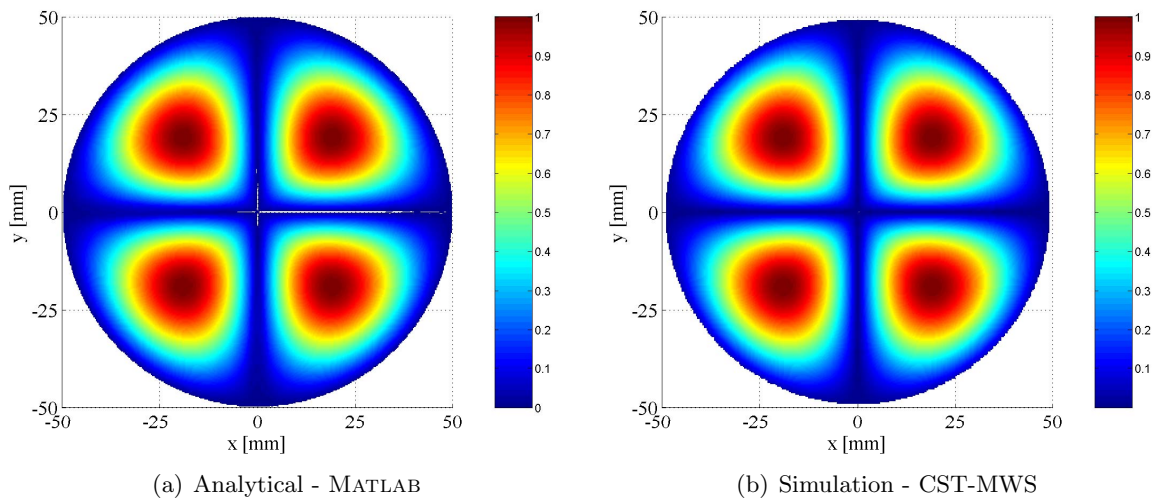


Fig. 2.18. Normalised absolute value of the E-field of the  $TE_{211}$  mode at 4.98 GHz.

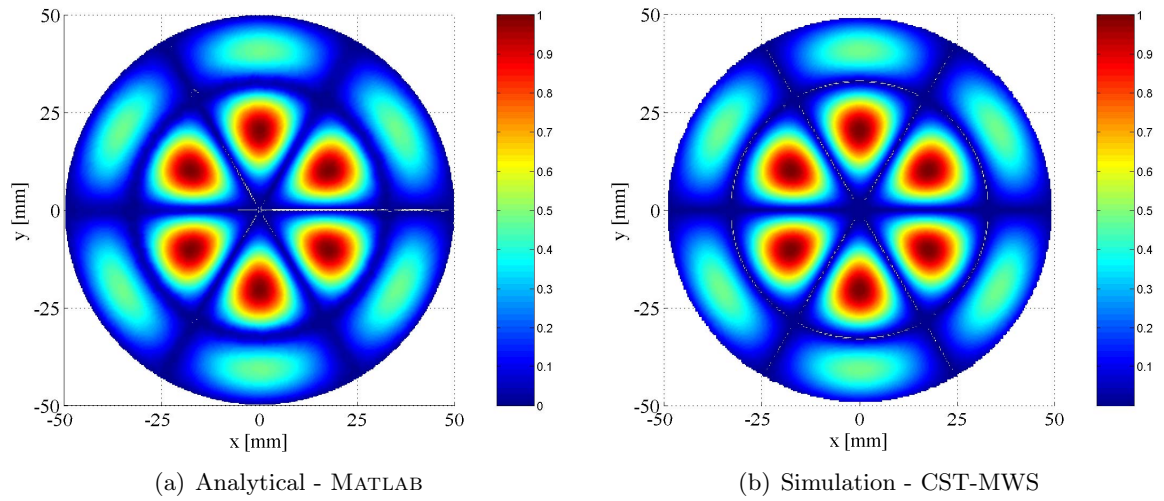


Fig. 2.19. Normalised absolute value of the E-field of the  $TE_{312}$  mode at 9.37 GHz.

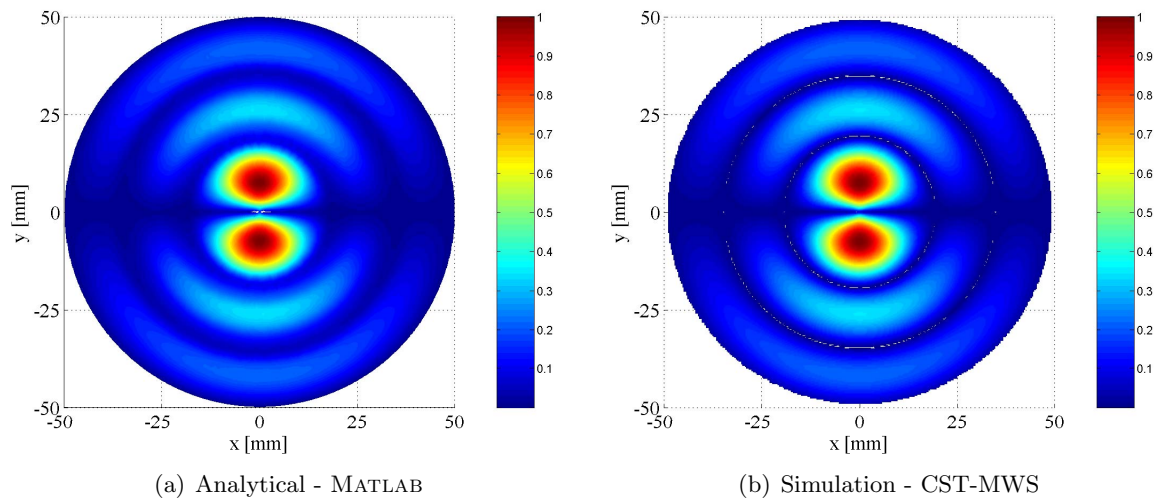


Fig. 2.20. Normalised absolute value of the E-field of the  $TE_{113}$  mode 9.88 GHz.

## Chapter 3

# A Basic 10-Way Conical Line Combiner

From Chapter 2 it emerged that conical lines, in contrast to radial lines, support a uniform TEM transmission line mode and therefore has a constant characteristic transmission line impedance with radial distance, and as discussed in the introduction, it is this property that makes conical lines potentially useful in the design of axially symmetric power combiners. In this chapter, such a power combiner for 10 input ports is proposed, designed and evaluated.

The initial design goals for this combiner are to achieve a good broadband match of the output port ( $S_{11} < -20$  dB across the X-band), as well as good balance across the input ports, and a low insertions loss. Only the TEM mode is considered in the initial design, and the effect of higher order modes (for instance on isolation) is investigated by full wave simulation of the final design. These effects are also investigated in some detail in Chapter 5.

To establish the context of the proposed combiner, ideal characteristics of  $N$ -way TEM combiners are briefly discussed, and the basic configuration of the conical combiner structure is explained. Attention is given to the transitions from the coaxial input ports into the conical line, and also from the conical line to the coaxial output port. The matching of the output port is discussed and the measured results of the constructed combiner are presented. Finally, the isolation as well as power handling capability of the combiner is discussed through some field simulation results.

### 3.1 Ideal $N$ -way TEM Combiners

To find a circuit model that describes the behaviour of a conical line combiner is very difficult due to the differences in physical separation between the peripheral ports, and to the higher order

modes present in the line when the structure is driven unsymmetrically. However, a simplified model can be used to get a qualitative idea of the behaviour of the combiner with increasing numbers of ports. Fig. 3.1 shows this simplified transmission line model for an  $N$ -way combiner, with all lines joined at a single point in space.

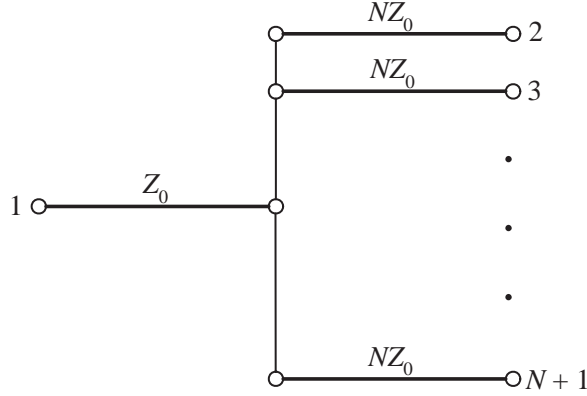


Fig. 3.1. Simplified transmission line model of a reactive  $N$ -way combiner.

Simple network analysis can be used to show that in Fig. 3.1

$$S_{11} = 0 \quad (3.1)$$

and

$$S_{nn} = (1 - N)/N \quad (3.2)$$

with  $n = 2, 3, \dots, N$ . From the lossless property of the combiner, the transmission coefficients can be found from

$$|S_{11}|^2 + N|S_{n1}|^2 = 1 \quad (3.3)$$

as

$$|S_{n1}| = \sqrt{\frac{1}{N}}. \quad (3.4)$$

Now, using the reciprocal and lossless properties of the network, the isolation between any of the peripheral ports can be found from

$$|S_{1n}|^2 + |S_{nn}|^2 + (N - 1)|S_{n'n}|^2 = 1 \quad (3.5)$$

with  $n' = 2, 3, \dots, N$  and  $n' \neq n$  as

$$|S_{n'n}| = \sqrt{\frac{1 - |S_{1n}|^2 - |S_{nn}|^2}{N - 1}} = \frac{1}{N}. \quad (3.6)$$

From (3.6) it is clear that the coupling between different peripheral ports will decrease proportionally to the number of ports, and therefore the isolation will improve. Isolation is achieved in reactive combiners by mismatching of the input ports for the case of unsymmetrical excitation. This can be seen by calculating  $S_{nn}$  in (3.2), which describes the reflected power at port  $n$  when only that port is excited.

### 3.2 Basic Configuration of the Structure

Because the impedance of a conical line is determined by a combination of  $\theta_1$  and  $\theta_2$  (2.116), one of these angles ( $\theta_2$ ) can be chosen in a specific design. Ideally,  $\theta_2$  can be chosen to minimise the cutoff wavelength of higher order modes. The impedance of the line is determined by the number of input ports as the line impedance should be matched to the combination of the parallel  $50 \Omega$  input ports. This characteristic impedance is simply given by

$$Z_0 = \frac{50}{N}, \quad (3.7)$$

where  $N$  is the number of input ports. For 10 input ports the line impedance is set to  $5 \Omega$ . The cutoff frequency of the first three propagating higher order modes in a  $5 \Omega$  line is shown in Fig. 3.2(a) for a fixed distance from the origin. It can be seen in Fig. 3.2(a) that the cutoff

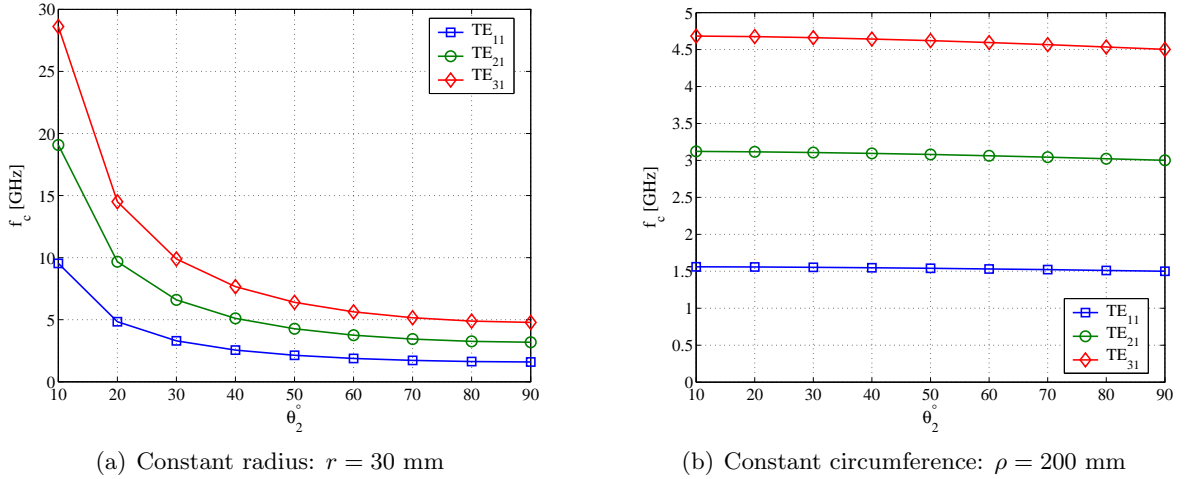


Fig. 3.2. Cutoff frequency of first three higher order modes in a  $5 \Omega$  conical transmission line.

frequency becomes higher for smaller  $\theta_2$ . A smaller  $\theta_2$ , however, presents a smaller circumference at a certain radius. For a power combiner a large circumference is needed to fit multiple ports, therefore a larger radius is needed to obtain the desired circumference for a smaller  $\theta_2$ . In Fig. 3.2(b) the cutoff frequency is again plotted against  $\theta_2$  for a  $5 \Omega$  line, but this time the circumference at the maximum radius is kept constant. It can clearly be seen that the cutoff frequency remains almost constant over all  $\theta_2$ , and therefore any  $\theta_2$  can be chosen to yield the same cutoff frequency for a given circumference.

To investigate the effects of manufacturing tolerances, Fig. 3.3 shows the percentage error in the impedance of the line if  $0.5^\circ$  error is made in  $\theta_1$ . Fig. 3.3 shows that the error in  $Z_0$  is smallest for  $\theta_2 = 90^\circ$  when a small error is made in  $\theta_1$  during manufacturing. Taking the above findings into account, and the fact that a small geometry is sought for the power combiner structure,  $\theta_2$  is chosen as  $\theta_2 = 90^\circ$ , and  $\theta_1$  is computed from (2.116) and (3.7) as  $\theta_1 = 85.23^\circ$ .

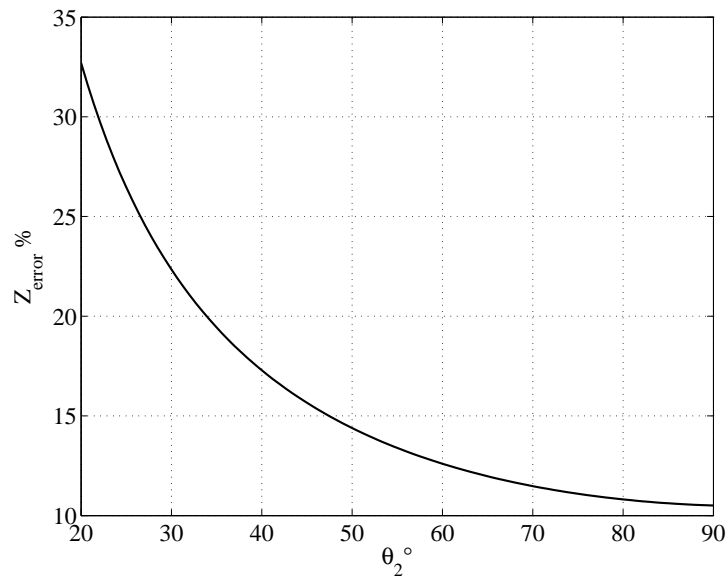


Fig. 3.3. Error in  $Z_0$  as a function of  $\theta_2$  with a  $0.5^\circ$  error in  $\theta_1$ .

Many ways exist for feeding axially symmetric power combiners [1, 2]. When a conical transmission line is used as the combining structure, the obvious choice for the central output port is a coaxial line, because a transition can easily be made from conical line to coaxial line [12]. On the input side, combiners using radial transmission lines can be segmented into several individual microstrip lines [3, 7, 36, 37, 38]. These lines form the input (peripheral) ports of the combiner. This technique is well suited to radial lines because the air gap of the radial line can easily be filled with a dielectric for the microstrip ports. The input ports can also be waveguides coupling into the combining structure at  $N$  equally spaced areas on the periphery of the radial or conical line [13, 39]. Another method for feeding axially symmetric combiners on the input side, which is also suited to a conical line combiner, is to couple magnetically into the conical line with probes extending from coaxial lines. An advantage of this technique is that standard coaxial input connectors can be used on the peripheral ports. This technique has been used in circular cavity combiners [40] and radial wave combiners [4, 6]. A side view of a section of the basic configuration showing the input and output feeds is shown in Fig. 3.4.

A top view showing the relative position and numbers of the different ports is shown in Fig. 3.5.

### 3.3 Central Conical to Coaxial Transition

In order to obtain a good match at the output port, the characteristic impedance of the coaxial feed line has to be the same as that of the conical line in the combining structure. Because of the low impedance level needed ( $5\Omega$ ), the gaps between the conductors must be small compared

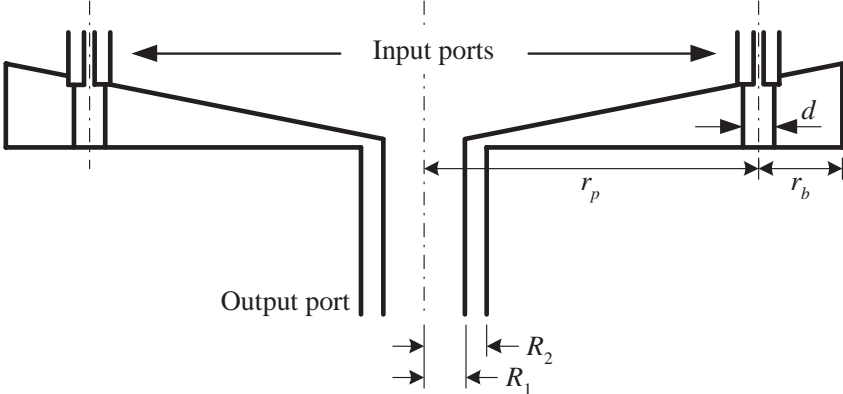


Fig. 3.4. Basic configuration of the power combiner.

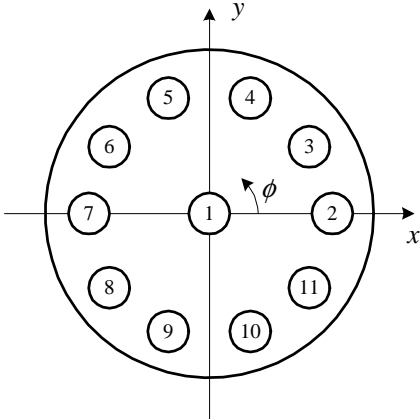


Fig. 3.5. 10-Way combiner port position and numbers.

to their radius at the conical/coaxial junction. The characteristic impedance of an air dielectric coaxial line is given by

$$Z_0 = 60 \ln \left( \frac{R_2}{R_1} \right), \quad (3.8)$$

where  $R_1$  is the radius of the inner conductor and  $R_2$  is the radius of the outer conductor. Because of the small size of the air gap, reflections from a simple junction such as the one shown in Fig. 3.4 will be relatively small. The sharp corner of the simple junction in Fig. 3.4 does, however, present a serious problem in high power combiners. The high field strength near the corner severely limits the power handling capability of the combiner. This field strength can be reduced by rounding these sharp corners, but reflections also increase when the corners are rounded. Van der Walt [12] proposes a smoothly curved, well matched transition between conical and coaxial lines of the same characteristic impedance. This transition is defined by two circles, and the steps for the construction of these circles, as proposed by Van der Walt in [12], are repeated here with reference to Fig. 3.6.

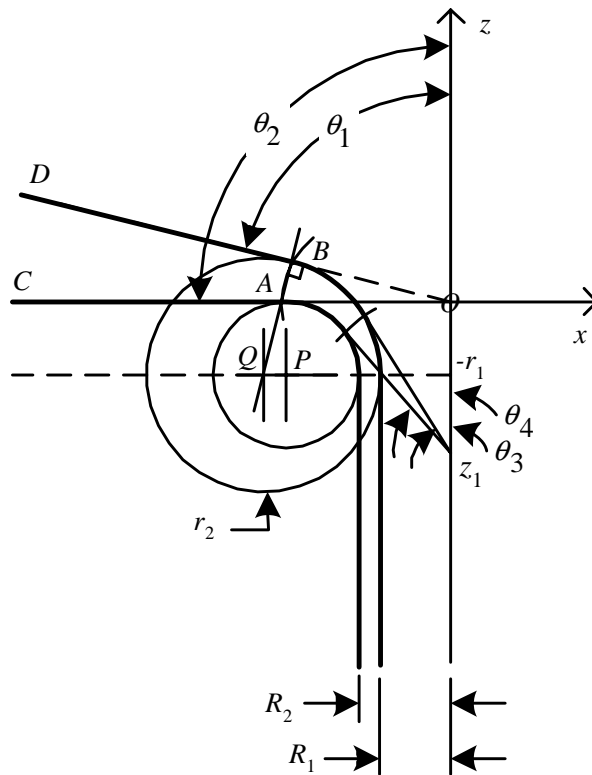


Fig. 3.6. Construction of conical to coaxial transition profile.

1. Choose the outer radius  $R_2$  of the coaxial transmission line and draw the vertical line at  $x = -R_2$ . Choose the apex of the conical line as the origin of the  $x - z$  plane and draw lines  $OD$  and  $OC$  using the previously determined values for  $\theta_1$  and  $\theta_2$ .
2. Decide upon the fillet radius  $r_1$  between the outer and lower conductors of the coaxial

and conical lines. (To limit the curvature of the transition, this radius should be chosen at least three times the gap width,  $R_2 - R_1$ , of the coaxial line - see discussion below.) Construct the fillet by drawing the circle centered at  $P$ , at  $(x, z) = (-R_2 - r_1, -r_1)$ , with radius  $r_1$ . This circle is tangent to the lower surface of the conical line at point  $A$ .

3. Draw the line  $z = -r_1$  perpendicular to the  $z$ -axis, through point  $P$ .
4. Through the tangent point  $A$ , draw an arc centered at the origin  $O$  to intersect the upper surface of the conical line at  $B$ .
5. From  $B$ , draw a line perpendicular to  $OD$  to intersect the line at  $z = -r_1$  at  $Q$ .
6. With  $Q$  as centre, draw a circle tangential to  $OD$ .
7. *It turns out that this circle is also precisely tangential to the inner conductor of the coaxial line at  $x = -R_1$  with characteristic impedance  $Z_{0coax} = Z_{0conical}$ .* (A proof of this property can be found in [12].)

This transition has the property that it defines a conical transmission line of constant characteristic impedance from point to point. This can be shown [12] by first choosing any point  $z_1$  on the  $z$ -axis. From this point, construct a line tangential to the circle centered at  $P$ . With the point  $(x, z) = (0, z_1)$  as centre, construct an arc through the tangent point to intersect the circle centered at  $Q$ . This line also intersects the  $z$ -axis at  $z_1$  and defines a conical transmission line at the tangent points with angles  $\theta_3$  and  $\theta_4$ . It can also be shown that the characteristic impedance of the conical transmission line defined by  $\theta_3$  and  $\theta_4$  has a constant characteristic impedance  $Z_0 = Z_{0conical}$ , regardless of where  $z_1$  is chosen on the  $z$ -axis. (A proof of this property can be found in [12].) To find the field strength in the transition, Wheeler's data for E-plane bends, as reproduced in [41], can be used. For a rectangular waveguide with an average bending radius of 3.5 times the height of the waveguide, an approximate increase of 16% will be observed in the field strength. A similar result can be expected in a curved conical transmission line compared to a straight conical transmission line.

A CST-MWS simulation was done to determine the reflections from and the field strengths within a simple junction and the above curved junction. As the software does not allow for a port on the outer circumference of the conical line, this end of the line was short circuited, and time gating applied to the total reflection from the common port to eliminate the component caused by the short circuit. A plot showing the reflection of only the transition over a wide band for both transitions is shown in Fig. 3.7. The small reflections caused by a simple transition can clearly be seen over a wide band in Fig. 3.7, as well as the improvement obtained by a smoothly curved, well matched transition. The electric field strength was calculated from the CST-MWS results along a curve running through the middle of the air gap of each of the transitions

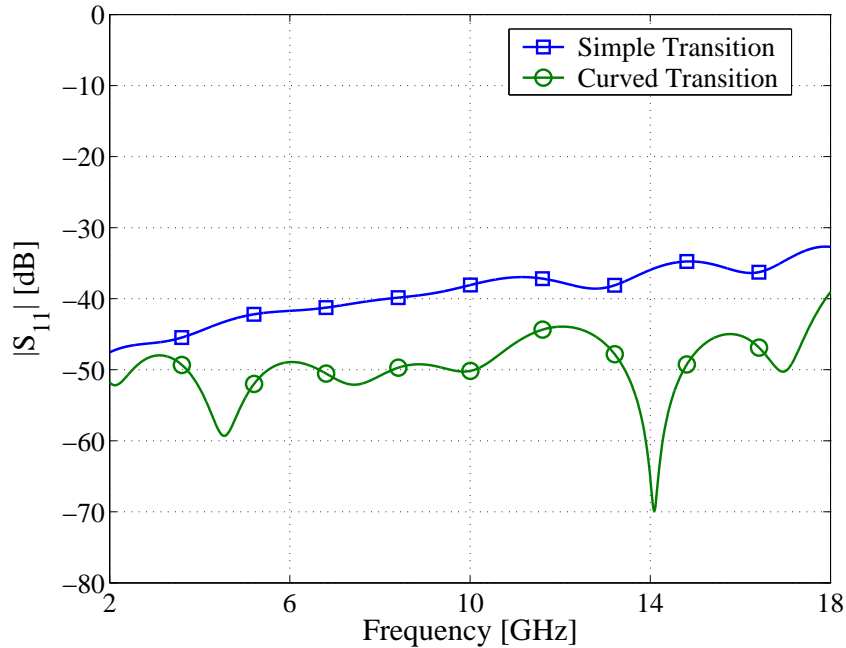


Fig. 3.7. Reflection from conical/coaxial transitions.

described above, with the same input power applied to both models (1 W). The results plotted in Fig. 3.8 can be used to show that the rounded corner does indeed reduce the field strength in the transition. The results in Fig. 3.8 should, however, not be used in a quantitative sense, but rather in a comparative sense due to uncertainty in the numerical results in the vicinity of sharp corners common to numerical EM techniques.

### 3.4 Peripheral Input Port Feeds

Different methods exist for analysing and designing coaxial probe feeds on the periphery of a radial line. Bialkowski and Waris [5] derived a full electromagnetic model for the structure with probes using a field matching technique. Optimisation of the feed probes using this method produced good results (return loss better than -17 dB in the 10-18 GHz band) in a radial line, but would be very tedious to repeat for a conical line. Another disadvantage of this method is that the complicated electromagnetic field computation makes physical interpretation of the results very difficult, and therefore gives very little design guidelines. Nogi *et al.* [6] presented an equivalent circuit for the peripheral part of a radial power combiner. The circuit parameters are obtained by using a Method of Moments (MoM) solution [42] for a probe in a semi-infinite parallel plate waveguide of width equal to the spacing between the neighbouring coaxial probes. Clearly this would be a very crude approximation to use in a conical line because of the parallel plate approximation, which would not hold in a conical line. Another way to analyse the structure would be full wave simulations in CST-MWS or a similar full wave solver. This also

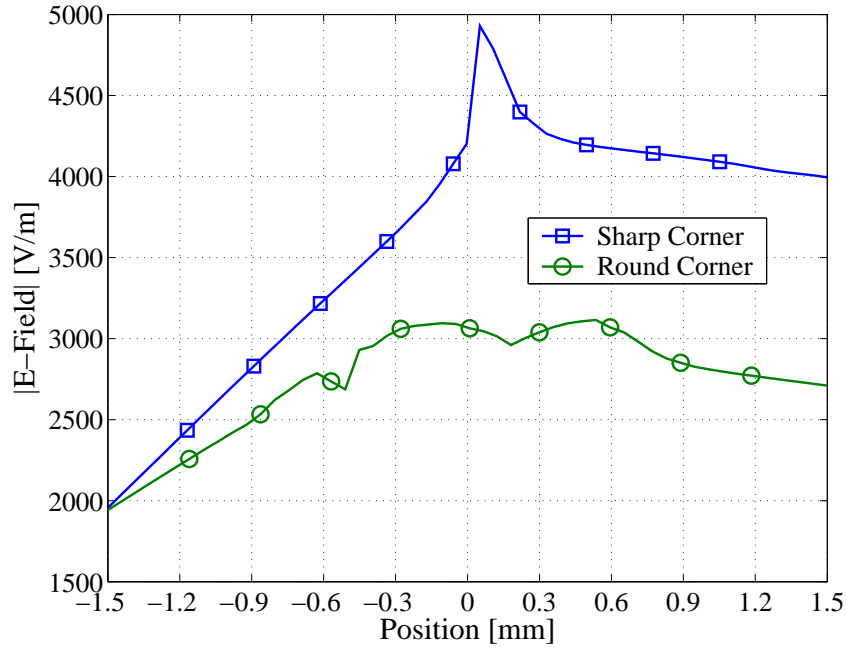


Fig. 3.8. Electric field size in the conical/coaxial transitions at 10 GHz with an input power of 1 W and  $R_1 = 3.22$  mm and  $R_2 = 3.5$  mm.

has the disadvantage of being time-intensive, with little physical insight into the problem being gained. Also, when optimising the feed probes using the above field computation techniques, the results often produce probe dimensions which are difficult to manufacture.

The difficulty in all these designs is the achievement of a good match in a difficult electromagnetic environment. Here, a solution is proposed with a very simple probe feed into the conical line, matched on the outside in a simple coaxial environment. Such matching networks can easily be optimised using analytical models in a circuit simulator such as Applied Wave Research's Microwave Office (MWO). The method would be to obtain the  $S$ -parameter description of the power combiner with the feeding probes, importing this model into MWO, and placing transmission lines at the ports and optimising the length and impedance of these lines to obtain the best wideband match.

Using this simple feed topology, the only design parameters are the radial position of the probe,  $r_p$ , the radial distance to the short circuit from the probe,  $r_b$ , and the diameter of the probe,  $d$ , as shown in Fig. 3.4. In the case of electrically coupled probes, the length of the probes can also be treated as a design parameter, but for the case of a high-power structure, magnetically coupled probes extending the full height of the guide at the feed point are used [6]. This is due to the very strong E-fields that would be present between the base of the conical line and the base of the probes if the E-field probes were to be used.

The value for  $r_p$  should be chosen as low as possible to restrict higher order modes (see Fig. 2.8).

The minimum value is determined by the dimensions of the connectors to be used in order to fit the required number of connectors on the circumference – in this case a value of  $r_p = 25$  mm is found.

Collin [43] computed the input impedance of a probe feeding a rectangular waveguide showing that a wider probe (larger  $d$ ) gives a wider matched bandwidth. Although the results cannot be used quantitatively for the case of a conical transmission line, a good qualitative idea can be formed of the behaviour of a probe fed conical line by comparing it to a probe fed rectangular waveguide. Extendable tuning posts are used as probes, as these can easily be fastened to the bottom plate of the conical line, and extended into the cavity from the bottom plate until good electrical contact is made with the coaxial line entering from the top of the conical line. The widest commercially available post which is narrower than the outer conductor of the Sub-Miniature A (SMA) feed (4.06 mm), has a diameter of 3.2 mm.

The short circuit at the end of the conical line should be transformed to an open circuit by the length of transmission line  $r_b$  at the centre frequency. The centre frequency of the match can be shifted by changing this length. Starting with the value  $r_b = 7.5$  mm (quarter wavelength at 10 GHz), only a few quick CST-MWS simulations are needed to find that  $r_b = 7.6$  mm produces the desired centre frequency for the match at 10 GHz.

A CST-MWS screen shot of the model used for these simulations is shown in Fig. 3.9. Since only the TEM mode is considered in the design, magnetic walls can be inserted on the  $x$ - $z$  and  $y$ - $z$  planes because the tangential magnetic field is zero for the TEM mode on these planes. Only a quarter of the structure needs therefore be analysed. The input ports are standard SMA connectors with feeding probes designed as described above. The output port is a  $5\ \Omega$  coaxial line feeding into the transition of Section 3.3. The effects of the lines between the ports and the actual conical combining structure are removed by de-embedding the length of the lines from the results. The CST-MWS result for the reflection coefficient looking into the output port is shown in Fig. 3.10.

Fig 3.10 clearly shows the centre frequency of the common port reflection coefficient is at the desired 10 GHz.

### 3.5 Input and Output Matching Networks

By exporting the full  $S$ -parameter matrix of the CST-MWS simulation and normalising it to a  $5\ \Omega$  environment, the matching networks in the input and output feed lines can be designed by optimisation of the circuit model in Fig. 3.11.

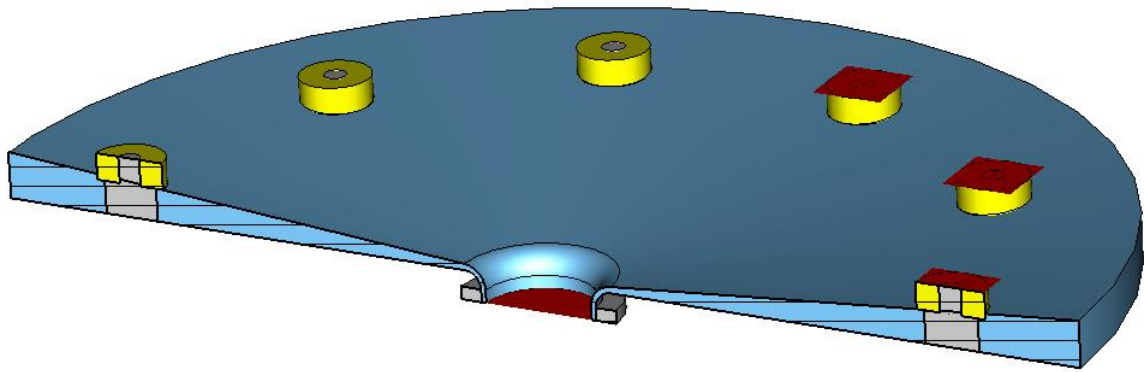


Fig. 3.9. CST-MWS screen shot of 10-way power combiner showing central conical to coaxial transition and peripheral feeding probes. The background material as well as the grey parts are perfect electrical conductors (PEC), the blue part is vacuum, and the yellow parts are tefflon. Ports are represented by red rectangles.

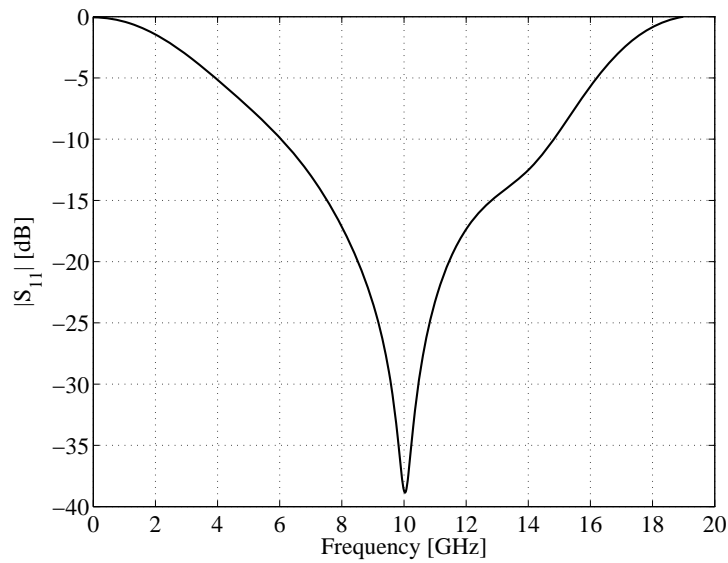


Fig. 3.10. CST-MWS simulation of 10-way power combiner common central port reflection coefficient.

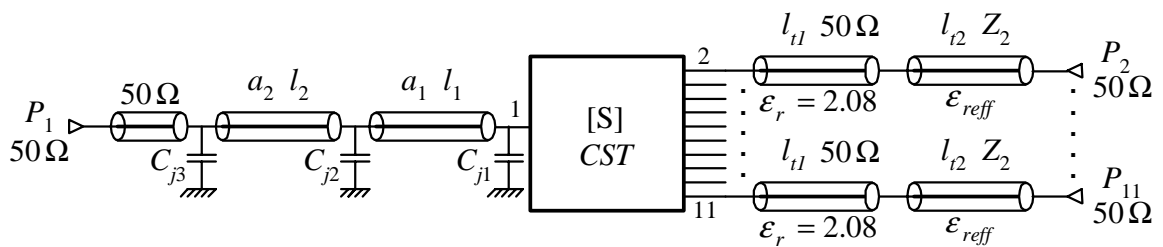


Fig. 3.11. Schematic representation of circuit to be optimised in MWO.

### 3.5.1 Input Matching Section

The input matching section consists of two coaxial transmission lines on all ten input ports. The two transmission lines are constructed by an extended dielectric SMA connector inserted into a hole in the metal at the top of the conical line. The impedance of the first section is the normal  $50\ \Omega$  of the SMA connector, and the impedance and effective permittivity of the second line is obtained by cutting away a thin layer of dielectric from the connector. A sketch of such a connector forming two transmission lines is shown in Fig. 3.12.

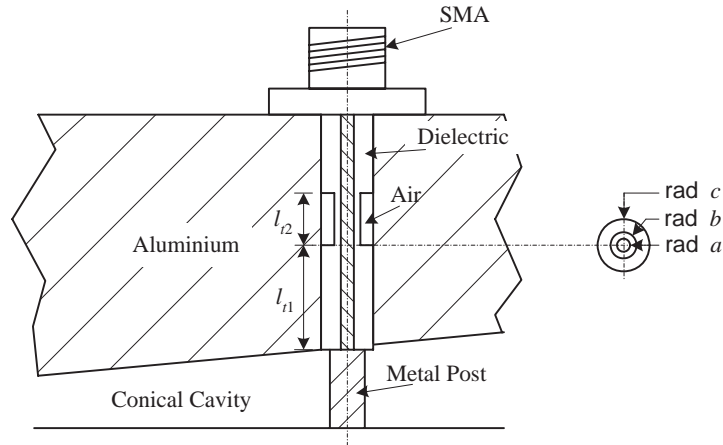


Fig. 3.12. Sketch of an extended dielectric SMA connector inserted into the top of the metal structure to form two short transmission lines.

The effective permittivity of a partially filled coaxial transmission line such as the one described above, can be obtained by solving the static capacitance of the line and comparing it to the static capacitance of a normal coaxial line filled with dielectric. The potential distribution in a partially filled coaxial line is found by solving Laplace's equation in cylindrical coordinates and applying the proper boundary conditions. This is straightforward, and the potential is given by [9] as

$$\Phi_1 = \frac{V_0 \ln(r/a)}{\ln(b/a) + \epsilon_r \ln(c/b)} \quad a < r < b \quad (3.9)$$

$$\Phi_2 = V_0 \left[ 1 - \frac{\epsilon_r \ln(c/r)}{\ln(b/a) + \epsilon_r \ln(c/b)} \right] \quad b < r < c. \quad (3.10)$$

The capacitance follows from integrating the surface charge density per unit length over the inner electrode to find

$$\sigma_1 = \oint_{S_1} \epsilon_0 \mathbf{E}_1 \cdot d\mathbf{a} = \int_0^{2\pi} \int_0^1 -\nabla \Phi_1 dz d\phi = \frac{-2\pi\epsilon_0 V_0}{\ln(b/a) + \epsilon_r \ln(c/b)}, \quad (3.11)$$

with the capacitance given by

$$C = -\frac{\sigma_1}{V_0} = \frac{2\pi\epsilon_0}{\ln(b/a) + \epsilon_r \ln(c/b)}. \quad (3.12)$$

This can be rewritten in a form resembling the capacitance of a normal coaxial line given by [44]

$$C_{coax} = \frac{2\pi\epsilon_0\epsilon_r}{\ln(c/a)}, \quad (3.13)$$

as

$$C = \frac{2\pi\epsilon_0}{\ln(c/a)} \frac{\epsilon_r \ln(c/a)}{\ln(b/a) + \epsilon_r \ln(c/b)}. \quad (3.14)$$

The effective permittivity can be found from (3.13) and (3.14) as

$$\epsilon_{reff} = \frac{\epsilon_r \ln(c/a)}{\ln(b/a) + \epsilon_r \ln(c/b)}, \quad (3.15)$$

with the characteristic impedance following as

$$Z_2 = \frac{60}{\sqrt{\epsilon_{reff}}} \ln(c/a). \quad (3.16)$$

The parameters used for the optimisation of the input transmission line matching section are the radius of the dielectric in the second line,  $b$ , thus changing the impedance of the line  $Z_2$ , and the lengths of the two lines,  $\ell_{t1}$  and  $\ell_{t2}$ . The total length of the connector should, however, be restricted to 15 mm because of the available connector sizes.

### 3.5.2 Output Matching Section

The output matching section consists of a stepped impedance air dielectric coaxial transmission line to match the  $5\Omega$  conical line to a  $50\Omega$  N-Type coaxial connector. The impedance is changed by stepping the radius of the inner conductor, and keeping the radius of the outer conductor constant. A sketch of the stepped coaxial line is shown in Fig. 3.13.

The radius of the outer conductor is determined by the connector to be used at the feed point (7 mm for a precision N-Type connector). The length ( $\ell_{1,2}$ ) and inner conductor radius ( $a_{1,2}$ ) of each section of line are used as parameters in the circuit model optimisation. The effect of the steps in the coaxial line is modelled by small static capacitances at the junctions  $C_{j1,2,3}$  [45]. This capacitance is given by

$$C_j = \frac{\epsilon_0}{100\pi} \left[ \frac{\alpha^2 + 1}{\alpha} \ln \frac{1 + \alpha}{1 - \alpha} - 2 \ln \frac{4\alpha}{1 - \alpha^2} \right] + 1.11 \times 10^{-15} (1 - \alpha)(\tau - 1) \quad \text{F/cm} \quad (3.17)$$

where

$$\alpha = \frac{r_3 - r_2}{r_3 - r_1} \quad (3.18)$$

and

$$\tau = \frac{r_3}{r_1}, \quad (3.19)$$

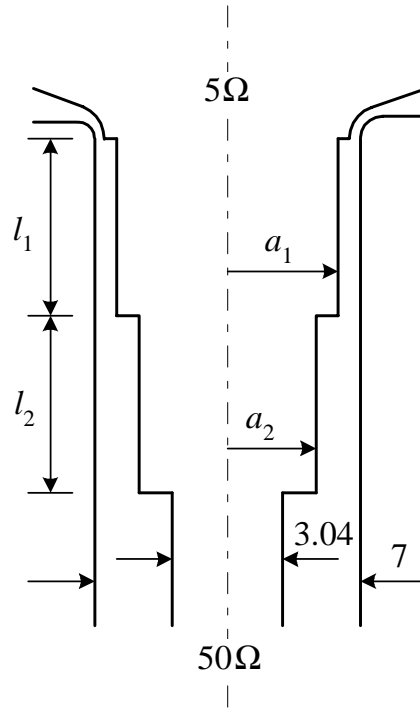


Fig. 3.13. Stepped impedance coaxial line feeding the conical line.

with  $r_3$  the radius of the outer conductor,  $r_2$  the radius of the larger inner conductor in the step, and  $r_1$  the radius of the smaller inner conductor in the step. The capacitance is obtained by multiplying (3.17) by the circumference of the outer conductor in cm.

The optimisation routine in MWO was set up with the goal that  $S_{11}$  should be as low as possible in the band 8-12 GHz. The final values obtained for the parameters are  $l_1 = 7.22$  mm,  $l_2 = 7.34$  mm,  $a_1 = 2.93$  mm,  $a_2 = 2.10$  mm,  $l_{t1} = 5.37$  mm,  $l_{t2} = 2.67$  mm and  $b = 1.55$  mm. The MWO and CST-MWS reflection results for this structure are plotted in Fig. 3.14.

The shift in frequency of the response in the pass band in the CST-MWS simulation was found to be due to a very high sensitivity to the dimension  $a_1$ . Very small changes in  $a_1$  (as small as  $10\ \mu\text{m}$ ) cause significant changes in the pass band response. This effect must be carefully considered during construction of the structure. By designing the matching networks to give  $S_{11} < -25$  dB in MWO, a 5 dB margin is left to account for manufacturing tolerances in order to still obtain a 20 dB match.

Note that only optimisation of the *circuit* model is necessary in this design approach, and no optimisation of the full wave simulation model.

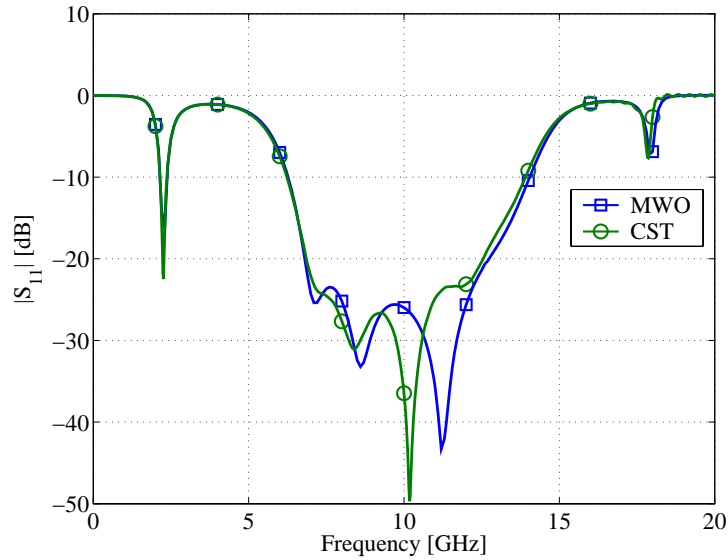


Fig. 3.14. Simulated reflection coefficient of matched 10-way conical power combiner.

### 3.6 Summary of the Step-by-Step Design Procedure

The full design process can be summarised as follows.

1. The combining structure is designed and the exact response of the structure is determined with a full-wave solver.
  - (a) Determine the impedance of the conical line from the number of ports as  $Z_0 = 50/N$ .
  - (b) Construct the central transition between conical and coaxial line as described in [12], using  $\theta_2 = 90^\circ$  and calculating  $\theta_1$  from (2.116).
  - (c) Determine the radius  $r_p$  where the input ports are placed, based on the width of the connectors, the spacing between the connectors, and the number of connectors used. Keep  $r_p$  as small as possible to reduce higher order modes (See Chapter 5).
  - (d) Determine the diameter of the feeding probes. Wider probes give better bandwidth, but the diameter is limited by the outer diameter of the input feeding coaxial lines.
  - (e) Determine the length of the backshort  $r_b$  using a full-wave solver parameter sweep. Note that this becomes more difficult for larger structures – see Chapter 5.
  - (f) Analyse the entire structure with a field solver to get the  $S$ -parameters at all the ports.
2. Optimise stepped impedance transmission lines on the input and output side of the combining structure in a circuit simulator to achieve a wide matched bandwidth.

### 3.7 Construction and Measurement

Due to the high degree of accuracy required in the manufacturing of the structure, a CNC-lathe is used for the construction. The sharp corner of the conical line short circuit had to be replaced by a rounded corner for manufacturing purposes as shown in Fig. 3.15.

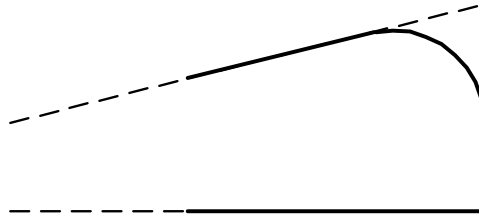


Fig. 3.15. Rounded corner detail of the conical line.

A CST-MWS simulation was done with a 1.25 mm corner fillet radius, and the results achieved for the reflection coefficient can be seen from Fig. 3.16 to be better than those achieved with a sharp corner.

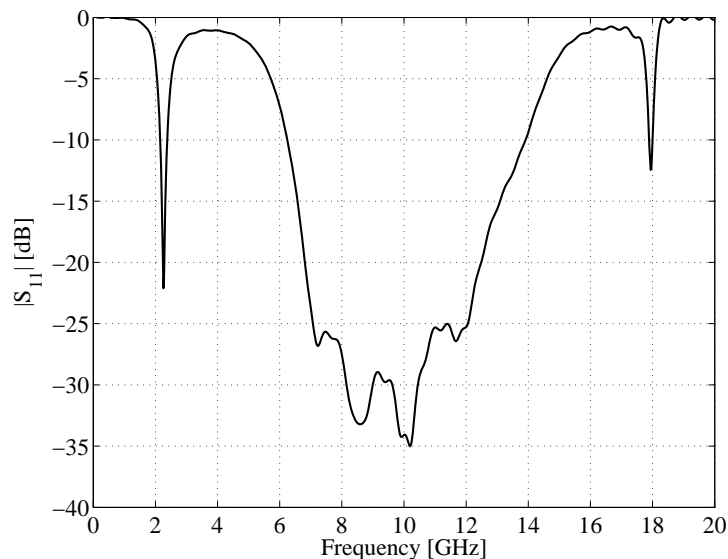


Fig. 3.16. CST-MWS simulation reflection coefficient of matched 10-way combiner with rounded corner.

The structure is divided into two parts (top and bottom), which are cut from aluminium blocks and screw fastened to each other. The top part forms the coaxial centre conductor of the central coaxial output port and the top part of the conical line. The bottom part forms the outer conductor of the central coaxial output port and the bottom part of the conical line. Extended dielectric SMA connectors prepared as in Fig. 3.12, which are inserted into holes in the top part of the structure, form the radial input ports. Tuning posts inserted into and extended from the bottom part of the structure are used as the feeding probes. The central output port is

formed into a female N-Type connector, with the centre pin of a commercially available N-Type connector epoxy fastened in a hole in the inner conductor of the central output coaxial line. A 2-D section view of the entire structure with all the connectors, tuning posts and fastening screws included is shown in Fig. 3.17. Some photographs of the structure are also shown in Fig. 3.18.

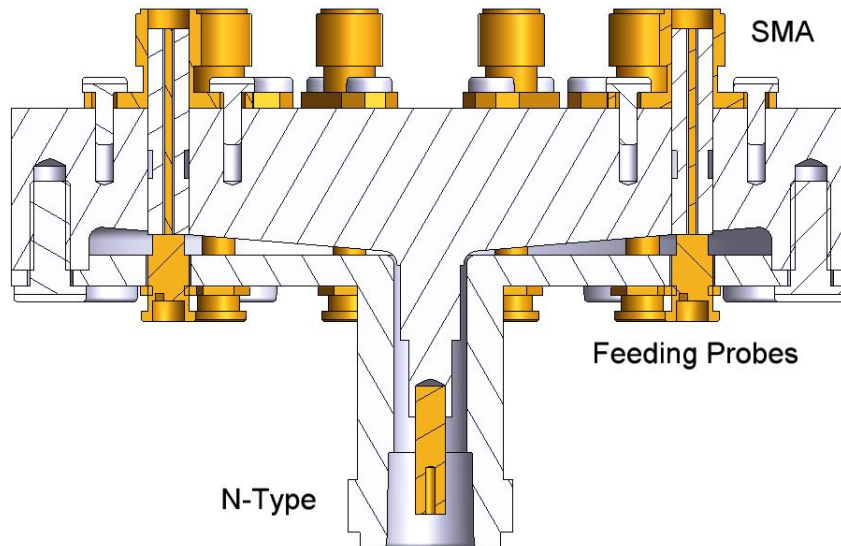


Fig. 3.17. 2-D section view of the conical combiner showing all connectors, feeding probes and fastening screws.

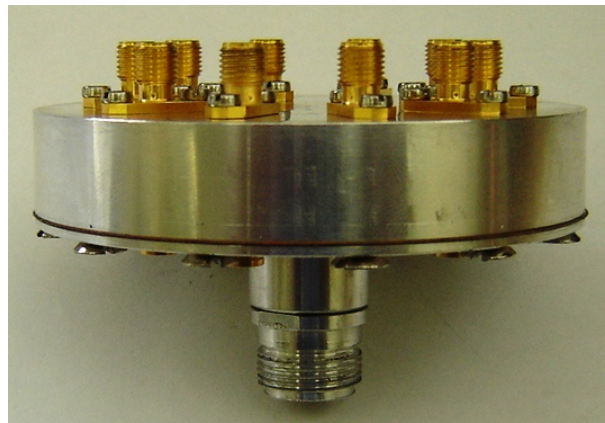
Two-port measurements were done on the *Agilent 8510C* Vector Network Analyser (VNA) using precision SMA loads to terminate the ports that are not being measured.

The simulated and measured reflection results of the common port of the constructed combiner are shown in Fig. 3.19. A matched bandwidth of 74% is achieved with a maximum return loss of -14.7 dB, from 6.5 to 14.1 GHz. The difference between the simulated and measured results at low values of  $|S_{11}|$  is caused in part by the difficulty in simulating and manufacturing accurately a large structure with very narrow gaps. The gap in the central coaxial to conical transition is only 0.28 mm compared to the diameter of the structure, which is 65.2 mm.

The measured transmission characteristics of the combiner are shown in Fig. 3.20. The simulated transmission coefficients are not shown since the simulated structure is perfectly symmetrical. As expected from (3.4) the amplitudes of the transmission coefficients are around -10 dB. A maximum amplitude imbalance of  $\pm 1$  dB and a phase imbalance of  $\pm 5^\circ$  are observed in the 8–12 GHz band, and an amplitude imbalance of  $\pm 1.5$  dB and a phase imbalance of  $\pm 10^\circ$  are observed in the 6–14 GHz band. At the peripheral ports a small gap (0.43 mm) is formed



(a) Separated top and bottom parts



(b) Fully assembled

Fig. 3.18. Photographs of the constructed 10-way combiner.

between the input probes of diameter 3.2 mm, and the feeding lines with outer diameter of 4.06 mm. Any misalignment between the top and the bottom parts of the structure will reduce this gap, and may cause imbalances in the transmission coefficients to the different ports. These problems will be addressed in following designs.

The simulated and measured isolation characteristics of the combiner are shown in Fig. 3.21, where good agreement between the results is demonstrated. It is noted that the worst isolation occurs between port 2 and port 7 (the ports located at the opposite sides of the combiner), which is consistent with the remarks made in [5]. As reported in [5], these values are consistent with reactive radial combiners. No attempt was made to improve the isolation of the combiner, but it is known from (3.6) that the isolation will improve when the number of ports are increased (see also the comments in [6]). The isolation characteristics are further discussed in Section 3.8.

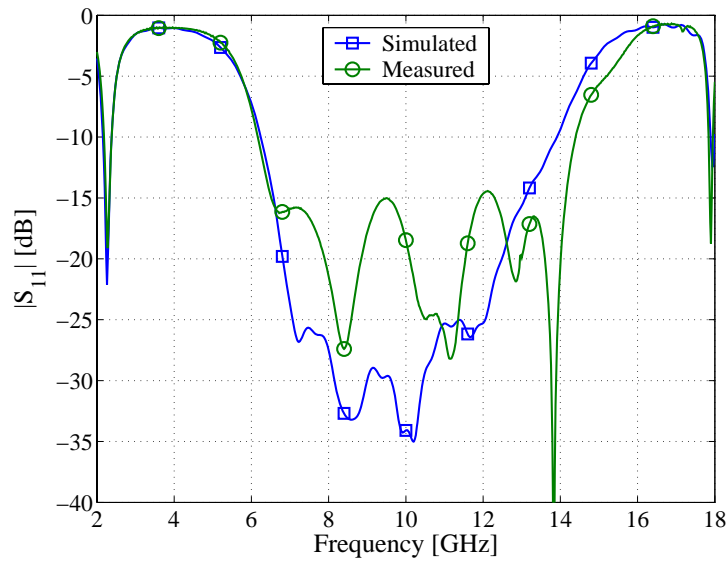


Fig. 3.19. Comparison between the simulated and measured reflection coefficient of a 10-way combiner.

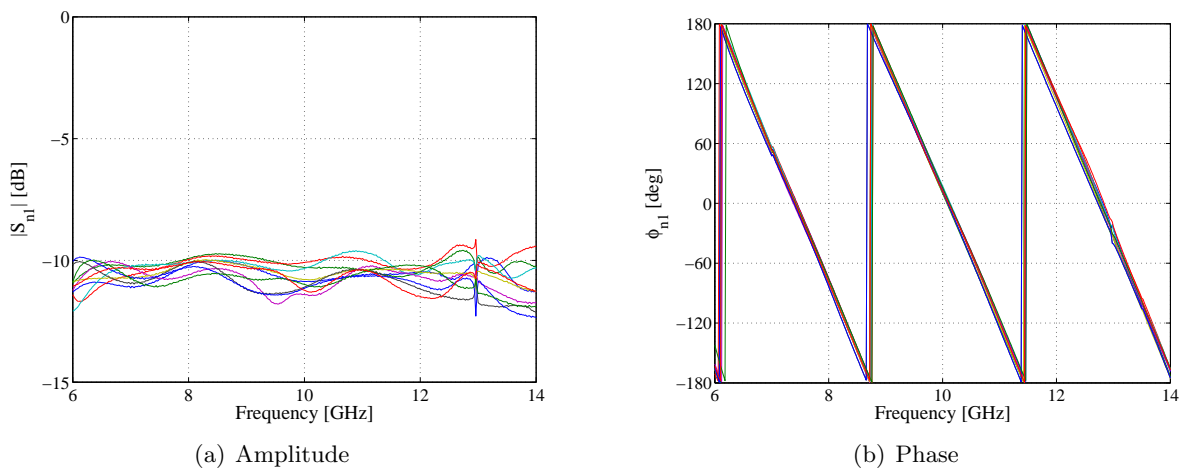


Fig. 3.20. Measured transmission coefficients in the operating band of a 10-way combiner ( $S_{n1}$  with  $n = 2, 3, \dots, 11$ ).

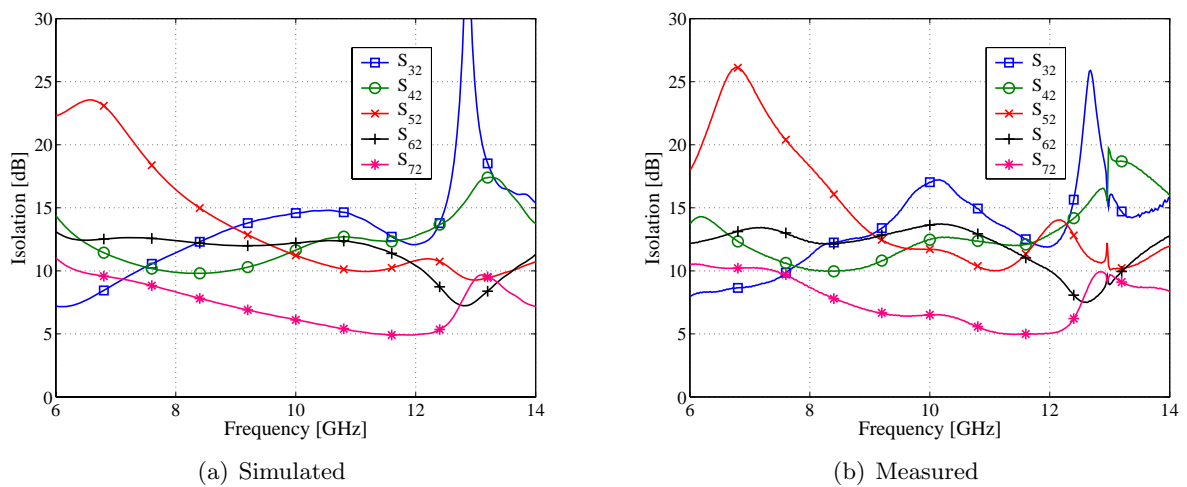


Fig. 3.21. Simulated and measured isolation in the operating band of a 10-way combiner.

Fig. 3.22 shows the total  $I^2R$  loss characteristic of the combiner. The maximum loss in the operating band is 1.1 dB, and the average loss only 0.45 dB. The loss includes the effects of the SMA transitions as well as a SMA to N-Type transition used in the measurement setup. This low loss is one of the advantages of radial type combiners over corporate or chain-type combiners for a large number of ports ( $N > 8$ ). The simulated loss is not included since the simulated structure is completely lossless.

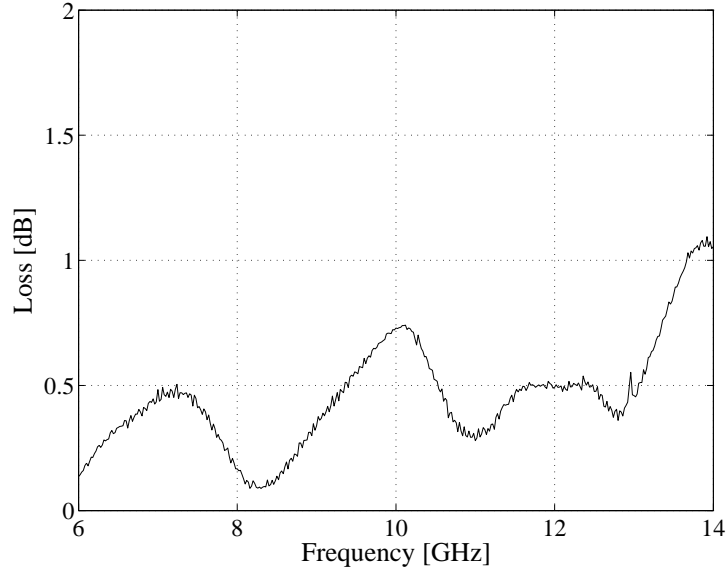


Fig. 3.22. Measured loss of a 10-way combiner.

Some radial combiners reported in the literature include 30-way combiners built at 12.5 GHz demonstrating a 25% bandwidth with a return loss of around -13 dB [7, 3]; a 20-way combiner built at 14 GHz demonstrating a 57% bandwidth with a -17 dB return loss [5]; and 8- and 16-way combiners built at 10 GHz demonstrating -20 dB return loss bandwidths of respectively 33% and 25% [6]. Also, coaxial combiners have been built at  $X$ -band demonstrating a 15% bandwidth [2, 11], and at  $Ku$ -band an eight-diode conical combiner was constructed using GaAs IMPATT diodes to generate 17.9 W of output power at 14.6 GHz [13]. Clearly, the 74 % bandwidth match with a -14.7 dB return loss obtained in the design presented in this chapter is much superior to the results previously published for similar types of combiners.

### 3.8 Isolation

From equation (3.6) the ideal isolation in a symmetrical 10-way combiner is 20 dB, which, as can be seen in Fig. 3.21, is clearly not obtained in a reactive conical combiner. Due to physical separation between the ports, the isolation obtained in this combiner, as in other practical combiners of this type, varies significantly with frequency, and is also much lower than the

predicted 20 dB for the ideal case. This behaviour is due to the existence of higher order modes in the conical line structure when it is driven unsymmetrically. For the ideal case, TEM operation was assumed in all the transmission lines, and as can be seen in the zero-time simulated H-field pattern at 10 GHz plotted in Fig. 3.23, this is clearly not the case here.

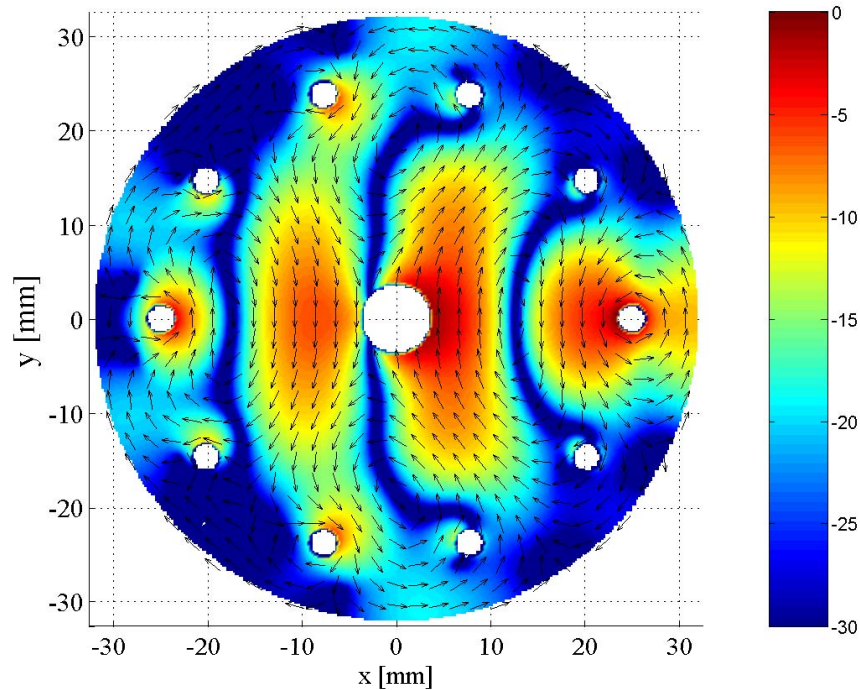


Fig. 3.23. Normalised absolute value (in dB) and direction of the simulated H-field at zero-time in a 10-way conical combiner at 10 GHz when port 2 (see Fig. 3.5) is driven and the other ports are terminated.

The H-field pattern in Fig. 3.23 can be compared to the H-field pattern of the  $TE_{21}$  mode shown in Fig. 2.14, which, from (2.140), propagates in the region where  $r > 9.7$  mm at 10 GHz. Although the mode pattern in Fig. 3.23 is somewhat distorted due to the presence of the input probes and the unsymmetrical excitation, it still resembles the mode pattern of the ideal  $TE_{21}$  mode due to the 4 groups of closed H-field loops visible in the field pattern.

From the field pattern in Fig. 3.23, and the time averaged H-field strength shown in Fig. 3.24, it can be deduced that the strongest coupling from port 2 would be to port 7 (opposite ports). The H-field in the vicinity of port 7, when compared to the H-field in the vicinity of the other ports, most closely resembles the H-field of the normal TEM mode in a coaxial line, and also has the highest average value. This observation is in agreement with the predicted and measured isolation in Fig. 3.21. More is said of the isolation in conical line combiners in Sections 4.6 and 5.5.

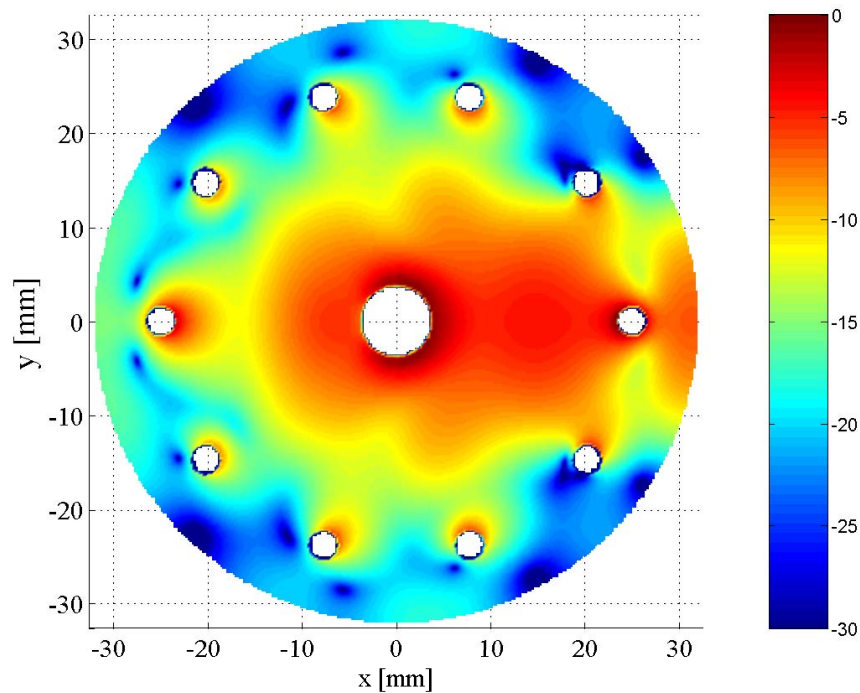


Fig. 3.24. Normalised absolute value (in dB) of the time averaged simulated H-field in a 10-way conical combiner at 10 GHz when port 2 (see Fig. 3.5) is driven and the other ports are terminated.

### 3.9 Electric Field Strength and Peak Power Considerations

The peak power handling capacity of transmission lines is usually limited by breakdown due to ionization of the gas that fills the guide. Breakdown in air at sea level occurs at an electric field strength of around 2.9 MV/m. It is well known that electric field strength increases considerably in the vicinity of sharp corners in the structure, therefore the steps in the central coaxial feed line will be the main limiting factor of the power handling capability of the combiner (Lower power levels exist at the radial input ports).

It is very difficult to predict exactly what the field strength will be near the sharp edges in the coaxial line. Weber's data [46] for a rounded  $90^\circ$  corner near an electric wall can be used if the corner is slightly rounded. The exact shape of the corner is a function of the machining tools used to cut the material, and is therefore hard to predict accurately. Also, standing wave effects must be included in the analysis, and these are tedious to predict accurately analytically. Instead, a full wave CST-MWS simulation of the structure is done to obtain an idea of the field strengths in the structure. It must be stressed, however, that due to the inherent difficulty common to numerical EM techniques in solving fields in the vicinity of sharp corners, the results presented here should be used more in a comparative than a quantitative sense (see Section 4.7 for comparative results). Fig. 3.25 shows the normalised magnitude of the TEM E-field in a

10-way combiner when a 2-D section view is taken of the structure.

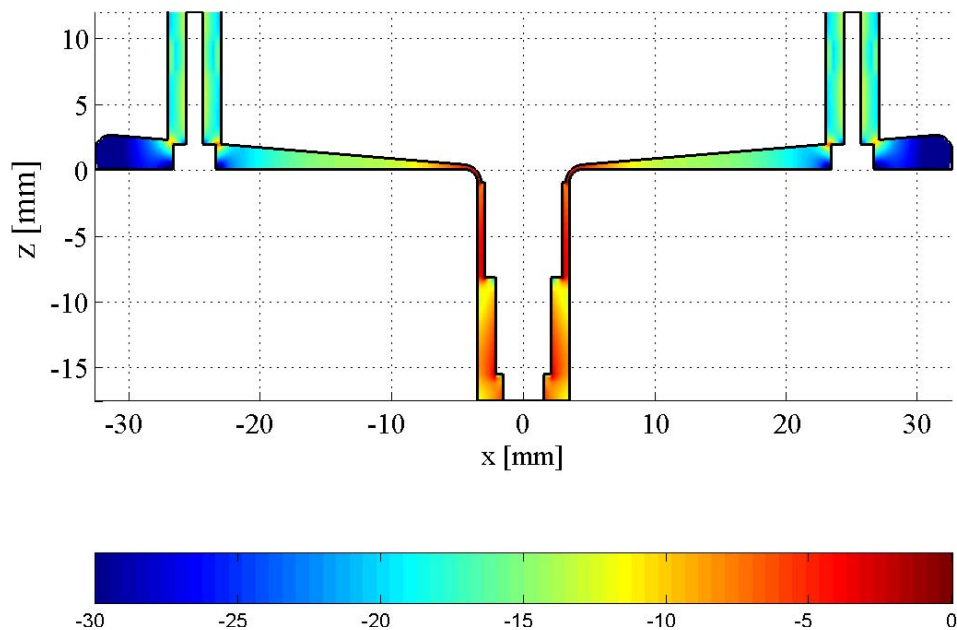


Fig. 3.25. 2-D section view of the normalised magnitude (in dB relative to 12.3 kV/m) of the TEM E-field in a 10-way combiner at 10 GHz with 1 W of input power.

As expected, the strongest fields in Fig. 3.25 exist near the sharp corners in the stepped impedance central coaxial line. This can be seen more clearly when the field is evaluated on the surface of the inner conductor of the central line from the central output port to one of the peripheral input ports. The field strength along such a curve is given in Fig. 3.26.

The plot in Fig. 3.26 clearly shows the very high field strengths near the sharp convex corners in the structure, and also the very low strengths in the vicinity of the nearby concave corners. The field strength is also seen to decrease closer to the peripheral ports, except for the large field caused by the sharp corner of the peripheral probe. This field strength is, however, much lower than that observed in the central high power part of the combiner.

The sharp corners in the stepped impedance central coaxial line are thus seen to cause large increases in electric field strength in the structure, and therefore severely limit the peak power handling capability of the combiner. This problem is addressed in the following chapter, and some comparative results are shown in Section 4.7.

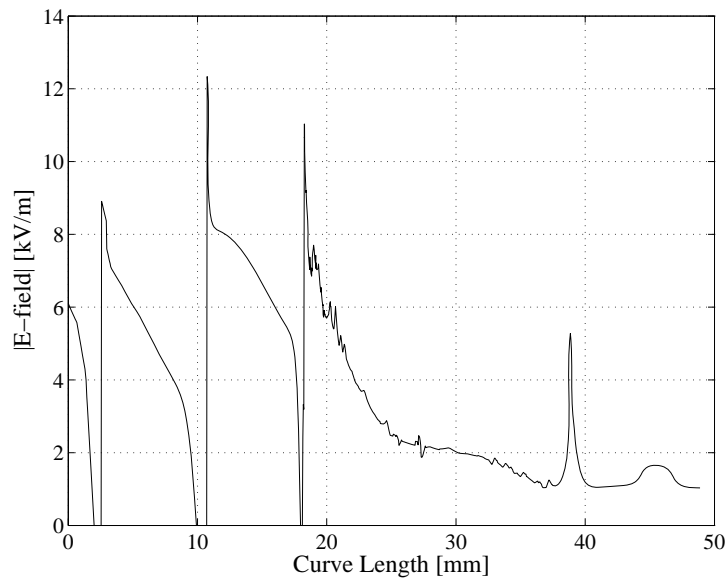


Fig. 3.26. Magnitude of the TEM E-field along a curve on the surface of the inner conductor of the central line from the central output port to one of the peripheral input ports of a 10-way stepped impedance combiner at 10 GHz with 1 W of input power.

### 3.10 Conclusion

In this chapter a conical line power combiner is proposed, and a simple design technique is presented. The technique is general and may be applied to the design of similar  $N$ -way conical line combiners.

Because of the uniform TEM transmission line properties of conical transmission lines, the design technique calls for very little full-wave model optimisation, but instead relies on optimisation of simple analytic transmission line models to achieve a wide operating bandwidth. This is in contrast to the design of radial line combiners, which do not support a uniform TEM transmission mode, where full-wave optimisation of the entire structure is normally necessary to obtain wide band operation.

A 10-way conical combiner was constructed and demonstrated excellent wide band performance as well as low losses. The structure is very compact and lightweight, and is therefore ideally suited for space and airborne applications.

## Chapter 4

# Design of a 10-Way Tapered Line Combiner

One of the main advantages of conical lines over radial lines is, as stated before, the existence of a uniform TEM transmission line mode and therefore a constant transmission line impedance with radial distance. This property allows the designer to make use of a huge array of uniform transmission line design techniques – in this case transmission line tapers.

The design in Chapter 3, although showing excellent performance, requires very tight manufacturing tolerances due to the narrow gaps in the structure – specifically the gap in the central coaxial to conical transition (0.28 mm), and the gaps between the peripheral feeding probes and the outer conductors of the feeding coaxial lines (0.43 mm). Errors of 0.1 mm in the construction of the central transition could cause impedance variations of as much as 36 %. This can significantly influence the reflection performance of the combiner, as can be seen in the measured results in Fig. 3.19. Minor construction errors at the peripheral probes will cause imbalance at the peripheral ports, as can be seen in the measured results in Fig. 3.20.

To increase the gap between the conductors of a coaxial transmission line without changing the diameter of the outer conductor, it can be seen from (3.8) that the impedance of the line must be increased. In this chapter it is shown how a tapered transmission line matching network can be employed in the uniform conical transmission line to increase the impedance level at the central conical to coaxial transition, and thus enlarge the conductor spacing. The central output coaxial line matching network will also be of the tapered line type to eliminate all the sharp edges in the high power central part of the combiner, and thus increase the power handling capability of the structure.

## 4.1 Peripheral Input Port Feeds and Matching

To increase the size of the gaps between the probes in the conical line and the outer conductors of the coaxial lines feeding the probes, the impedance of the peripheral input port feeds must be increased. A matching network must also be designed to match the higher impedance feeding lines to the  $50\ \Omega$  SMA connectors. When the impedance of the feeds is increased, the impedance of the conical line in the combining structure must also be increased accordingly. This is advantageous since, as stated earlier, a higher impedance is sought for the conical line to enlarge the conductor spacing.

A simple way to construct a high impedance coaxial feed line, matched to a  $50\ \Omega$  connector, would be to use a quarter wavelength partially filled coaxial line to match the high impedance air coaxial line to the connector. A sketch of the configuration is shown in Fig. 4.1.

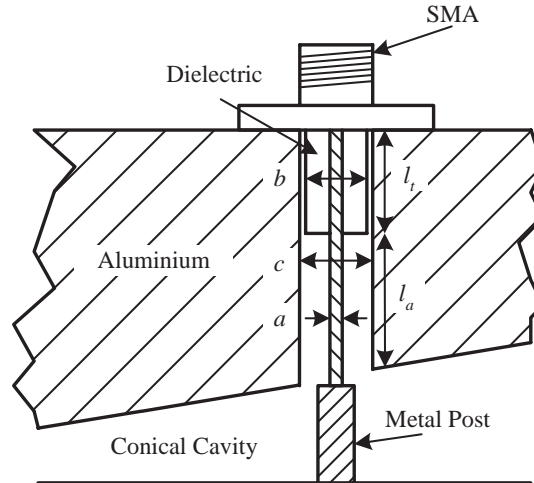


Fig. 4.1. Sketch of an extended dielectric SMA connector inserted into the top of the metal structure forming the peripheral feeding line matching network.

The feeding line is divided into two parts, the airline part of length  $l_a$  and impedance  $Z_a$ , and the partially filled line of length  $l_t$  and impedance  $Z_t$ . The dimensions  $a$  and  $b$  are fixed by the SMA connector and are  $a = 1.24\ \text{mm}$ , and  $b = 4.06\ \text{mm}$ . The impedance of the airline,  $Z_a$ , is therefore designed by changing the dimension  $c$ .

It is well known that the impedance of the partially filled line should be

$$Z_t = \sqrt{50Z_a}, \quad (4.1)$$

and the length,  $l_t$ , should be a quarter wavelength to match  $Z_a$  to  $50\ \Omega$ . The impedances of the airline and the partially filled line are related by

$$Z_t = Z_a / \sqrt{\epsilon_{\text{reff}}}, \quad (4.2)$$

with  $\epsilon_{reff}$  calculated as in (3.15). Substituting (4.2) into (4.1) and using (3.8), (3.15), and (3.16),  $c$  can be found as

$$c = b \exp \left[ \frac{1}{\epsilon_r} \left( \frac{5\epsilon_r}{6} - \ln \frac{b}{a} \right) \right]. \quad (4.3)$$

Using the dimensions given above for  $a$  and  $b$ ,  $c$  is found as  $c = 5.16$  mm. This gives  $Z_a = 85.6 \Omega$  and  $Z_t = 65.4 \Omega$ . However, due to the width of the flange on the available connectors (5.62 mm), to have a safety margin of about 0.4 mm on each side of the feed, the maximum diameter of  $c$  is limited to 4.82 mm. Choosing the diameter as  $c = 4.82$  mm, the impedance of the airline is  $Z_a = 80 \Omega$ , and that of the partially filled line  $Z_t = 60.1 \Omega$ .

The length of the matching line is calculated as

$$l_t = \frac{\lambda}{4\sqrt{\epsilon_{reff}}} = 5.64 \text{ mm}, \quad (4.4)$$

with  $\lambda$  the wavelength at the centre frequency (10 GHz), and  $\epsilon_{reff}$  calculated from (3.15). The length of the airline is also chosen as a quarter wavelength  $l_a = 7.5$  mm.

Results from a MWO simulation of the reflection coefficient looking into a  $80 \Omega$  line connected to a  $50 \Omega$  load through a quarter wavelength  $60.1 \Omega$  partially filled coaxial line are given in Fig. 4.2. It can be seen from Fig. 4.2 that the match is better than -20 dB from 8 to 12 GHz.

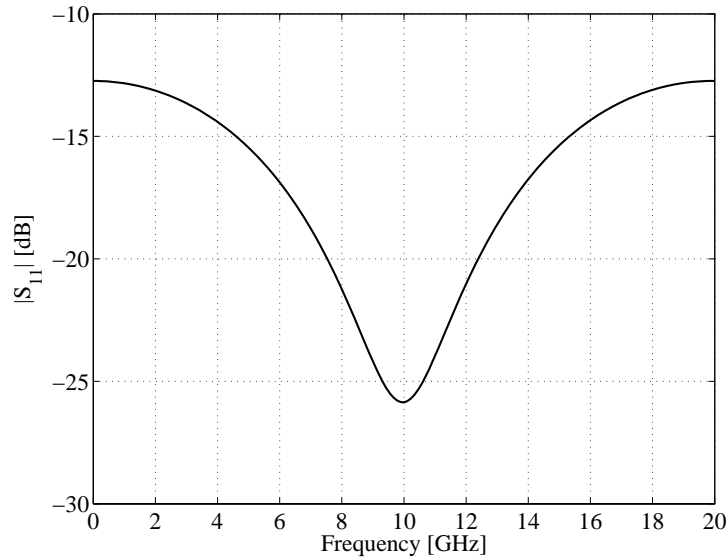


Fig. 4.2. MWO simulated reflection coefficient looking into an  $80 \Omega$  line matched to a  $50 \Omega$  load through a quarter wavelength  $60.1 \Omega$  partially filled coaxial line.

The same extendable posts from the design in Chapter 3 are again used as probes in this design, and the gaps between the probes and the outer conductors of the coaxial lines feeding them has been increased from 0.43 mm to 0.81 mm.

If, due to construction errors, the connector in Fig. 4.1 is not inserted exactly in the middle of

the hole with diameter  $c$ , the impedance of the lines will change slightly. CST-MWS simulations show that for a 0.1 mm offset the change is only 0.15%, and for a 0.2 mm offset the change is about 0.7%. These changes are negligible and do not have a significant effect on the matching of the lines.

## 4.2 Conical Line Design

To ensure a large gap between the inner and the outer conductors at the central feed point, a higher impedance is sought at the central conical to coaxial line transition than at the peripheral input ports. A matching section is therefore needed in the conical line to match these impedances over a wide band. Since a conical line is a uniform TEM transmission line, standard matching theory can be used. Quarter wavelength stepped impedance matching sections can be used in the conical line, but a disadvantage is the sharp edges formed by the impedance steps. Like a coaxial stepped impedance line [45], a stepped impedance conical line has step capacitances introduced by the sharp edges, and these are very difficult to compute accurately. The sharp edges also degrade the high power performance of the line. Steps in the line can be avoided by using a tapered line to do the impedance match. The Klopfenstein taper [47] has been shown to be the optimum matching section, in that for a specified tolerance of the reflection coefficient magnitude, the taper has minimum length [48].

The design of the conical transmission line in the common combining structure will be reported in this section. The effect of higher order modes when the diameter of the structure is increased will be discussed, as well as the design of the transmission line taper and back short distance.

### 4.2.1 Determination of Maximum Conical Line Length

For optimum matching performance using tapered lines, the tapered sections should have the maximum possible length. However, when the radial length (and therefore the diameter) of the combining structure is increased, a transmission zero is observed at a frequency which decreases as the diameter of the structure increases. The transmission coefficient results of two parameter sweeps in CST-MWS of an  $8 \Omega$  10-way combiner, much like the one shown in Fig. 3.9 but with  $80 \Omega$  peripheral airline feeds, with variable  $r_p$  and  $r_b$  (Fig. 3.4), are shown in Fig. 4.3.

To predict the frequency of the transmission zero, the field pattern at the frequency of the transmission zero must be studied. Fig. 4.4(a) shows the amplitude of the electric field pattern at the transmission zero frequency of 17.5 GHz, for a combiner like the one described above with  $r_p = 30$  mm and  $r_b = 7.5$  mm. This field pattern is remarkably similar to one of the higher order modes found with the eigenmode solver of CST-MWS for a  $8 \Omega$  conical cavity, with

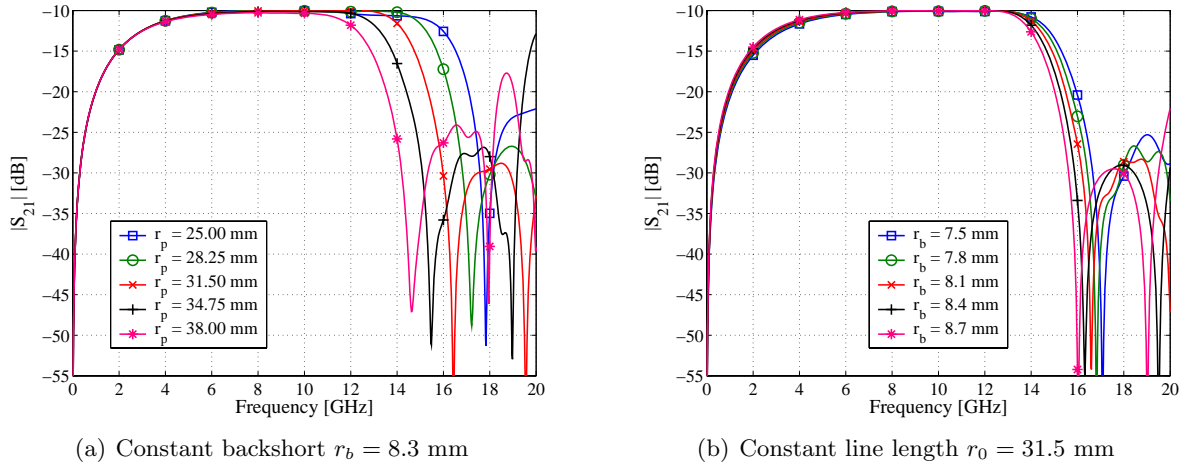


Fig. 4.3. Transmission coefficient of an  $8 \Omega$  10-way combiner showing the transmission zero effect with changing dimensions.

the same peripheral feeding probes inserted in the cavity as those used in the combiner. The eigenmode field pattern is shown in Fig. 4.4(b), and it has a resonant frequency of 16.3 GHz.

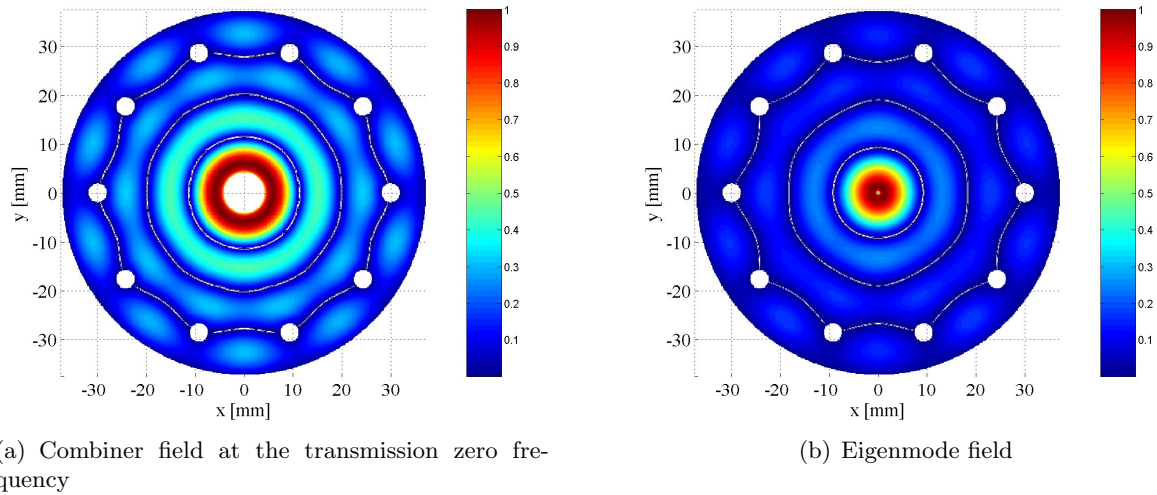


Fig. 4.4. Normalised amplitude of the electric field patterns in an  $8 \Omega$  combiner at the transmission zero frequency, and an eigenmode of a similar  $8 \Omega$  conical transmission line with peripheral feeding probes inserted.

From Fig. 4.4 it can be seen that when the combiner is driven symmetrically at the correct frequency, the structure becomes resonant and no energy will be coupled to the output ports. The difference in resonant frequency of the simple conical line and the combiner structure is due to the effect of the central transition in the combiner. This transition in effect shortens the conical cavity, and thus increases the resonant frequency.

The resonant frequency of the eigenmode shown in Fig. 4.4(b) can be predicted by using the similarity of the field to that of the  $TM_{003}$  mode in a simple conical cavity. The cavity wall

is formed by the peripheral probes at  $r_0 = r_p - d/2$ . Using (2.161), with  $p = 3$  and  $r_0 = 30 - 1.6 = 28.4$  mm, the resonant frequency is found as 15.83 GHz. When this is multiplied by the factor introduced by the shortening effect of the transition,

$$\Delta_f = \frac{r_0 + R_2}{r_0}, \quad (4.5)$$

with  $R_2 = 3.5$  mm, the predicted transmission zero frequency is 17.8 GHz, which is within 2% of the simulated value of 17.5 GHz, and it shows that (2.161) can be used as a good estimate of the resonant frequency. The difference between the predicted and simulated values is due to the  $r_b$  dependence, as shown in Fig. 4.3(b), which was not taken into account in the prediction. If  $r_b$  is kept smaller than  $\lambda/2$  at the resonant frequency, the predicted and simulated results are within 5% agreement.

The maximum radius that the peripheral probes can be placed from the axis in a conical combiner is therefore fixed by the frequency of the transmission zero. For a combiner designed to work in the 8–12 GHz band, and to allow tuning of  $r_b$ , it can be seen in Fig. 4.3(a) that a minimum frequency of around 17 GHz should be chosen. The approximate maximum radius can be found by incorporating (2.161) into (4.5) using  $r_0 = r_p - d/2$ , and substituting  $p = 3$  to find

$$r_p = \frac{3c + \sqrt{3c(3c + 8f_{\min}R_2)}}{4f_{\min}} + \frac{d}{2}. \quad (4.6)$$

Substituting  $f_{\min} = 17$  GHz into (4.6) gives a maximum radius of  $r_p \approx 31.5$  mm. The backshort distance  $r_b$  can still be tuned significantly to find the optimum reflection performance without compromising the transmission performance, as can be seen in Fig. 4.3(b).

When a taper is introduced into the transmission line, these results will change slightly, but (4.6) can still be used as a good initial estimate of a maximum conical line length.

### 4.2.2 Design of the Klopfenstein Taper

The maximum length of taper that can be used in the conical line is determined by the size of the central transition and of the peripheral port feeds. Taking point *A* in Fig. 3.6 as the maximum distance from the axis of the central transition, and allowing a length  $\delta_s$  of space on either side of the taper, the maximum length of the taper is found as

$$L_{\max} = r_0 - \frac{c}{2} - (R_2 + r_1) - 2\delta_s. \quad (4.7)$$

When  $\delta_s$  is chosen as 0.7 mm, the maximum length of the taper is found as  $L = 20$  mm.

The maximum reflection of a Klopfenstein taper can be calculated from [47] as

$$\Gamma_{\max} = \frac{\Gamma_0}{\cosh A}, \quad (4.8)$$

with the initial value of the reflection coefficient taken as

$$\Gamma_0 = \frac{1}{2} \ln \left( \frac{Z_2}{Z_1} \right), \quad (4.9)$$

and  $A$  defined by

$$A = \frac{2\pi L f_{\min}}{c}. \quad (4.10)$$

If the minimum frequency of the match is chosen as 8 GHz, the length of the taper as  $L = 20$  mm, the impedance at the end of the taper as  $Z_1 = 8 \Omega$ , and the maximum reflection as  $\Gamma_{\max} = -28$  dB (so as not to degrade the reflection performance of the combiner – see Section 5.2), the impedance at the central transition will be  $Z_2 = 25 \Omega$ . From (3.8) the gap between the conductors of the central coaxial airline will be 1.2 mm for a 25  $\Omega$  line, which is a significant improvement from the 0.28 mm gap in a 5  $\Omega$  line. The central conical to coaxial transition is designed as described in Section 3.3, but this time in a 25  $\Omega$  environment.

The impedance variation along the taper is given by [47] as

$$\begin{aligned} \ln(Z_0) &= \frac{1}{2} \ln(Z_1 Z_2) + \frac{\Gamma_0}{\cosh A} \left[ A^2 \phi \left( \frac{2x}{L}, A \right) + U \left( x - \frac{L}{2} \right) + U \left( x + \frac{L}{2} \right) \right], \quad |x| \leq L/2 \\ &= \ln(Z_2), \quad |x| > L/2 \\ &= \ln(Z_1), \quad |x| < -L/2. \end{aligned} \quad (4.11)$$

$U$  is the unit step function defined by

$$\begin{aligned} U(z) &= 0, \quad z < 0, \\ U(z) &= 1, \quad z \geq 0, \end{aligned} \quad (4.12)$$

and  $\phi$  is defined by

$$\phi(z, A) = -\phi(-z, A) = \int_0^z \frac{I_1(A\sqrt{1-y^2})}{A\sqrt{1-y^2}} dy, \quad |z| \leq 1. \quad (4.13)$$

Equation (4.13) may be rapidly evaluated by expanding the incomplete modified Bessel function  $I_1(A\sqrt{1-y^2})$  as a power series [49]. The function  $\phi(z, A)$  now becomes

$$\phi(z, A) = \int_0^z \frac{1}{2} \sum_{k=0}^{\infty} \frac{\left(\frac{A^2}{4}\right)^k (1-y^2)^k}{k!(k+1)!} dy, \quad (4.14)$$

which may be rewritten as

$$\phi(z, A) = \sum_{k=0}^{\infty} a_k b_k \quad (4.15)$$

where

$$a_k = \frac{(A^2)^k}{4^k k!(k+1)!} \quad (4.16)$$

and

$$b_k = \frac{1}{2} \int_0^z (1 - y^2)^k dy. \quad (4.17)$$

Next, recursion relations for  $a_k$  and  $b_k$  may be obtained, the  $b_k$  recursion being obtained through integration by parts:

$$\begin{aligned} a_0 &= 1; & a_k &= \frac{A^2}{4k(k+1)} a_{k-1} \\ b_0 &= \frac{z}{2}; & b_k &= \frac{\frac{z}{2}(1-z^2)^k + 2kb_{k-1}}{2k+1}. \end{aligned} \quad (4.18)$$

The impedance taper designed using (4.18) is shown in Fig. 4.5. The steps in impedance at

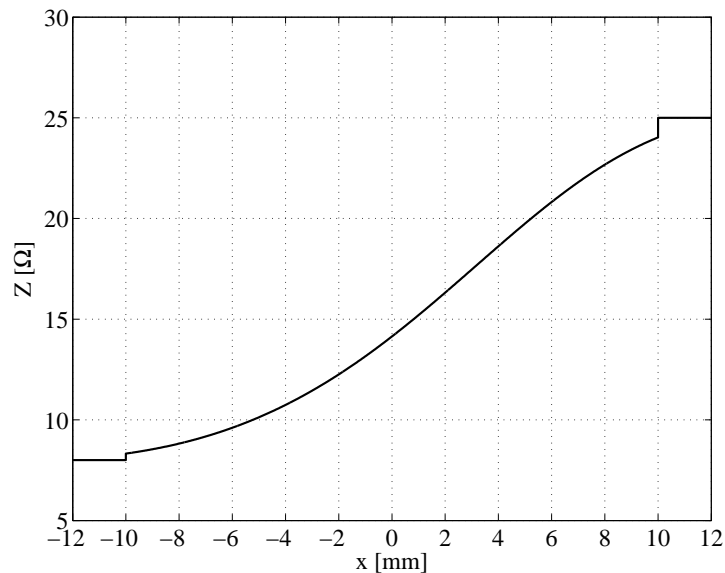


Fig. 4.5. Characteristic impedance of a 20 mm Klopfenstein taper matching an 8  $\Omega$  load to a 25  $\Omega$  line.

the ends of the taper are typical of a Klopfenstein taper, and these are smoothed away in the practical implementation in the conical line to maintain the high power performance of the structure. The taper is approximated in the conical line by 20 straight lines of length 1 mm (when a 2-D sectioned side view is taken). These lines connect the points specified by  $\theta_1$ , as calculated from the required impedance of the taper using (2.116), and the distance from the axis. The error introduced by this approximation is negligible, as can be seen by the 2-D profile of the taper in Fig. 4.6. The edges are smoothed by connecting the edge to a point on the taper 1 mm from the edge with a straight line, as shown in Fig. 4.7.

For comparison, a Hecken taper of the same length was also designed. Hecken proposed a near optimum taper [50, 51] which approximates the performance of a Klopfenstein taper but without the impedance discontinuities. A CST-MWS simulation was done of the Klopfenstein taper in a conical transmission line with the edge discontinuities smoothed away, and the results



Fig. 4.6. 2-D profile of the ideal and linear approximated smoothed Klopfenstein taper in a conical line without a central conical to coaxial transition. The red part is the ideal taper, and the black part the linear approximated smooth taper.



Fig. 4.7. 2-D profile showing the smoothed edge of the conical line Klopfenstein taper. The red part is the ideal taper, and the black part the linear approximated smooth taper.

are compared to the ideal Klopfenstein taper and also to the ideal Hecken taper in Fig. 4.8. Although the smoothed Klopfenstein taper has slightly worse performance than the ideal case

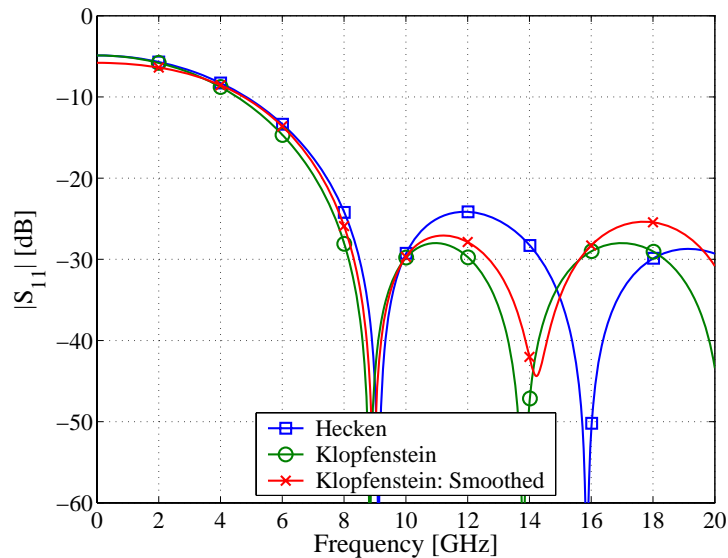


Fig. 4.8. Comparison of the reflection coefficients of an ideal and a smoothed Klopfenstein taper, as well as an ideal Hecken taper.

( $\Gamma_{\max} = -25.5$  dB compared to  $-28$  dB), the performance is still superior to that of the ideal Hecken taper ( $\Gamma_{\max} = -24$  dB).

### 4.2.3 Higher Order Mode Cutoff Frequencies

Since the impedance of the conical line in this design varies with radial distance, the calculation of higher order mode cutoff frequencies becomes more involved than for a simple constant impedance conical line. It is known from Fig. 2.8 that the 10-way combiner of Chapter 3 operates above the cutoff frequency of several of the  $TE_{m1}$  modes. From Figs. 2.6 and 2.7 it can be seen that, for a higher constant impedance combiner, the cutoff frequencies of the  $TE_{m1}$  modes will be higher, but the cutoff frequencies of the  $TE_{m2}$  and the  $TM_{mn}$  modes will be lower than those of a lower constant impedance combiner. If the tapered impedance combiner operates above the cutoff frequencies of the  $TE_{m1}$  modes and below the cutoff frequencies of the  $TE_{m2}$  and  $TM_{mn}$  modes, like the combiner designed in Chapter 3, it can be assumed that similar performance would be obtained.

The cutoff frequencies of several higher order modes in the tapered conical line are calculated using the technique described in Section 2.5. The impedance of the taper is sampled at a few positions on the taper, and the cutoff frequencies are calculated at these positions. Plots of these cutoff frequencies versus radial distance of the taper are shown in Figs. 4.9 and 4.10.

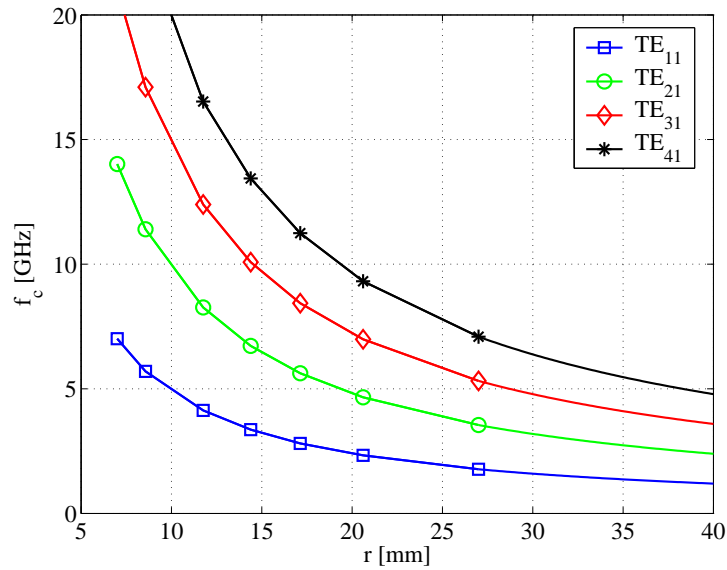


Fig. 4.9. Spatial variation of the cutoff frequency of the first 4  $TE_{m1}$  modes in a Klopfenstein tapered conical line.

The results in Figs. 4.9 and 4.10 make intuitive sense. The modes with little variation of the electric fields in the  $\theta$ -direction ( $TE_{m1}$ ), look much the same as those of a normal  $5 \Omega$  line plotted in Fig. 2.8. This is because a wider angle between the conductors will not significantly influence the mode pattern. For modes where the electric field is zero at the conductors ( $TE_{m2}$  and  $TM_{mn}$ ), however, the cutoff frequencies vary significantly with changing impedance. The

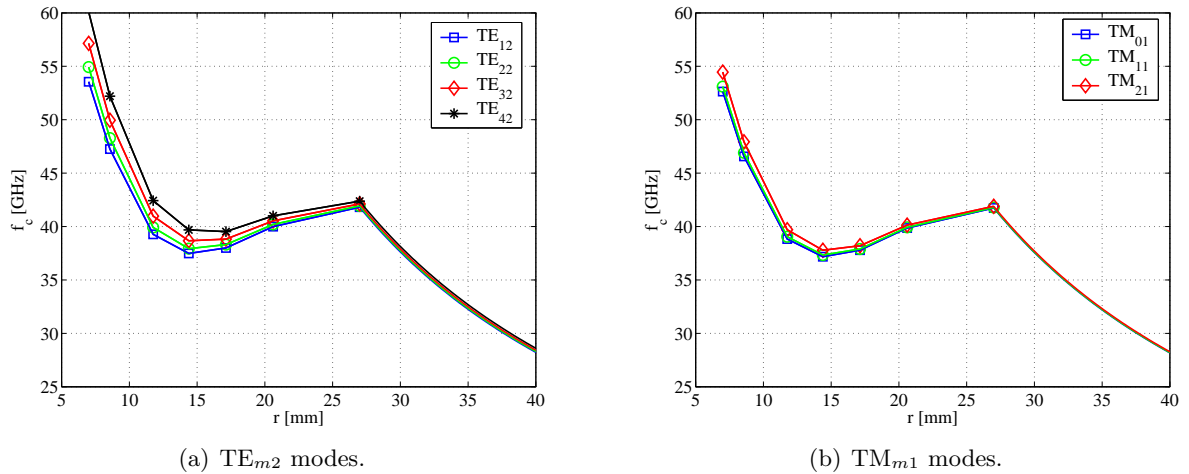


Fig. 4.10. Spatial variation of the cutoff frequency of the first few modes with electric field variations in the  $\theta$ -direction in a Klopfenstein tapered conical line.

effect of the tapered impedance line can clearly be seen in Fig. 4.10, in that the  $1/r$  dependence of the cutoff frequency is lost. Note that for  $27 \leq r \leq 40$  mm the impedance of the line is constant at  $8 \Omega$ , and the  $1/r$  dependence of all the cutoff frequencies is again clearly visible.

From the above results it is seen that the tapered line combiner is similar to the constant impedance combiner of Chapter 3, in that it operates above the cutoff frequency of the first few  $TE_{m1}$  modes, and below the cutoff frequency of all the other modes. Similar performance could therefore be expected in terms of isolation and balance.

#### 4.2.4 Simulation of the Combining Structure

As with the design in Chapter 3, the combining structure will be simulated and analytical transmission line models will be optimised outside the structure to obtain a wide matched bandwidth. Since the peripheral input ports have already been designed using analytical models in Section 4.1, only the impedance of the line at the central output port will be optimised, and therefore, only the reflection data from the common port is needed from the simulation. The CST-MWS model will include the full peripheral input ports with the matching sections in the input coaxial lines.

Like the previous design, the backshort length will be determined by a parameter sweep in CST-MWS. A screen shot of the model used in CST-MWS is shown in Fig. 4.11. Again only the TEM mode is considered in the design, and magnetic walls can again be inserted on the  $x$ - $z$  and  $y$ - $z$  planes. Only a quarter of the structure needs therefore be analysed. The input ports are standard SMA connectors with feeding lines designed as described in Section 4.1. The output port is a  $25 \Omega$  coaxial line. The CST-MWS result for the reflection coefficient looking into the

output port is shown in Fig. 4.12(a). A parameter sweep of  $r_b$  shows that a back short distance of  $r_b = 8.5$  mm gives minimum reflection at a centre frequency of 10 GHz. The transmission

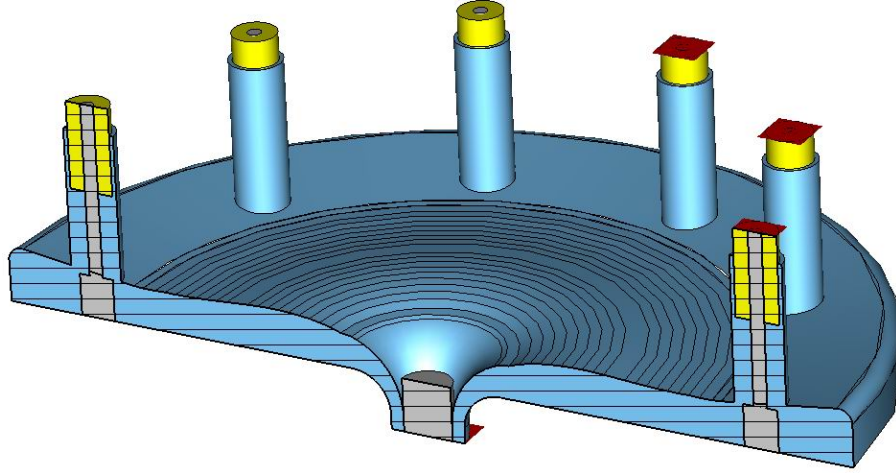
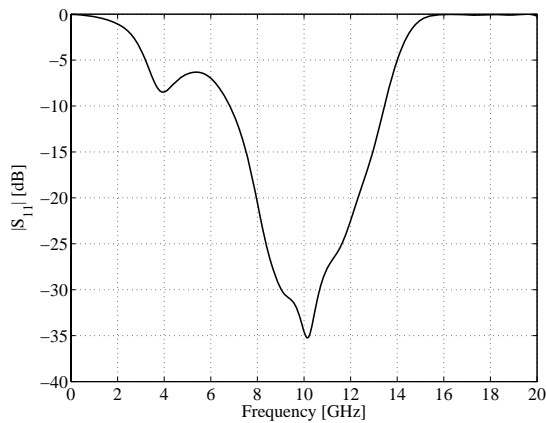
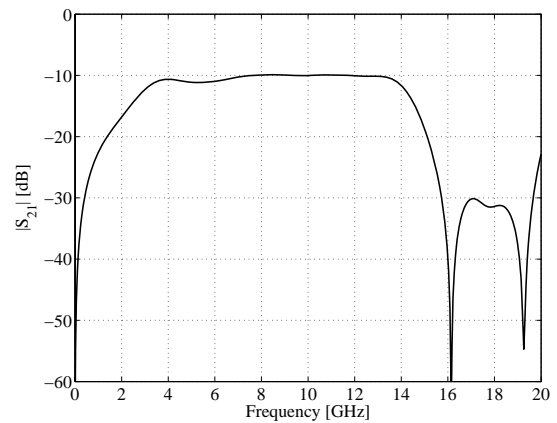


Fig. 4.11. CST-MWS screen shot of tapered 10-way combiner showing central conical to coaxial transition and peripheral feeding lines and ports. The background material as well as the grey parts are PEC, the blue part is vacuum, and the yellow parts are teflon. Ports are represented by red rectangles.



(a) Common central port reflection coefficient.



(b) Transmission coefficient.

Fig. 4.12. CST-MWS simulated results of the combining structure.

coefficient in Fig. 4.12(b) is very similar to the transmission coefficient of a similar size  $8 \Omega$  combiner plotted in Fig. 4.3(b).

### 4.3 Central Output Port Matching

To match the  $25 \Omega$  conical combining structure to a  $50 \Omega$  N-Type connector across the entire X-band, with no sharp edges in the matching network, an optimised taper is used in the feeding coaxial line. Since the diameter of the outer conductor of the coaxial line is fixed by the N-Type connector (7 mm), the diameter of the inner conductor is tapered. The optimisation is done in MATLAB using analytical transmission line models connected to the  $S$ -parameter box generated by a CST-MWS simulation in Section 4.2.4. A schematic representation of the two-port optimisation model is shown in Fig. 4.13. The model uses the transmission matrices of

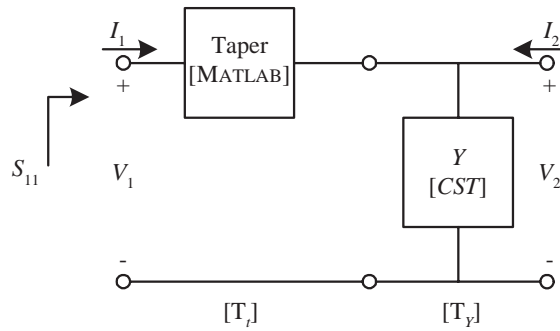


Fig. 4.13. Schematic representation of optimisation model for tapered central output line matching section.

the various parts to obtain the reflection coefficient of the whole system. The tapered matching section is represented by the transmission matrix  $T_t$ , which is terminated in the CST-MWS generated load  $Y$ , which is represented by the transmission matrix  $T_Y$ .

#### 4.3.1 Transmission Matrix Modelling

A tapered impedance transmission line can be modelled by breaking the line up into  $N$  short constant impedance lines with impedance  $Z_i$  and length  $l_i$ , and connecting these in cascade. The transmission matrix of one of these constant impedance lines is found as

$$\mathbf{T}_i = \begin{bmatrix} A_i & B_i \\ C_i & D_i \end{bmatrix} = \begin{bmatrix} \cos \beta l_i & jZ_i \sin \beta l_i \\ jY_i \sin \beta l_i & \cos \beta l_i \end{bmatrix}, \quad (4.19)$$

with  $Y_i = 1/Z_i$ . The transmission matrix of the tapered line is then found by multiplying all the transmission matrices of the cascaded sections as

$$\mathbf{T}_t = \begin{bmatrix} A_t & B_t \\ C_t & D_t \end{bmatrix} = \prod_{i=1}^N \mathbf{T}_i, \quad (4.20)$$

taking care to ensure that the order of matrix multiplication is correct.

The admittance of the frequency dependent load generated in CST-MWS is calculated from the reflection coefficient  $S$ -parameter as

$$Y = \frac{1}{Z_0} \frac{1 - S_{11}}{1 + S_{11}}. \quad (4.21)$$

The characteristic impedance  $Z_0$  is taken as  $25 \Omega$ , which is the impedance of the conical combiner at the central port. The transmission matrix of the admittance  $Y$  is calculated as

$$T_Y = \begin{bmatrix} 1 & 0 \\ Y & 1 \end{bmatrix}. \quad (4.22)$$

The input reflection coefficient  $S_{11}$  of Fig. 4.13 can be found by first multiplying the transmission matrices together to find

$$\begin{aligned} T &= T_t T_Y \\ &= \begin{bmatrix} A_t & B_t \\ C_t & D_t \end{bmatrix} \begin{bmatrix} 1 & 0 \\ Y & 1 \end{bmatrix} \\ &= \begin{bmatrix} A_t + B_t Y & B_t \\ C_t + D_t Y & D_t \end{bmatrix}. \end{aligned} \quad (4.23)$$

Using simple two-port network theory and (4.23), the voltage and current at port 1 is found as

$$\begin{aligned} V_1 &= (A_t + B_t Y)V_2 - B_t I_2 \\ I_1 &= (C_t + D_t Y)V_2 - D_t I_2. \end{aligned} \quad (4.24)$$

Setting  $I_2 = 0$  to represent the open circuit at port 2, the input impedance at port 1 is found as

$$Z_{\text{in}} = \frac{V_1}{I_1} = \frac{A_t + B_t Y}{C_t + D_t Y}. \quad (4.25)$$

The characteristic impedance of the input connector to the matching section is  $Z_0 = 50 \Omega$ , and the input reflection coefficient is thus found as

$$S_{11} = \frac{Z_{\text{in}} - Z_0}{Z_{\text{in}} + Z_0} = \frac{A_t + B_t Y - C_t Z_0 - D_t Y Z_0}{A_t + B_t Y + C_t Z_0 + D_t Y Z_0}. \quad (4.26)$$

The network represented by  $T_t$  can now be optimised with the target that  $S_{11}$  should be a minimum between 8 and 12 GHz.

### 4.3.2 Coaxial Taper Optimisation

Since accurate construction of complex smooth profiles is difficult, even when a CNC-lathe is used, a taper consisting of several linear sections in the centre conductor of the coaxial line is designed. Fig. 4.14 shows a 2-D profile of the taper with the definition of the optimisation

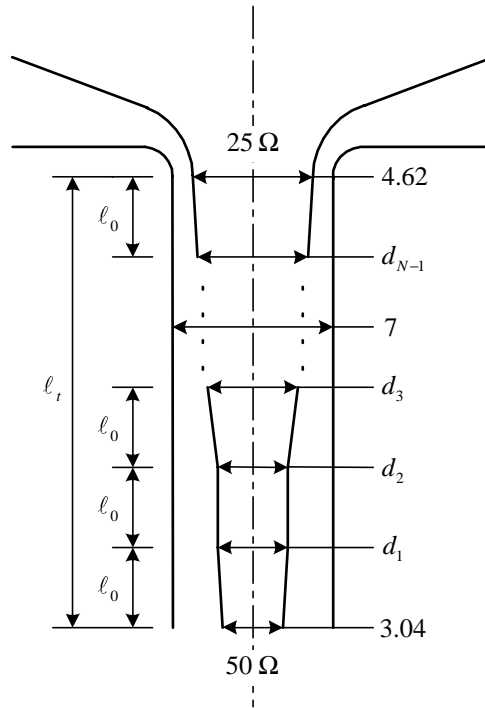


Fig. 4.14. 2-D profile of the coaxial taper showing optimisation variables.

variables. The total length of the taper is  $\ell_t$ , and it consists of  $N$  sections defined by the diameters  $d_n$  and the length  $\ell_0 = \ell_t/N$ .

The optimisation routine written in MATLAB optimises only the diameters  $d_n$  using a standard MATLAB function minimising procedure to yield a minimum  $S_{11}$  in the band 8–12 GHz.  $S_{11}$  is found by evaluating (4.26). The length of the taper is chosen as  $\ell_t = 20$  mm, since manufacturing becomes difficult if the coaxial line is too long. For easy manufacturing the diameters must be constrained so that  $d_{n+1} \geq d_n$ , with  $d_1 \geq 3.04$  mm, and  $d_{N-1} \leq 4.62$  mm. The number of sections  $N$  must also be kept to a minimum. A linear taper is used as the seed for the optimiser.

The reflection results of a five section taper (increasing the number of sections does not significantly improve the reflection performance) is shown in Fig. 4.15, and a MATLAB generated 2-D profile of the physical tapered coaxial line is shown in Fig. 4.16. The final values of the optimisation variables are  $d_1 = 3.18$  mm,  $d_2 = 3.74$  mm,  $d_3 = 4.09$  mm, and  $d_4 = 4.62$  mm. The length of the sections is  $\ell_0 = 4$  mm. The predicted reflection result from a CST-MWS simulation of the entire structure is also plotted in Fig. 4.15, and is in very good agreement with the MATLAB prediction. The return loss is better than -28 dB across the 8–12 GHz band.

#### 4.4 Summary of the Step-by-Step Design Procedure

The full design process can be summarised as follows.

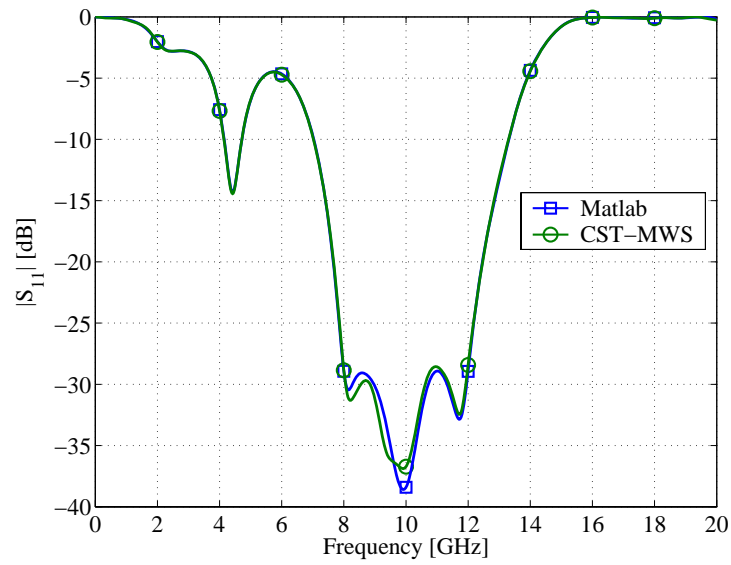


Fig. 4.15. Comparison of the simulated reflection coefficients of a matched 10-way tapered line conical power combiner.

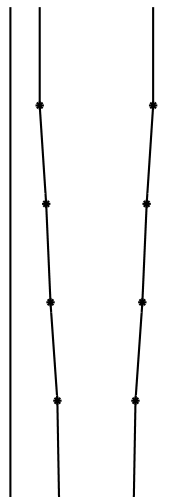


Fig. 4.16. MATLAB generated 2-D profile of the final coaxial taper showing optimisation variable positions.

1. Design the peripheral input port feeds using quarter wavelength partially filled coaxial lines to match the  $50 \Omega$  connectors to  $80 \Omega$  airlines feeding the conical line combining structure.
  - (a) The  $80 \Omega$  airline is formed by a standard SMA inner conductor inserted in a 4.82 mm diameter air cylinder forming the outer conductor of the coaxial line.
  - (b) A standard extended dielectric SMA connector inserted into the  $80 \Omega$  airline forms a partially filled coaxial line with an impedance of  $60.1 \Omega$ . This provides a good match between the connector and the airline.
  - (c) The length of the partially filled line is a quarter wavelength and is calculated using the effective relative permittivity of the line.
  - (d) The length of the airline is also chosen as a quarter wavelength.
  - (e) Determine the diameter of the feeding probes. Wider probes give better bandwidth, but the diameter is limited by the 4.82 mm outer diameter of the input feeding coaxial lines.
  
2. The combining structure is designed and the exact response of the structure, including peripheral input port feeds, is calculated with a full-wave solver.
  - (a) Determine the impedance of the outer part of the conical line from the number of ports as  $Z_0 = 80/N$ .
  - (b) Determine the radius  $r_p$  where the input ports are placed. The minimum distance is based on the width of the connectors, the spacing between the connectors and the number of connectors used. An estimate of the maximum distance is determined from (4.6). A smaller  $r_p$  will reduce higher order modes (see Chapter 5), but a larger  $r_p$  will provide for a longer, and therefore better, tapered line matching section.
  - (c) Determine the impedance at the central transition from the length of the taper used and the maximum return loss of the match from the equations given in [47].
  - (d) Construct the central transition between the conical and coaxial line as described in [12], using  $\theta_2 = 90^\circ$ , and calculating  $\theta_1$  from (2.116).
  - (e) Calculate the Klopfenstein impedance taper using the equations for the impedance variation given in [47]. The physical taper in the conical line is approximated by 20 straight lines, which connect points specified by  $\theta_1$ , which are calculated from the required impedance using (2.116) and the distance from the axis.
  - (f) Determine the length of the backshort  $r_b$  using a full-wave solver parameter sweep. Note that this becomes more difficult for larger structures – see Chapter 5.
  - (g) Analyse the entire structure, including the peripheral input ports, with a full-wave solver to get the reflection coefficient  $S$ -parameter at the central output port.

3. Optimise a tapered transmission line on the output of the combining structure, using analytical models in MATLAB, to achieve a wide matched bandwidth.

## 4.5 Construction and Measurement

The structure is again constructed from aluminium in two parts using a CNC-lathe, as described in Section 3.7. An extra flange was included in the bottom part of the structure to improve the mechanical stability. A 2-D section view of the entire structure with all the connectors, tuning posts and fastening screws included, is shown in Fig. 4.17. Some photographs of the structure are also shown in Fig. 4.18.

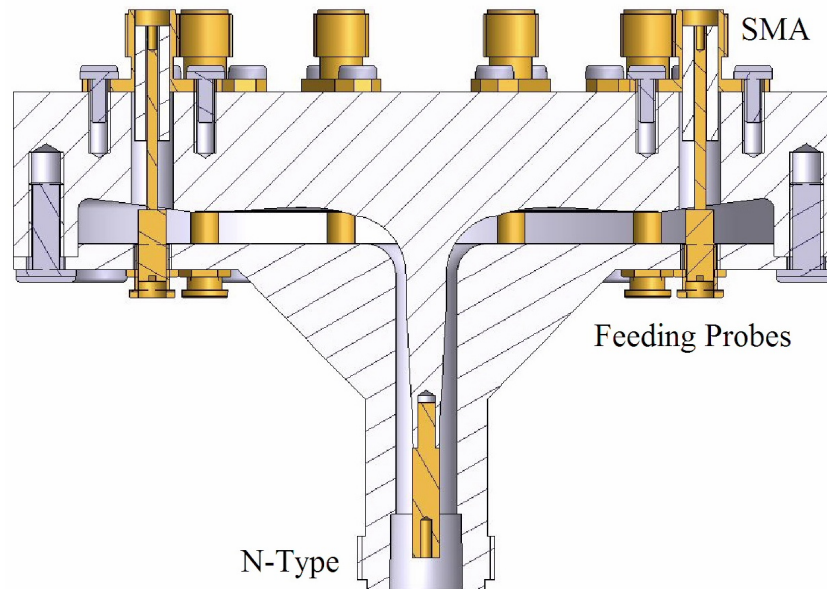


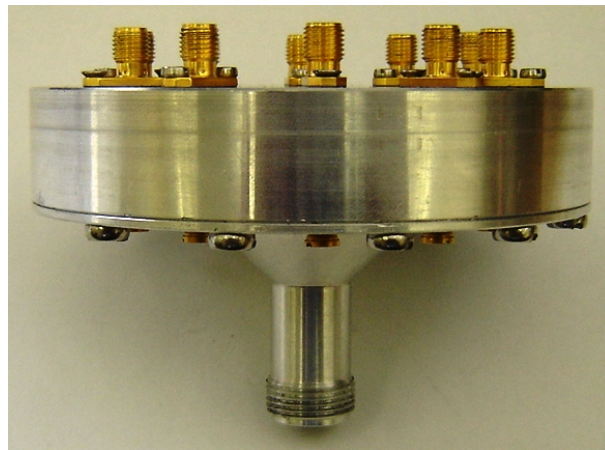
Fig. 4.17. 2-D section view of the tapered line conical combiner showing all connectors, feeding probes and fastening screws.

Two port measurements were again done on the 8510C VNA using precision SMA loads to terminate the ports that were not being measured.

The simulated and measured reflection results of the common port of the constructed combiner are shown in Fig. 4.19. A matched bandwidth of 47% is achieved with a maximum return loss of -18.5 dB, from 7.7 to 12.4 GHz. This match is narrower and deeper than the previous design in Chapter 3, and is in much closer agreement to the simulated results. Again, the biggest discrepancy is at low values of  $|S_{11}|$ . This is partly due to the SMA to N-Type adaptor used in the measurement, since no N-Type calibration kit was available to calibrate this effect out of the measurements. A voltage standing wave ratio (VSWR) of 1.1 is expected from the adaptor [52], which can be translated to a 55  $\Omega$  transmission line in a 50  $\Omega$  environment. If a 55  $\Omega$  line



(a) Separated top and bottom parts



(b) Fully assembled

Fig. 4.18. Photographs of the constructed 10-way tapered line combiner.

is inserted between two  $50\ \Omega$  ports in MWO, depending on the length of the line, the reflection can be as high as  $-20.5\ \text{dB}$ .

The measured transmission characteristics of the combiner are shown in Fig. 4.20. The simulated transmission coefficients are not shown since the simulated structure is perfectly symmetrical. A maximum amplitude imbalance of  $\pm 0.7\ \text{dB}$  and a phase imbalance of  $\pm 5^\circ$  are observed in the 8–12 GHz band. This is a  $\pm 0.3\ \text{dB}$  improvement on the amplitude balance results measured in Fig. 3.20(a).

The simulated and measured isolation characteristics of the combiner are shown in Fig. 4.21, where good agreement between the results is demonstrated. It is noted that the worst isolation is between port 2 and port 6, which is inconsistent with the measurements in Fig. 3.21 and with the remarks made in [5]. This effect will be investigated and explained in a Section 4.6.

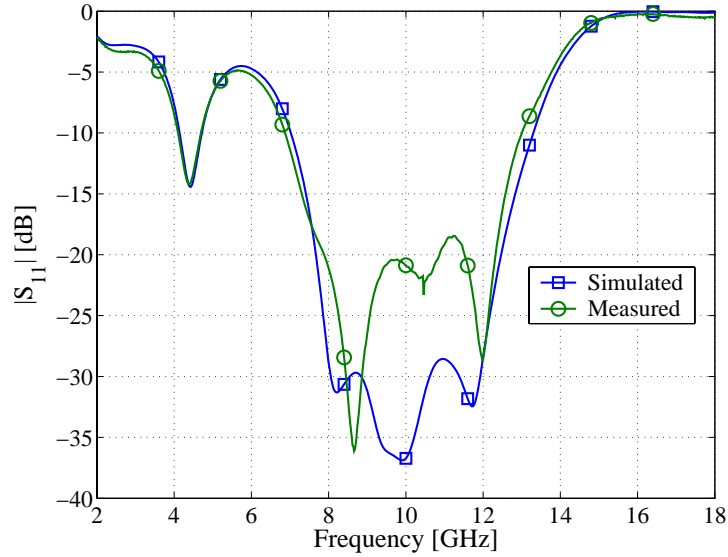


Fig. 4.19. Comparison between the simulated and measured reflection coefficient of a tapered line 10-way combiner.

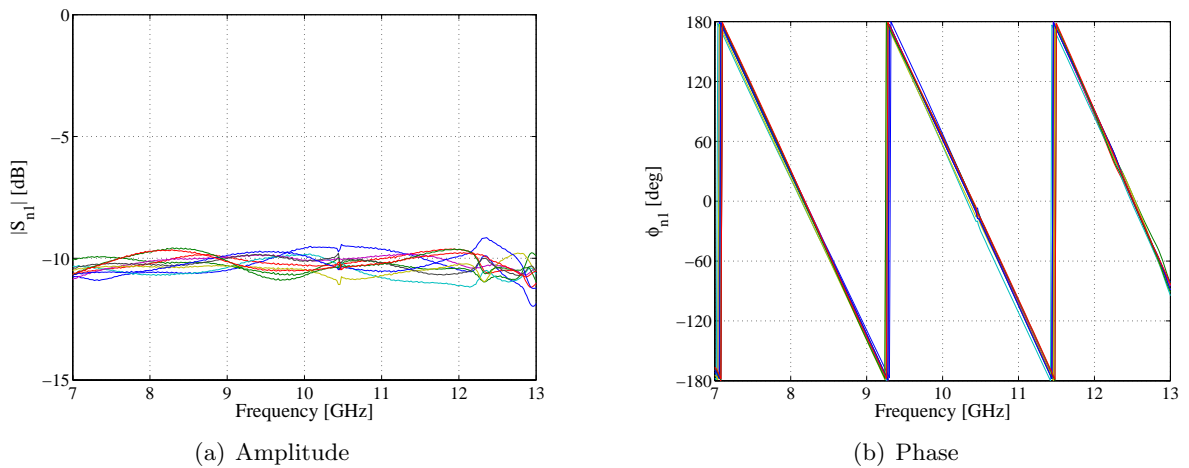


Fig. 4.20. Measured transmission coefficients in the operating band of a tapered line 10-way combiner ( $S_{n1}$  with  $n = 2, 3, \dots, 11$ ).

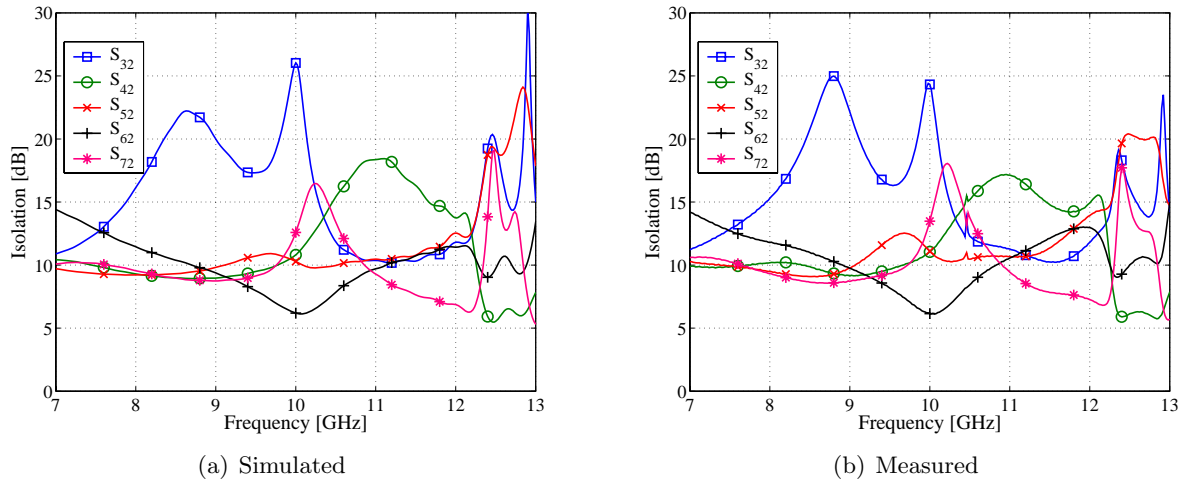


Fig. 4.21. Simulated and measured isolation in the operating band of a tapered line 10-way combiner.

Fig. 4.22 shows the total  $I^2R$  loss characteristic of the combiner. The maximum loss in the operating band is 0.28 dB, and the average loss only 0.18 dB. The loss includes the effects of the SMA transitions, as well as a SMA to N-Type transition used in the measurement setup. Again the simulated loss is not included, since the simulated structure is completely lossless.

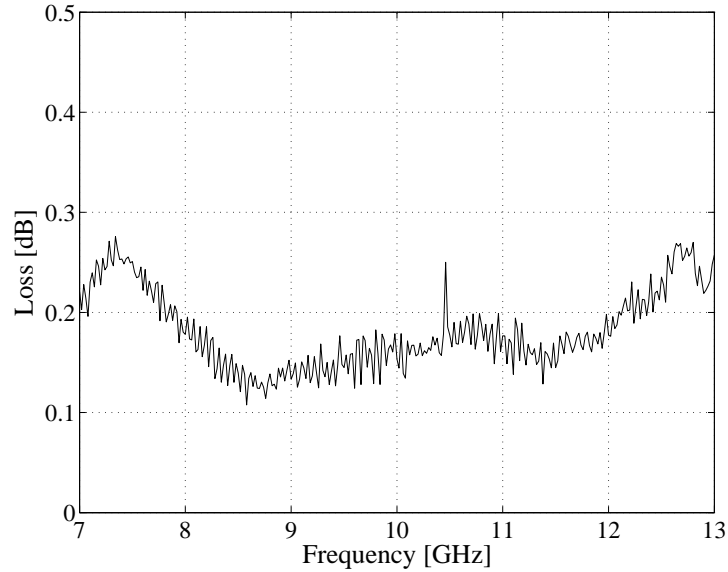


Fig. 4.22. Measured loss in the operating band of a tapered line 10-way combiner.

## 4.6 Isolation

The simulated zero-time H-field pattern in the combiner at 10 GHz when port 2 is driven and the other ports are terminated is shown in Fig. 4.23.

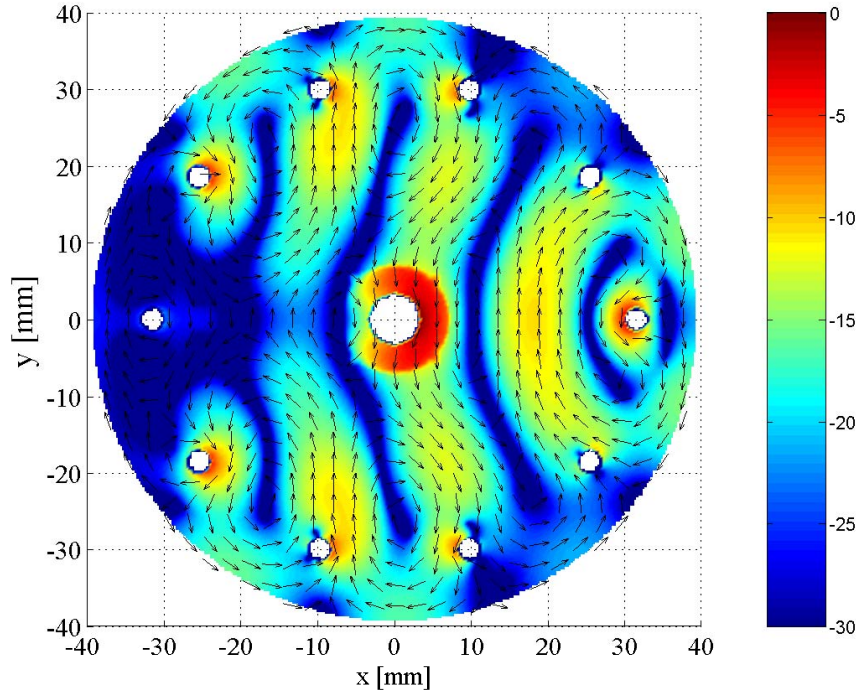


Fig. 4.23. Normalised absolute value (in dB) and direction of the simulated H-field pattern at zero-time in a 10-way tapered line conical combiner at 10 GHz when port 2 (see Fig. 3.5) is driven and the other ports are terminated.

As with the field pattern in Fig. 3.23, the H-field in Fig. 4.23 is similar to the H-field of one of the natural higher order modes in a conical transmission line. Although the mode pattern in Fig. 4.23 is again somewhat distorted due to the presence of the input probes and the unsymmetrical excitation, the H-field loops resemble those of the mode pattern of the ideal  $TE_{31}$  mode which, from (2.140), propagates in the region  $r > 14.6$  mm at 10 GHz. Since the structure is larger than the one designed in Chapter 3, it makes intuitive sense that a higher order mode than the one in the smaller structure will dominate when the structure is driven unsymmetrically.

The effect of this higher order dominant mode is seen in the isolation results of Fig. 4.21, where the worst isolation is no longer between opposite ports, but indeed between port 2 and port 6 (The exact same results are also valid for a number of other port combinations due to the symmetry of the structure). When the field pattern in Fig. 4.23 and the time averaged field strength in Fig. 4.24 are studied, the H-field in the vicinity of port 6, when compared to the fields in the vicinity of the other ports, most closely resembles that of the normal TEM H-field in a coaxial line and also has the highest average value. It can therefore be deduced that the strongest coupling is between port 2 and port 6, which is in agreement with the results in Fig. 4.21.

It is also interesting to note that the isolation results for the smaller combiner in Fig. 3.21

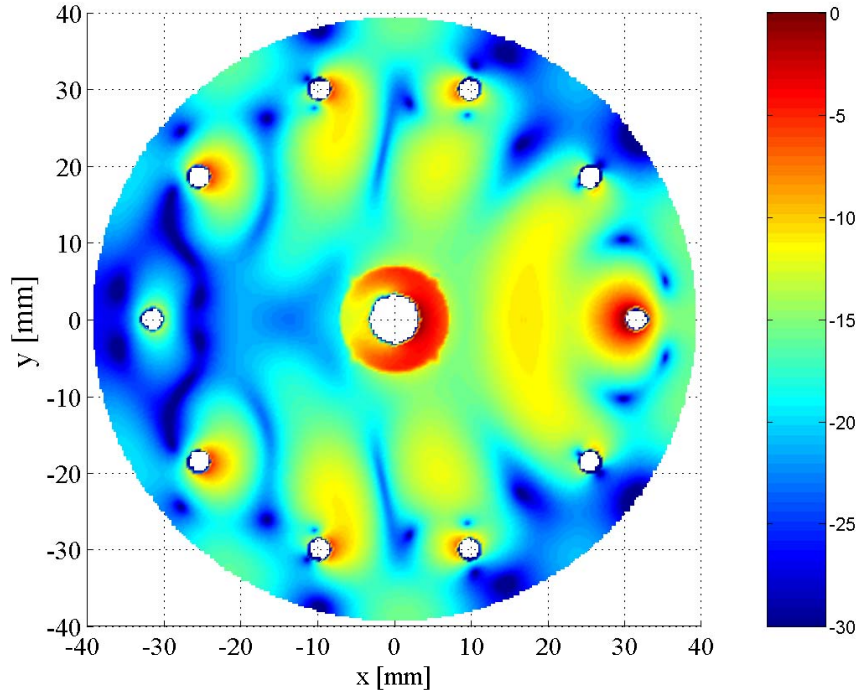


Fig. 4.24. Normalised absolute value (in dB) of the time averaged simulated H-field pattern in a 10-way tapered line conical combiner at 10 GHz when port 2 (see Fig. 3.5) is driven and the other ports are terminated.

around 12.9 GHz, are similar to the results for the larger combiner in Fig. 4.21 around 10 GHz. The frequency increase factor ( $\Delta_f = 1.29$ ) is almost exactly the same as the decrease in size ( $\Delta_r = 31.5/25 = 1.26$ ). This further confirms that the excitation of different higher order modes in structures of different electrical sizes causes the frequency dependence of the isolation.

## 4.7 Electric Field Strength and Peak Power Considerations

A 2-D section view of the simulated normalised magnitude of the TEM E-field at 10 GHz in the 10-way tapered line combiner is shown in Fig. 4.25.

In contrast to the field pattern in Fig. 3.25, the maximum field strength in a tapered line combiner is spread evenly through the high power central coaxial line due to the lack of any sharp corners in this design. This is confirmed by the plot of the E-field magnitude evaluated along the surface of the inner conductor, when compared to the results of a stepped impedance combiner in Fig. 3.26, shown in Fig. 4.26 (Note that the curve length of the tapered line combiner is longer than that of the stepped impedance case due to the larger size of the structure).

Fig. 4.26 clearly shows much lower peak E-field values for the tapered line combiner than those of the stepped impedance combiner. There are no sharp peaks in the E-field, except in the

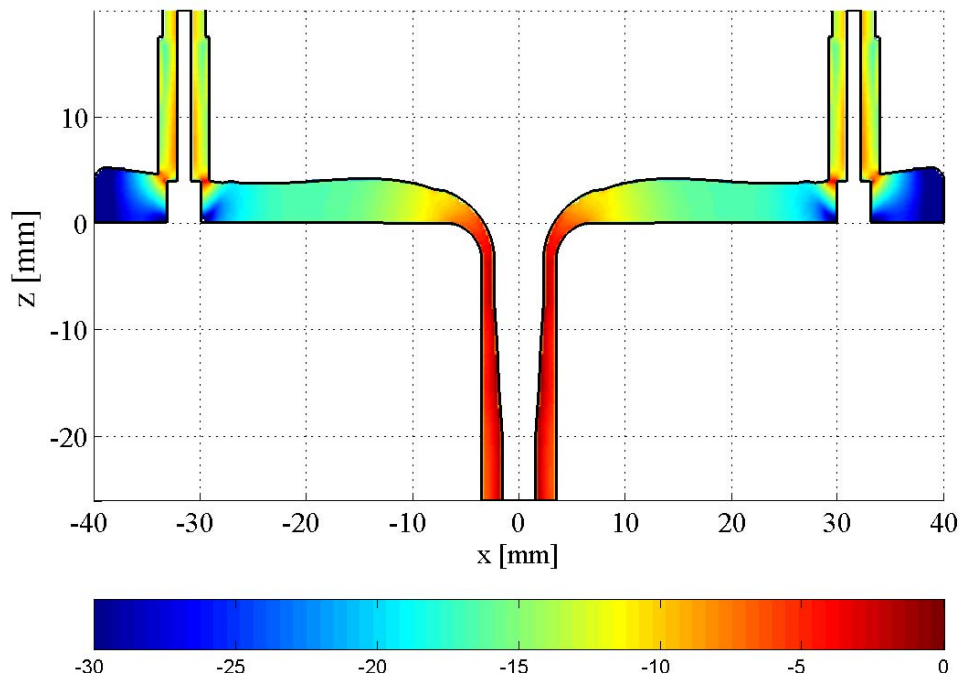


Fig. 4.25. 2-D section view of the normalised magnitude (in dB relative to 5.7 kV/m) of the TEM E-field in a 10-way tapered line combiner at 10 GHz with 1 W of input power.

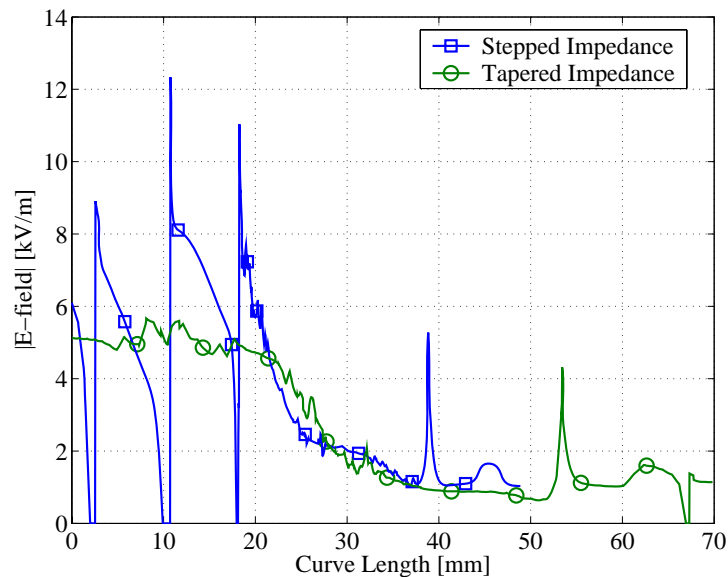


Fig. 4.26. Comparison of the magnitudes of the TEM E-fields, evaluated along a curve on the surface of the inner conductor of the central line from the central output port to one of the peripheral input ports, of a 10-way tapered line combiner with a 10-way stepped impedance combiner at 10 GHz with 1 W of input power.

vicinity of the corners at the peripheral ports. The E-field value here is, however, much lower than the field in the central part of the combiner due to the power combining action. The peak E-field strength in the tapered line combiner (5.7 kV/m) is about 2 times lower than that of the stepped impedance combiner (12.3 kV/m) for the same input power, and it can therefore be expected that the tapered line combiner has a 4 times greater peak power handling capability.

## 4.8 Conclusion

This chapter illustrates how the uniform TEM transmission line nature of the conical line can be exploited through the use of tapered lines. This leads to improved power handling and tolerance insensitive manufacture of a conical line power combiner.

By using simple quarter wavelength matching sections in the peripheral feeds, and a tapered line matching section in the conical line, the impedance at the central port is raised, which allows for easier matching to the output connector, and also more accurate construction. An optimised tapered line matching section is employed at the central output port to obtain wide band performance. Peak power handling capability of the combiner is increased since there are no sharp edges in the central high power parts of the structure.

A 10-way combiner, which demonstrates wide band performance, good amplitude and phase balance, and very low losses, was constructed. Measured results are in excellent agreement with predicted results obtained with a full-wave solver.

## Chapter 5

# General Design Strategy for N-Way Conical Combiners

In the previous two chapters two methods were presented for designing 10-way conical line combiners, which both displayed excellent performance. In this chapter a general design strategy will be presented for the design of  $N$ -way conical combiners. This strategy is developed by a detailed study of the main design parameters, namely size of the structure, match of the conical line impedance taper and the peripheral port matching. The field patterns inside the structures are investigated, and it is shown that higher order modes are indeed excited in symmetrically fed electrically large structures. These modes cause the reflection and transmission performance to differ from the highly predictable performance of electrically small TEM structures. The effect of different impedance tapers on performance is also studied, as well as the effect of the simple input matching section described in Section 4.1. The previous designs are critically compared to the general design strategy developed in this chapter, and a 30-way combiner is designed and simulated using the general strategy.

### 5.1 Effect of Size Variations in a Constant Impedance Combining Structure

In order to gain a better understanding of the operation of general  $N$ -way conical combiners, several simulated experiments were performed using CST-MWS for various constant impedance combiners with different numbers of ports. Ten-, 16-, and 20-way constant impedance combiners were analysed with varying radial size,  $r_p$ , and backshort distance,  $r_b$ , (see Fig. 3.4) in an effort to find predictable trends in the behaviour of combiners containing different numbers of ports. Such a trend was indeed recognised when it was found that the  $TE_{N/2,1}$  mode causes degraded performance in larger structures. Since the  $TE_{N/2,1}$  mode is meaningless in a structure with an

uneven number of input ports, simulations were also done of an 11-way combiner.

The peripheral input port feeds for all the combiners are  $80 \Omega$  airlines, as described in Section 4.1, without the matching section. Note that the impedance of the conical line in the combiners is now  $80/N$  in (3.7). The transition of [12] is used throughout as the central conical to coaxial transition, and no matching network is included at the central port.

### 5.1.1 Effects of Varying Size on the Reflection Coefficient

The reflection coefficient of a 10-way combiner is shown in Fig. 5.1 for a wide range of radial sizes and backshort lengths. It can be seen from Fig. 5.1 that for small structures (the meaning

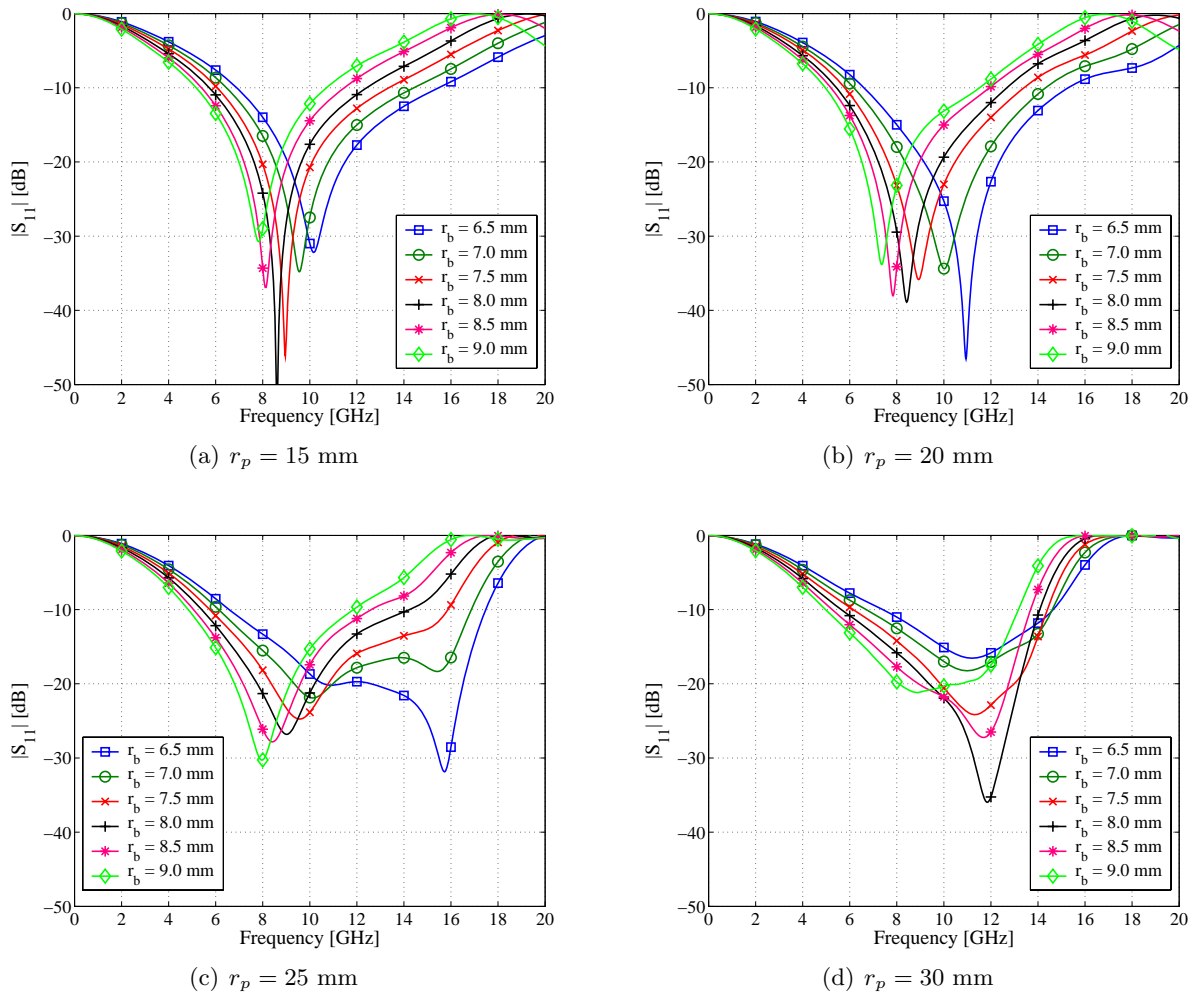


Fig. 5.1. Simulated reflection coefficients of several  $8 \Omega$  10-way combiners of different radial sizes and backshort lengths.

of 'small structures' will become clear later in this section) the reflection coefficient displays a reflection zero at the  $\lambda/4$  backshort frequency, as expected from a TEM combiner. Table 5.1 compares the expected reflection zero frequency due to the quarter wavelength backshort, and

the actual simulated value. From Table 5.1 and Fig. 5.1 it can be seen that, for small values of

TABLE 5.1

COMPARISON OF THE THEORETICAL QUARTER WAVELENGTH BACKSHORT REFLECTION ZERO FREQUENCY WITH THE SIMULATED VALUE IN AN  $8 \Omega$  10-WAY COMBINER FOR SMALL VALUES OF  $r_p$ .

$r_p$ [mm]	$r_b$ [mm]	$f_0$ [GHz]		% Difference
		Theory	CST-MWS	
15	6.5	11.5	10.2	-11.5
	7.0	10.7	9.6	-10.3
	7.5	10.0	9.0	-9.9
	8.0	9.4	8.6	-8.2
	8.5	8.8	8.1	-8.1
	9.0	8.3	7.8	-6.3
20	6.5	11.5	10.9	-5.5
	7.0	10.7	10.0	-6.6
	7.5	10.0	9.0	-9.9
	8.0	9.4	8.4	-10.3
	8.5	8.8	7.9	-10.4
	9.0	8.3	7.4	-11.1

$r_p$ , the simulated reflection zero frequency is between about 5 and 10 % lower than the predicted theoretical value. Similar results are obtained when an 11-, 16- or 20-way combiner is analysed, as can be seen in Fig. 5.2 and Table 5.2, which display the results for 16-way combiners of different radial sizes and backshort lengths, and also Fig. 5.3 for 20-way combiners.

TABLE 5.2

COMPARISON OF THE THEORETICAL QUARTER WAVELENGTH BACKSHORT REFLECTION ZERO FREQUENCY WITH THE SIMULATED VALUE IN A  $5 \Omega$  16-WAY COMBINER FOR SMALL VALUES OF  $r_p$ .

$r_p$ [mm]	$r_b$ [mm]	$f_0$ [GHz]		% Difference
		Theory	CST-MWS	
20	6.5	11.5	11.3	-2.0
	7.0	10.7	10.4	-2.9
	7.5	10.0	9.8	-1.9
	8.0	9.4	8.7	-7.1
	8.5	8.8	7.9	-10.4
30	6.5	11.5	10.0	-13.3
	7.0	10.7	9.5	-11.3
	7.5	10.0	8.9	-10.9
	8.0	9.4	8.4	-10.3
	8.5	8.8	7.9	-10.4

When  $r_p$  is increased, however, the behaviour of the reflection coefficient changes. As the radial size is increased and the backshort distance decreased, a knee starts to appear in the reflection response above the reflection zero frequency (from here on termed the  $S_{11}$  transition point),

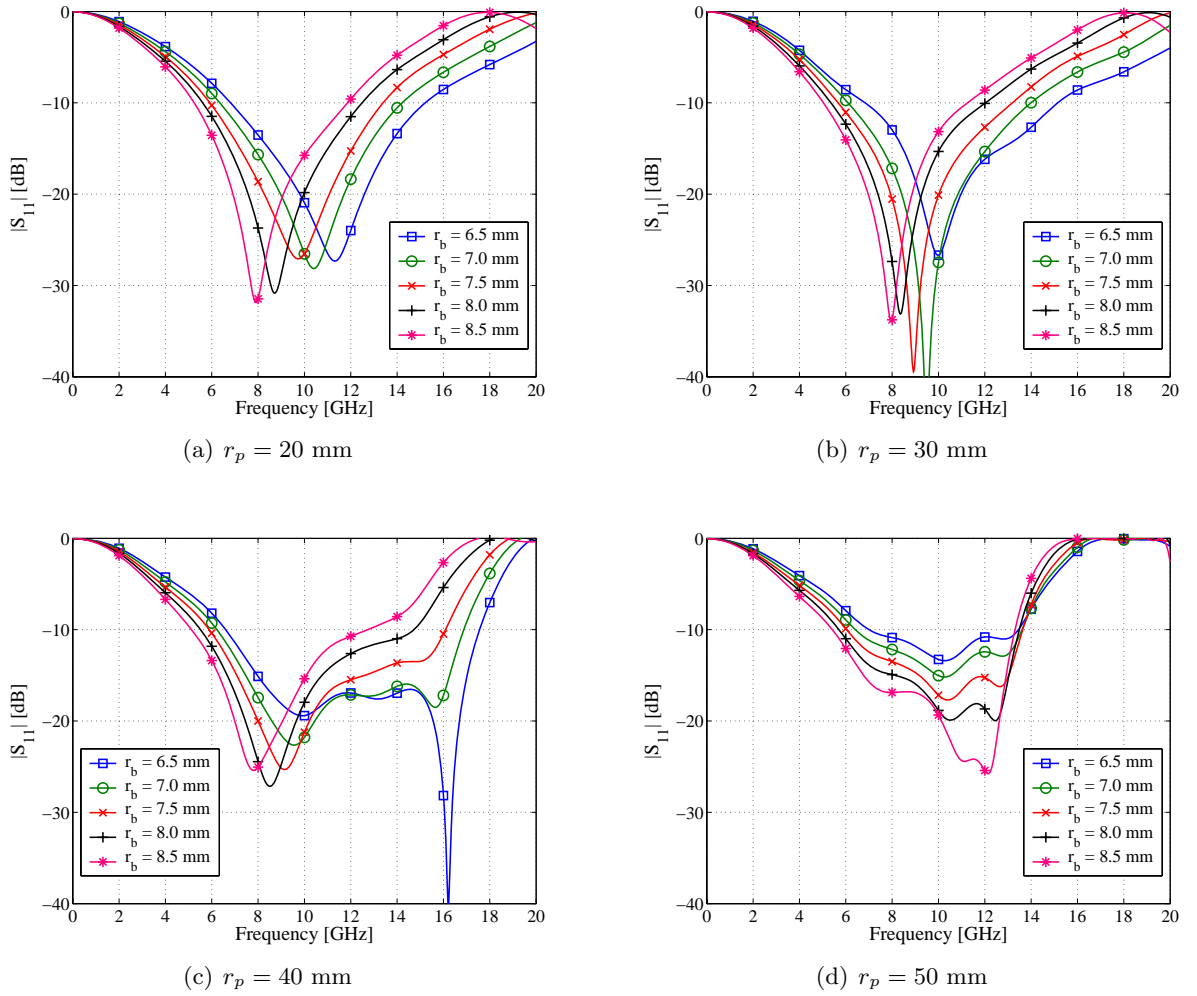


Fig. 5.2. Simulated reflection coefficients of several  $5 \Omega$  16-way combiners of different sizes and backshort lengths.

which later forms a spurious reflection zero and causes the expected reflection zero to disappear. In all the cases, the reflection performance becomes severely degraded in larger structures.

This degraded reflection performance can be attributed to the excitation of symmetrical higher order modes in electrically large structures, which have field patterns similar to the pattern depicted in Fig. 4.4(a). Even though the structure is driven symmetrically, higher order modes can still be excited, due to the position of the peripheral ports, when the structure is large enough. For combiners with an even number of peripheral ports, the  $TE_{N/2,1}$  mode can exist relatively undisturbed if the ports are in a region of the combiner which is above the cutoff frequency of the specific mode, as can be seen from the field plots in Section 2.6. In Fig. 5.1, the transition point for  $S_{11}$  is at  $r_p = 20$  mm and  $r_b = 6.5$  mm. Much the same result is also seen for  $r_p = 25$  mm and  $r_b = 8.5$  mm. The cutoff radius of the  $TE_{51}$  mode is calculated from (2.140) at a frequency of 11.53 GHz (which corresponds to a quarter wavelength of 6.5 mm) to be  $r_c = 20.74$  mm. At 8.8 GHz, which corresponds to  $r_b = 8.5$  mm, the cutoff radius is

$r_c = 27.1$  mm. In both these cases the total size of the structure ( $r_{\max} = r_p + r_b$ ) is about 1.25 times the cutoff radius at the centre frequency. Fig. 5.3 shows some reflection results for 20-way combiners, and Table 5.3 shows the total size of some of the structures at the  $S_{11}$  transition point compared to the cutoff radii of the  $\text{TE}_{N/2,1}$  modes at the centre frequency. Note that an approximate formula for the cutoff radius can be found by using the radius at the point at which the circumference is  $N$  half wavelengths at the desired frequency,

$$2\pi r_c = N(2r_b), \quad (5.1)$$

as shown in Table 2.1.

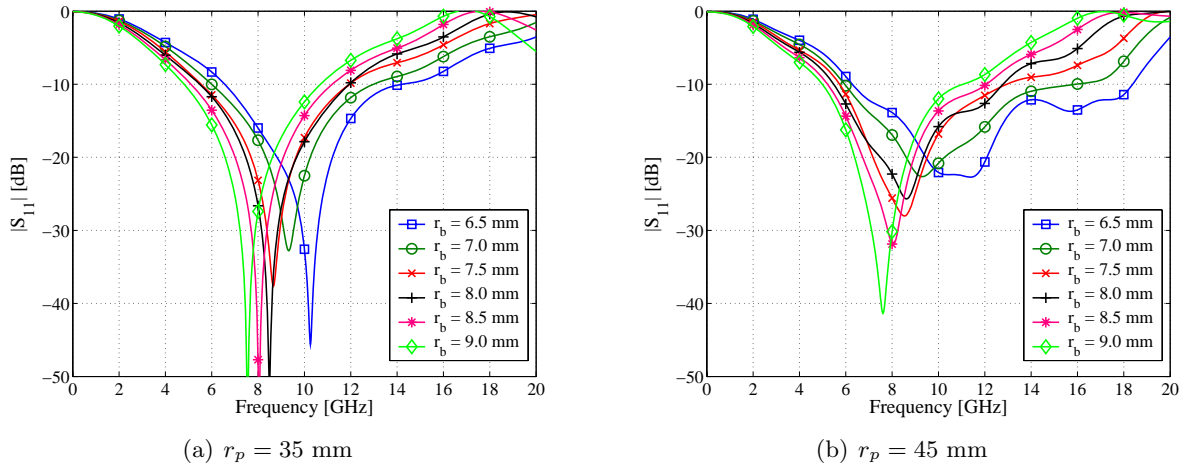


Fig. 5.3. Simulated reflection coefficients of several  $4 \Omega$  20-way combiners of different sizes and backshort lengths.

TABLE 5.3

COMPARISON OF THE CUTOFF RADIUS OF THE  $\text{TE}_{N/2,1}$  MODE AT THE THEORETICAL CENTRE FREQUENCY OF THE STRUCTURE TO THE TOTAL SIZE OF THE STRUCTURE AT THE  $S_{11}$  TRANSITION POINT.

$N$	$r_p$ [mm]	$r_b$ [mm]	$r_c$ [mm]		$\frac{r_{\max}}{r_c}$
			Exact	Approx	
10	20	6.5	20.7	20.7	1.3
	25	8.5	27.1	27.1	1.2
16	30	6.5	33.1	33.1	1.1
	40	8.5	43.3	43.3	1.1
20	35	7.0	44.6	44.6	0.9
	45	9.0	57.3	57.3	0.9

Table 5.3 confirms that a very good approximation of the cutoff radius can be found by using (5.1). More importantly, it shows that the reflection performance starts to degrade when the size of the structure is approximately the same as the cutoff radius of the  $\text{TE}_{N/2,1}$  mode. Also, in combiners with a larger number of ports, reflection performance starts degrading faster than in

combiners with fewer ports. It must be noted, however, that the above results are a conservative estimate of the maximum size where the reflection performance will still be acceptable since, as can be seen from Figs. 5.1, 5.2 and 5.3, the reflection performance is still good for some structures electrically larger than those given in Table 5.3. 'Electrically small' structures can now be defined in this context as structures smaller than those described above.

Very similar results were found with an 11-way combiner, but, because of the uneven number of ports, there is no natural conical mode that can exist between the ports. The ports do, however, cause a similar mode to the ones described above, to degrade the reflection performance in exactly the same way as for combiners with even numbers of ports. Since the cutoff radius of the mode cannot be calculated directly, a simple linear interpolation can be used between the cutoff radii of the natural modes above and below the uneven mode (the  $TE_{(N+1)/2,1}$  and  $TE_{(N-1)/2,1}$  modes) to find results similar to the ones in Table 5.3.

It is therefore possible to derive a conservative estimate for the maximum size of a  $N$ -way combiner to give predictable reflection performance. The study shows that the expected reflection zero occurs at a slightly lower frequency than that predicted by the length of the backshort, if the total radial size of the structure is kept smaller or equal to the cutoff radius of the  $TE_{N/2,1}$  mode at the frequency of the quarter wavelength backshort. If electrically larger structures are desired, the reflection performance is still good, but not as predictable as electrically smaller structures. More care must be taken when designing such large structures to ensure adequate bandwidth and the correct centre frequency. More will be said of this in the rest of the chapter.

### 5.1.2 Effects of Varying Size on the Transmission Coefficient

As with the reflection coefficient responses in Section 5.1.1, a transmission coefficient response from the central common port to one of the peripheral ports of a 10-way combiner is shown in Fig 5.4, for a wide range of radial sizes and backshort lengths. Again a difference is noted in Fig. 5.4 between the electrically small and the electrically large structures. In the small structures a transmission zero is observed at the frequency where the backshort is approximately half a wavelength - as expected from a TEM combiner. In the larger structures, the transmission zero is much less dependent on the backshort length, and the behaviour can be approximated by the technique described in Section 4.2.1. Table 5.4 compares the theoretically expected transmission zero frequencies to the simulated values, and also shows the relative total radial size of the structure, compared to the cutoff radius of the  $TE_{N/2,1}$  mode at the centre frequency. It can be seen in Table 5.4, that for electrically small structures, the transmission zero frequency can be very accurately predicted by using the frequency at which the backshort length is  $\lambda/2$ , and is therefore independent of the radial size of the combiner. Similar results are found for 11-,

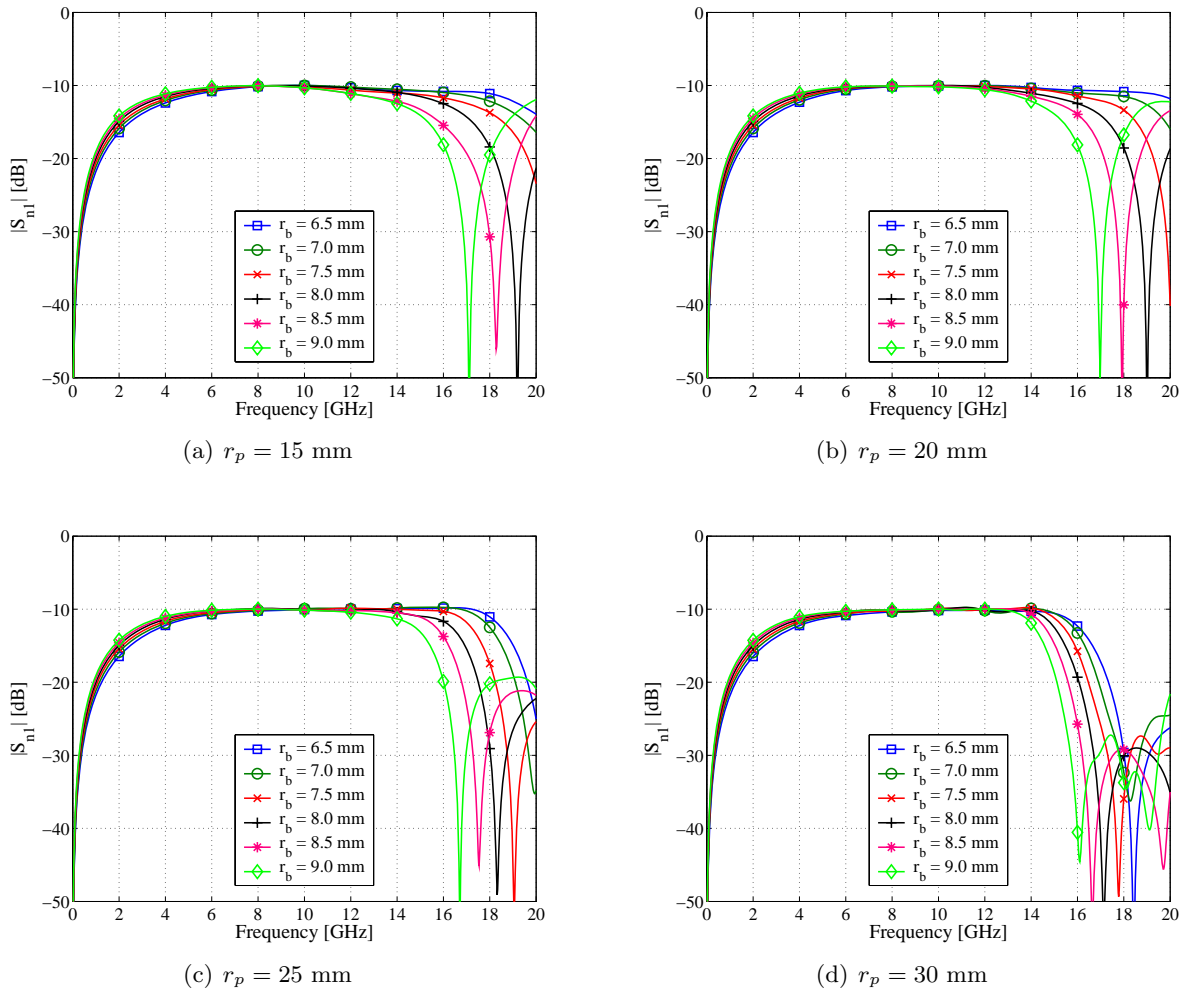


Fig. 5.4. Simulated transmission coefficients of several  $8 \Omega$  10-way combiners of different radial sizes and backshort lengths.

16- and 20-way combiners.

When the radial size of the structure is increased, the transmission zero frequency becomes more dependent on the radial size of the structure than on the length of the backshort, as was also shown in Section 4.2.1. The specific higher order mode causing the transmission zero is, however, not easy to predict for a  $N$ -way combiner. It was shown in Section 4.2.1 that for a 10-way combiner the transmission zero is mainly caused by the resonant  $TM_{003}$  mode within the probes. Similarly, for a large 20-way combiner, the transmission zero is mainly caused by the  $TM_{006}$  mode within the probes, and in a 16-way combiner by the  $TM_{005}$  mode. Fig. 5.5 shows the normalised absolute value of the resonant transmission zero electric field in a 16-way combiner with  $r_p = 50$  mm, and  $r_b = 7.5$  mm at 17.1 GHz. The cutoff radius of the  $TE_{81}$  mode at 10 GHz is 38.2 mm, which makes this structure 1.5 times the size of the cutoff radius and thus electrically large.

TABLE 5.4  
COMPARISON OF THE THEORETICAL HALF WAVELENGTH BACKSHORT TRANSMISSION ZERO  
FREQUENCY WITH THE SIMULATED VALUE IN AN  $8 \Omega$  10-WAY COMBINER.

$r_p$ [mm]	$r_b$ [mm]	$f_0$ [GHz]		% Difference	$\frac{r_{\max}}{r_c}$
		Theory	CST-MWS		
15	8.0	18.7	19.2	2.5	0.9
	8.5	17.6	18.3	3.8	0.9
	9.0	16.7	17.1	2.7	0.8
20	8.0	18.7	19.0	1.4	1.1
	8.5	17.6	17.9	1.5	1.1
	9.0	16.7	17.0	2.1	1.0
25	8.0	18.7	18.3	-2.3	1.3
	8.5	17.6	17.6	-0.5	1.2
	9.0	16.7	16.7	0.3	1.2
30	8.0	18.7	17.1	-8.7	1.5
	8.5	17.6	16.7	-5.6	1.4
	9.0	16.7	16.1	-3.3	1.4

The same technique can be used as in Section 4.2.1 to predict the transmission zero frequency with  $p = 5$ . These predictions are, however, very rough due to the  $r_b$  dependence shown in Figs. 4.3(b) and 5.4, and should be verified by simulation. For large combiners having different numbers of ports, the resonant mode causing the transmission zero is almost never known and must be found by simulation.

As before, it is therefore clear that, for electrically small combiners, the frequency of the first transmission zero can easily be predicted by taking the half wavelength frequency of the backshort distance. For larger structures it becomes increasingly more difficult to predict the transmission zero frequencies, and simulations have to be performed to determine which resonant mode is causing the transmission zero. These resonant higher order modes cause the severe degradation of reflection performance in electrically large combiners, and therefore limit the maximum size of such a combiner.

## 5.2 Effect of Different Impedance Matching Tapers in the Conical Line of the Combining Structure

As described in Chapter 4, the impedance of the conical line in a low impedance combiner has to be increased at the centre of the structure to obtain wider spacings between the conductors of the central transition and coaxial feed line. This is achieved by employing a Klopfenstein impedance taper in the conical line to match the low impedance peripheral part of the combiner to a higher impedance at the central part. The effect of several tapers, providing different levels

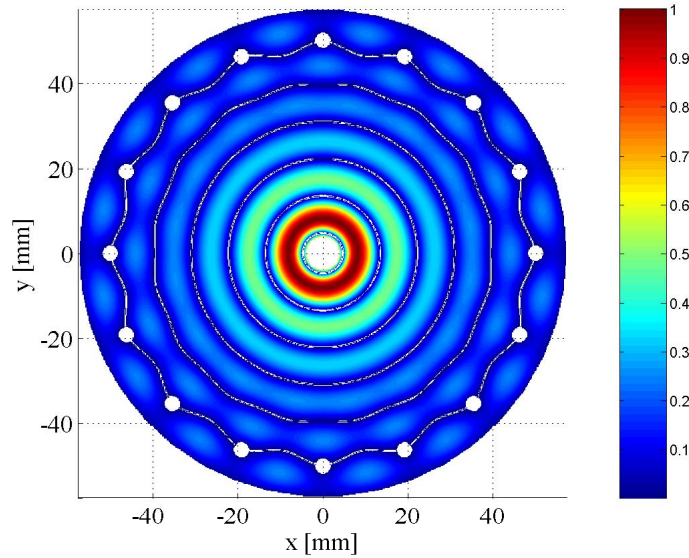


Fig. 5.5. Normalised absolute value of the electric field at the resonant transmission zero frequency (17.1 GHz) of an electrically large 16-way combiner with  $r_p = 50$  mm and  $r_b = 7.5$  mm.

of return loss, is simulated for both electrically small and electrically large structures. The effect that the taper has on the reflection performance of the combiner is investigated and a design guideline suggested.

Smoothed Klopfenstein tapers, like the one described in Section 4.2.2, are used in all the simulations. The reflection coefficients shown in the legends of Figs. 5.6 to 5.9, refer in all cases to the design value of the unsmoothed Klopfenstein taper used in the design. If a different taper, like the Hecken or exponential type, is used the results may differ slightly and should be checked carefully. The smoothed Klopfenstein taper is preferred here due to its superior performance, as shown in Fig. 4.8.

### 5.2.1 Effect of Tapers in Electrically Small Structures

To investigate the effect on the return loss of an electrically small combiner when an impedance taper is introduced in the conical line, a 16-way combiner is analysed with  $r_p = 30.7$  mm and  $r_b = 7.5$  mm, which makes the radial size of the combiner exactly the same as the cutoff radius of the  $TE_{81}$  mode at 10 GHz. Tapers with a return loss of  $-20$ ,  $-23$ ,  $-25$ , and  $-30$  dB are used (Note that in order to fit the  $-30$  dB taper in the conical line, a maximum impedance step of only 5 to 15  $\Omega$  is possible). Fig. 5.6 shows the resulting reflection coefficients of the combiner containing the different tapers. For tapers with a return loss of  $-23$  dB and higher, a slight shift in the centre frequency of the reflection coefficient of the combiner is observed. However, the reflection coefficients of the combiners containing the  $-25$  and  $-30$  dB tapers show excellent

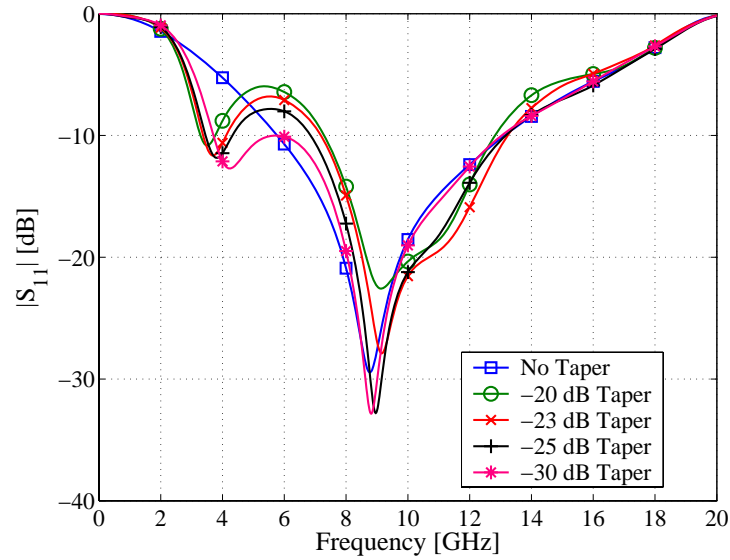


Fig. 5.6. Reflection coefficients of electrically small ( $r_p = 30.7$  mm and  $r_b = 7.5$  mm)  $15 \Omega$  common port 16-way combiners with varying return loss conical line impedance tapers.

agreement with that of the  $5 \Omega$  constant impedance combiner.

When the length of the backshort is reduced to  $r_b = 6.3$  mm, the centre frequency of the  $5 \Omega$  constant impedance combiner is moved to exactly 10 GHz. The same tapers as above were inserted in the structure, and the resulting reflection coefficients are shown in Fig. 5.7. These

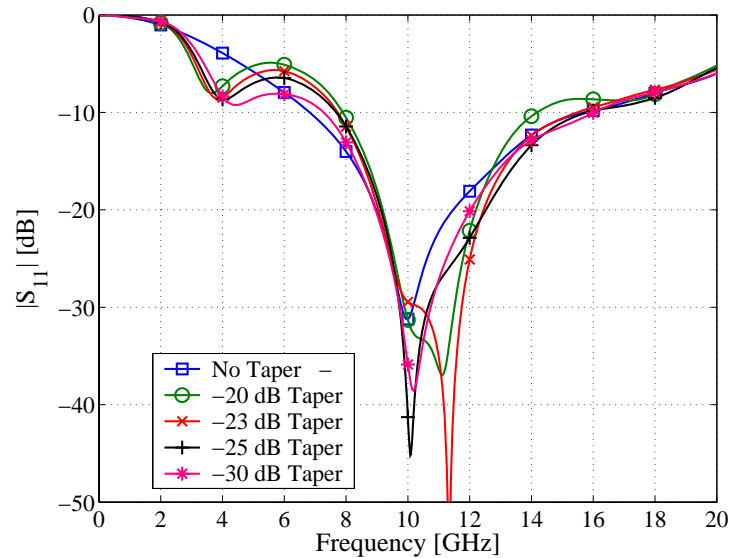


Fig. 5.7. Reflection coefficients of electrically small ( $r_p = 30.7$  mm and  $r_b = 6.3$  mm)  $15 \Omega$  common port 16-way combiners, tuned to 10 GHz, with varying return loss conical line impedance tapers.

combiners are slightly larger than the cutoff radius of the  $TE_{81}$  mode at the theoretical centre frequency of 11.9 GHz (1.2 times), but Fig. 5.7 shows that tapers with a return loss of better than  $-25$  dB produce reflection results very similar to those of the simple constant impedance

combiner.

### 5.2.2 Effect of Tapers in Electrically Large Structures

The effect of the impedance taper in the conical line on the return loss of electrically large structures is investigated by analysing 10-way combiners with  $r_b = 31.5$  mm and  $r_b = 7.5$  mm, which makes the radial size of the combiner 1.6 times the cutoff radius of the  $TE_{51}$  mode at 10 GHz. To be comparable to the combiner designed in Chapter 4, the impedance levels are chosen as 8 - 25  $\Omega$ , and the taper return losses as -20, -23, -25, and -28 dB. Fig. 5.8 shows the reflection coefficients. Due to the fact that all the tapers have a better return loss than that

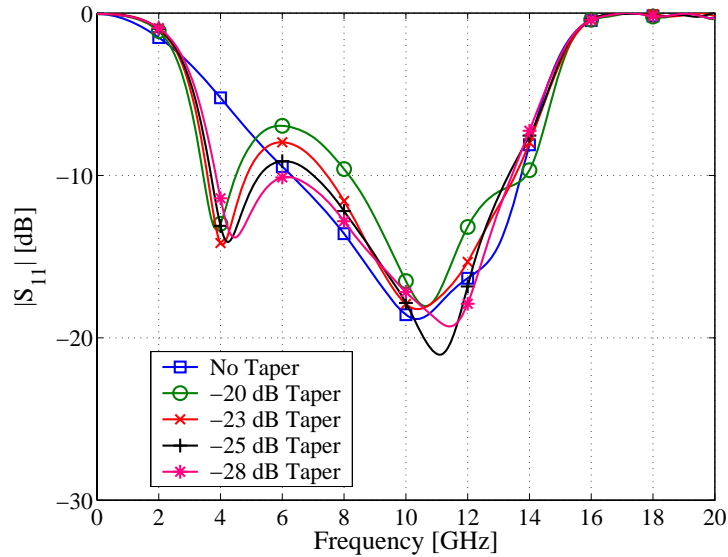


Fig. 5.8. Reflection coefficients of electrically large ( $r_p = 31.5$  mm and  $r_b = 7.5$  mm) 25  $\Omega$  common port 10-way combiners with varying return loss conical line impedance tapers.

of the simple constant impedance combiner, the effect of the different tapers is not apparent in Fig. 5.8. More degradation of the reflection performance is, however, noticed in the -20 dB taper combiner.

When the length of the backshort is increased to 8.5 mm, like the combiner in Chapter 4, the cutoff radius of the  $TE_{51}$  mode is increased, and therefore the radial size of the structure is reduced to 1.4 times the cutoff radius of the  $TE_{51}$  mode at the theoretical centre frequency of 8.8 GHz. Here, as Fig. 5.9 shows, a reflection zero does exist, but it is shown in Section 5.1.1 that it is not easy to predict the frequency thereof. Tapers with a return loss of better than -28 dB give the most predictable performance, even though a slight shift in frequency of the transmission zero is still noticed. This is due to the fact that the tapered conical line is not entirely TEM anymore at the large radii, and therefore starts giving some unpredictable results. For a large structure such as this, where a reflection zero is still achieved, the tapers and indeed

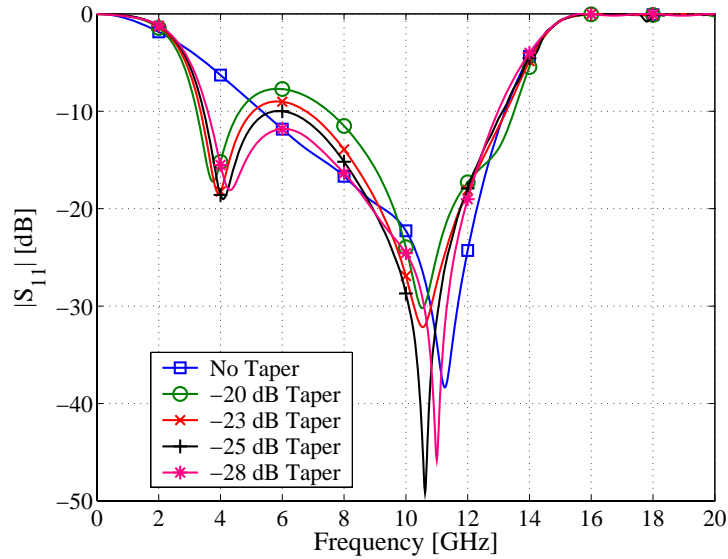


Fig. 5.9. Reflection coefficients of electrically large ( $r_p = 31.5$  mm and  $r_b = 8.5$  mm)  $25 \Omega$  common port 10-way combiners, tuned to about 10 GHz, with varying return loss conical line impedance tapers.

the combiner can still be used, but more care must be taken in the tuning of the backshort length to achieve the desired centre frequency.

### 5.3 Effect of the First Order Peripheral Input Port Matching Sections

To match the  $80 \Omega$  peripheral input feeds to a  $50 \Omega$  connector, a simple first order quarter wavelength matching section was used in Section 4.1, where the ideal impedance levels could not be used due to construction limitations. This could be overcome by using connectors with wider flanges, or by taking care to place the connectors very accurately during construction, and therefore having a smaller safety margin than the 0.4 mm used in Section 4.1. The effect that the non-ideal first order match has on the reflection performance of electrically small and large combiners is investigated in this section. For wider bandwidth applications, an optimised matching section, such as the one described in Section 3.5.1, can be employed. It should be kept in mind that these matching sections are normally much harder to construct than the simple first order ones.

#### 5.3.1 Effect of First Order Input Match on Electrically Small Combiners

A 20-way combiner with  $r_p = 35$  mm and  $r_b = 6.5$  mm has the same total radial size as the cutoff radius of the  $TE_{10,1}$  mode at 11.5 GHz, and is used here as the electrically small combiner. A taper with a  $-27$  dB return loss was incorporated in the structure to raise the impedance to  $25 \Omega$

at the central port. Note that for the ideal matching section the impedance of the feeding lines must be raised from 80 to 85.6  $\Omega$ , and the impedance of the outer part of the conical line changed accordingly. Fig. 5.10 shows the effect that the non-ideal and the ideal input matching sections have on the reflection of the combiner. It can be seen in Fig. 5.10 that while the combiner with

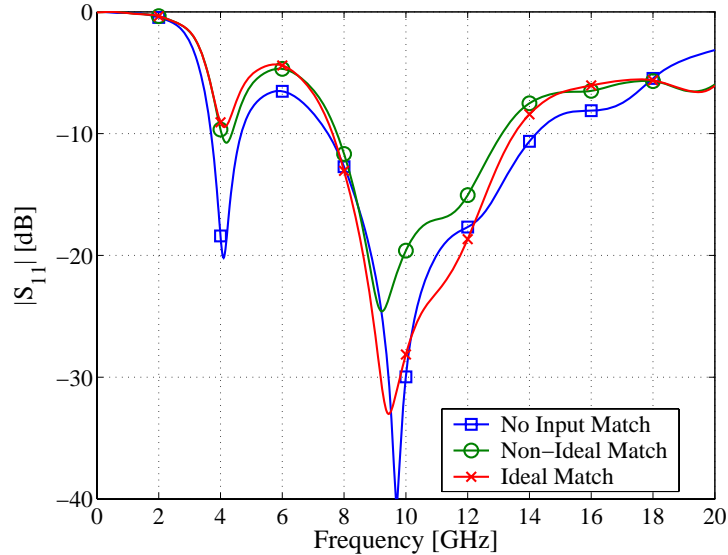


Fig. 5.10. Comparison of the reflection coefficients caused by adding non-ideal and ideal first order input matching sections to an electrically small ( $r_p = 35$  mm and  $r_b = 6.5$  mm) 20-way combiner containing a -27 dB conical line taper.

the ideally matched inputs displays good reflection performance, the non-ideal match degrades the reflection performance of the combiner. Thus, for electrically small combiners, it is advisable to have a very good and well tuned match from the input feeds of the combiner to the peripheral port connectors.

### 5.3.2 Effect of First Order Input Match on Electrically Large Combiners

For the electrically large case a 10-way combiner with  $r_p = 31.5$  mm and a -28 dB taper is used. The impedance at the central port is 25  $\Omega$ . Fig. 5.11 shows the reflection coefficient of the combiner with the non-ideal input matching section included for different values of  $r_b$ . From Fig. 5.11 it can be seen that a good match can be achieved if the backshort length is tuned to  $r_b = 8.5$  mm, even if the input matching sections are not ideal. This is the exact case that was used for the design in Chapter 4. Slightly worse results, with reduced bandwidth, are achieved when an ideal first order matching section is used in the input lines, as can be seen in Fig. 5.12. When these results are compared to Fig. 5.9 it is seen that the input matching section has a large effect on the reflection coefficient of the combiner. It is therefore apparent that when an electrically large combiner is designed, the length of the backshort must be determined by simulations in order to obtain the desired operating frequency. Also, this must be done after

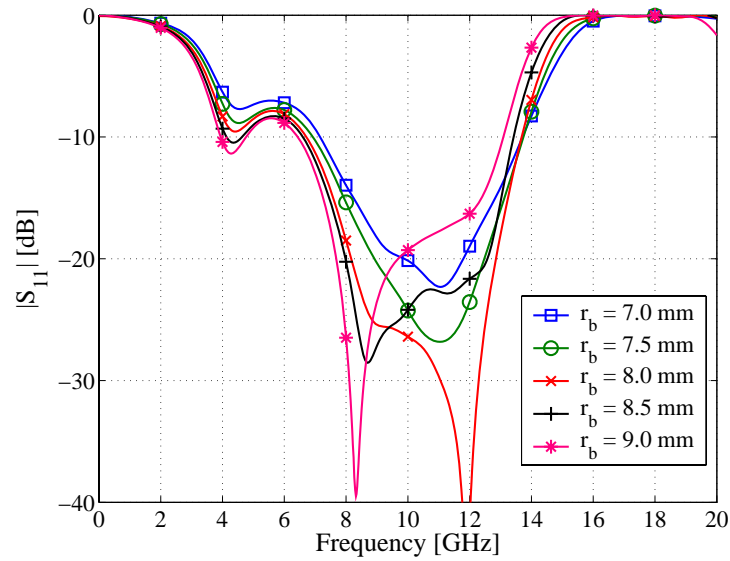


Fig. 5.11. Comparison of reflection coefficients caused by adding non-ideal first order matching sections to an electrically large ( $r_p = 31.5$  mm) 10-way combiner, containing a -28 dB conical line taper, for different backshort lengths.

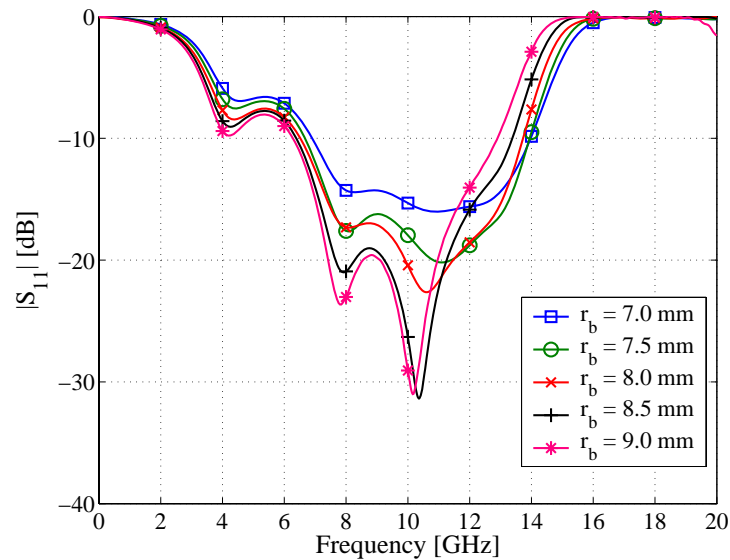


Fig. 5.12. Comparison of reflection coefficients caused by adding ideal first order matching sections to an electrically large ( $r_p = 31.5$  mm) 10-way combiner, containing a -28 dB conical line taper, for different backshort lengths.

the input matching section is included in the design, since the matching section has an effect on the reflection coefficient of the combiner.

## 5.4 Summary of General Design Guidelines and Critical Evaluation of Previous Designs

In this chapter some general design guidelines have been developed for the design of  $N$ -way conical transmission line power combiners. A short summary of these findings will be given in this section, as well as a critical evaluation of the designs in Chapters 3 and 4 against these general design guidelines.

### 5.4.1 Summary of General Design Guidelines

The most important parameter to determine in the design is the radial size of the combiner. The minimum radial size is determined by the circumference needed to support the  $N$  input connectors. The maximum size of the combiner is determined by the cutoff radius of the  $TE_{N/2,1}$  mode at the centre frequency, or for uneven numbers of input ports a linear interpolation is used between the cutoff radii of the  $TE_{(N+1)/2,1}$  and the  $TE_{(N-1)/2,1}$  modes. If the structure is kept smaller or about the same size as this cutoff radius, very predictable reflection and transmission performance can be expected from the combiner when using a taper with a return loss better than  $-25$  dB, and well matched first order peripheral port matching sections. Note that slightly mismatched peripheral ports may give undesired degradation of the reflection performance, and care should be taken to ensure a good match of the peripheral ports. For wider bandwidth applications optimisation of these matching sections may be performed as shown in Section 3.5.1.

When a structure larger than about 1.3 times the cutoff radius of the  $TE_{N/2,1}$  mode is required, more care must be taken in the design to ensure that the reflection performance of the structure is still adequate. If the resonant mode causing the transmission zero is known, normally by simulation, the maximum size of the combiner can be approximated by the technique in Section 4.2.1. A taper with a return loss of at least  $-25$  dB should be used, and careful simulation of the structure should be performed after the peripheral port matching sections are included to find a backshort length that will give good reflection performance at the desired frequency. This may be necessary when a longer section of conical line is required for the impedance taper in order to allow adequate spacing between the conductors of the central coaxial line. Normally this will only happen in structures with fewer than about 16 input ports (depending on the impedance level required at the central port), since the return loss of the Klopfenstein taper is more dependent on the length of the line than the impedance step required, due to the log-

arithmic impedance dependence seen in (4.9). When more than 16 ports are used, the cutoff radius is generally large enough to accommodate an adequate length of tapered line to raise the impedance at the central port sufficiently with a good return loss.

#### 5.4.2 Critical Evaluation of Previous Designs

The first design in Chapter 3 is very simple, since no impedance taper was included in the conical line, and optimisation was used for the central as well as the peripheral port matching sections. A  $5\ \Omega$  conical line was used to match the ten  $50\ \Omega$  input feeds. The radial size of the combiner was simply determined by the minimum size required to fit the ten peripheral SMA connectors. The total radial size of the combiner, after tuning of the backshort length, is  $r_{\max} = 32.6\ \text{mm}$ , with  $r_b = 7.6\ \text{mm}$  for 10 GHz operation. This is 1.3 times the cutoff radius of the  $\text{TE}_{51}$  mode, and it can be seen in Fig. 3.10 that the reflection coefficient displays the characteristic knee at the high frequency side of the reflection zero. This is consistent with the results in Table 5.3, where the reflection performance of 10-way combiners is shown to start degrading at around 1.2 to 1.3 times the size of the cutoff radius. Optimisation was used to design both the central and the peripheral matching networks to obtain wide band performance. The performance of the constructed combiner was not as good as expected due to the imperfect manufacturing of the narrow spacings between the central conductors, and therefore the impedance of the central part of the conical line should be raised.

The design in Chapter 4 was done for a combiner with a much larger radius than the cutoff radius of the  $\text{TE}_{51}$  mode. This large radial size requirement is due to the  $25\ \Omega$  impedance needed at the central port, and the length of the Klopfenstein taper needed to achieve this. An estimate of the maximum radial size was calculated with the technique in Section 4.2.1, and used as the radial size of the structure. The best taper that could be fit into the structure was employed ( $-28\ \text{dB}$  return loss), and simple non-ideal first order peripheral port matching sections were used due to limitations on the available SMA connectors. A parameter sweep was performed in CST-MWS to find the value of  $r_b$  that gives the best reflection performance, and an optimised central port matching section was included in the final design. Note that although this method of design still gives satisfactory results, more full wave simulation is required to get the final parameters, and the design is therefore more time consuming than the design of an electrically small combiner.

## 5.5 Design and Simulation of a 30-Way Combiner

Using all the design guidelines developed in this chapter, a 30-way combiner is designed in this section to operate at 12.5 GHz in order to be comparable to the results for a 30-way radial combiner published in [3]. The design in [3] relies on circuit models to find the basic dimensions of the structure, and full wave simulation optimisation to achieve a wide band performance for the combiner. The design here will attempt to achieve similar or better performance than the published results, with far less design effort and full wave optimisation.

For this design the first order peripheral port matching sections described in Section 4.1 are used in order to keep the design as simple as possible. If the structure is found to be electrically small the ideal matching section should be employed, as explained in the previous section.

As a first step, the cutoff radius of the  $TE_{15,1}$  mode is found at 12.5 GHz from (2.140) as 57.3 mm. The same result is also found when (5.1) is used. The minimum radius needed to accommodate 30 SMA connectors is about 47 mm which, when using (4.7) with  $\delta_s = 6$  mm, easily allows for a taper of 33 mm. The impedance of the conical line in the combiner at the peripheral ports is  $Z_0 = 85.6/30 = 2.85 \Omega$  in order to accommodate ideal first order peripheral matching sections. A Klopfenstein taper matching  $2.85 \Omega$  to  $25 \Omega$  over a length of 33 mm has a return loss of better than -35 dB when the minimum frequency is chosen as 7 GHz. Since the match is so good, the minimum frequency of the match can be chosen almost freely as long as it is lower than the expected minimum operating frequency of the combiner, which is around 10.5 GHz in this case. With this excellent return loss achieved by the taper, the size determined by the minimum circumference needed to accommodate the input ports can be used as the size of the structure, which is much smaller than the cutoff radius of the  $TE_{15,1}$  mode at 12.5 GHz.

The Klopfenstein taper is again approximated in the conical line by 1 mm straight line sections, and the edges smoothed in the same manner as described in Section 4.2.2. Ideal first order matching sections are included at the peripheral ports, as described in Section 4.1, with the diameter of the airline  $c = 5.16$  mm, and the length of the partially filled line  $l_t = 4.51$  mm for operation at 12.5 GHz. The length of the quarter wavelength  $85.6 \Omega$  airline is  $l_a = 6.0$  mm. The backshort length is initially chosen as  $r_b = 5.4$  mm, which is about 10 % shorter than the theoretical value of 6 mm, as suggested by Tables 5.1 and 5.2. This produces a centre frequency of about 12.0 GHz, which is moved to 12.5 GHz by decreasing  $r_b$  by the factor  $12.0/12.5$  to  $r_b = 5.2$  mm. A CST-MWS screen shot of the simulation model is shown in Fig. 5.13 and the simulated reflection coefficient is shown in Fig. 5.14.

An optimised tapered coaxial line matching section, like the one described in Section 4.3.2, is used in the central coaxial line of the combiner to match the structure to  $50 \Omega$  over a wide

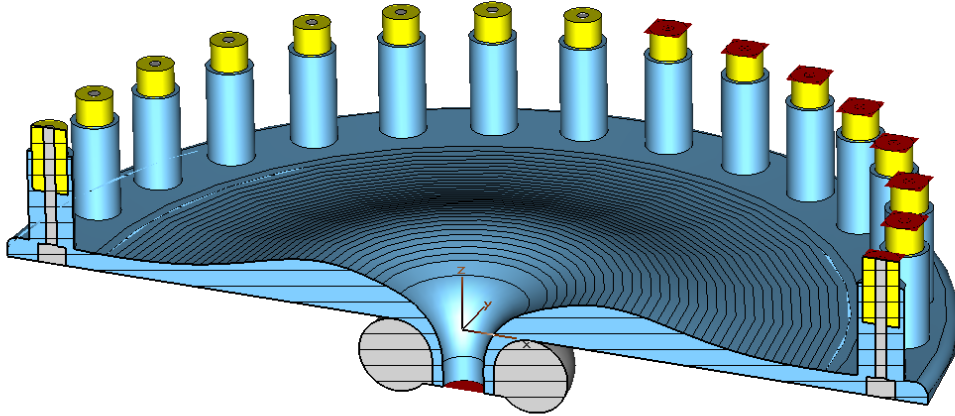


Fig. 5.13. CST-MWS screen shot of tapered 30-way combiner showing central conical to coaxial transition and peripheral feeding lines and ports. The background material as well as the grey parts are PEC, the blue part is vacuum, and the yellow parts are teflon. Ports are represented by red rectangles.

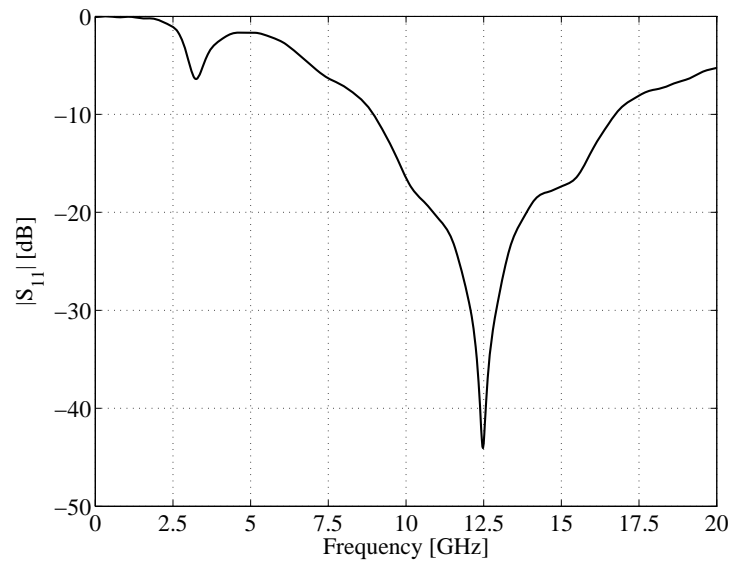


Fig. 5.14. Common central port reflection coefficient of a tapered 30-way combiner with the peripheral input matching sections included.

band. Fig. 5.15 shows a comparison of the MATLAB prediction of the reflection coefficient to the CST-MWS simulation of the entire combiner, including the central coaxial matching section. Excellent agreement between the simulated results is demonstrated in Fig. 5.15, and a  $-20$  dB

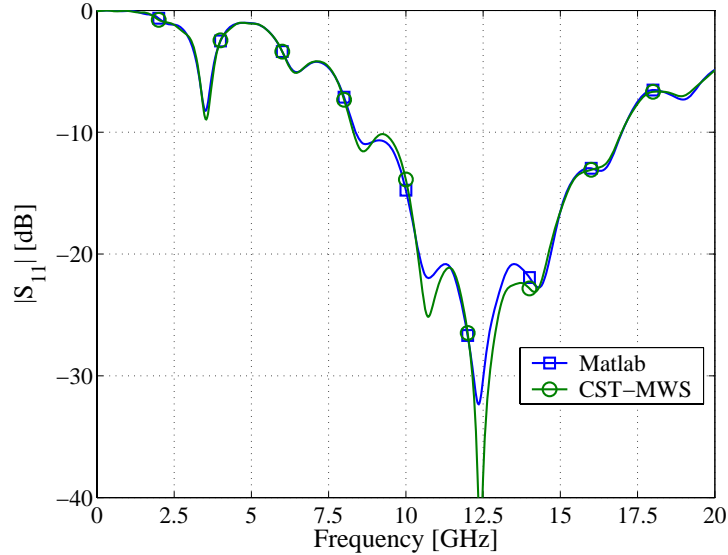


Fig. 5.15. Comparison of the simulated reflection coefficients of a matched 30-way tapered line conical power combiner.

matched bandwidth of 34% is achieved around 12.5 GHz. It was shown in Fig. 4.19 that good agreement between measured and simulated reflection can be expected for this type of combiner down to about  $-20$  dB. The simulated reflection performance of this 30-way combiner is superior to the performance of the 30-way radial combiner in [3], which demonstrates a 25% bandwidth with a return loss of  $-14$  dB at 12.5 GHz. The  $-14$  dB return loss bandwidth of the combiner designed here is 40% at 12.5 GHz.

It should be noted here that, depending on the required bandwidth of the combiner, other matching techniques could have been used. For wider bandwidth operation optimised stepped impedance networks could have been used as the central and peripheral matching sections. For narrower bandwidth applications the Klopfenstein taper could also have been used in the conical line to raise the impedance to the required  $50 \Omega$  at the central port. This can be done because of the long length of conical line available in the combiner. Bandwidths similar to the one demonstrated in Fig. 5.14 can be achieved in this manner, with the advantage that no optimisation is required in the design. When this technique is used, however, care should be taken to check that the higher order modes described in Section 4.2.3, and particularly those in Fig. 4.10, are not excited in the high impedance part of the conical line.

A simulated transmission coefficient of the combiner is shown in Fig. 5.16 which, from (3.4), displays the expected  $-14.8$  dB transmission coefficient of a 30-way combiner in the 10.5–

14.5 GHz band.

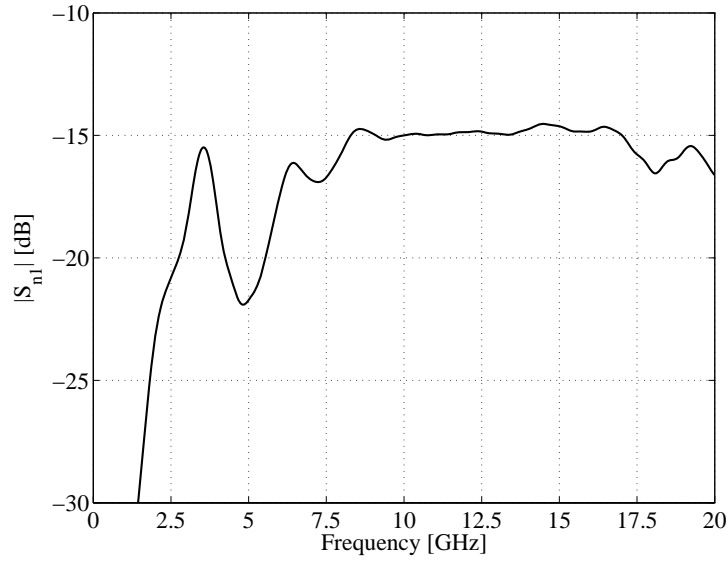


Fig. 5.16. Simulated transmission coefficient of a 30-way conical line combiner.

The minimum simulated isolation between port 2 and port  $n$  in the band 10.5–14.5 GHz is shown in Fig. 5.17. The worst isolation is between neighbouring and opposite ports, and also between

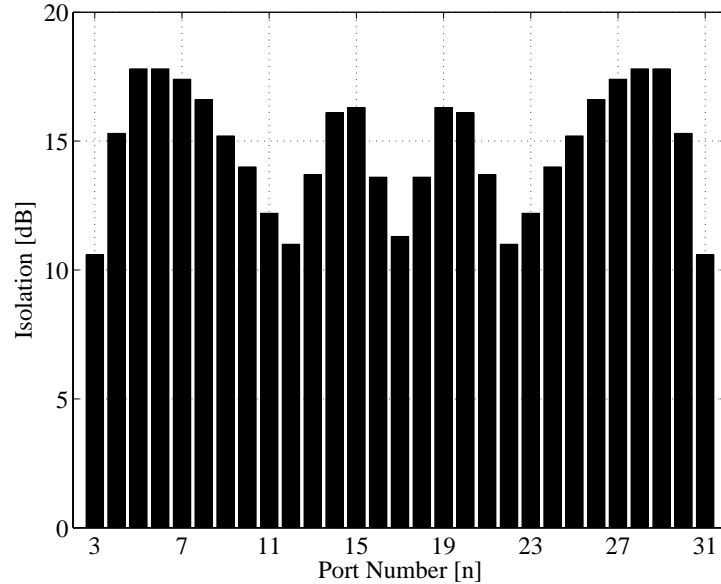


Fig. 5.17. Simulated minimum isolation between port 2 and port  $n$  in the band 10.5–14.5 GHz of a 30-way conical combiner. The same port numbering convention is used as in Fig. 3.5.

ports 2 and 12 (the exact same results are also valid for a number of other port combinations due to the symmetry of the structure). The same numbering convention is used as in Fig. 3.5. Again this is confirmed, by using the same argument as in Sections 3.8 and 4.6, by studying the zero-time H-field pattern at 12.5 GHz shown in Fig. 5.18 and the time averaged H-field strength

shown in Fig. 5.19. The fields in the vicinity of ports 3, 12 and 17 are seen to closely resemble

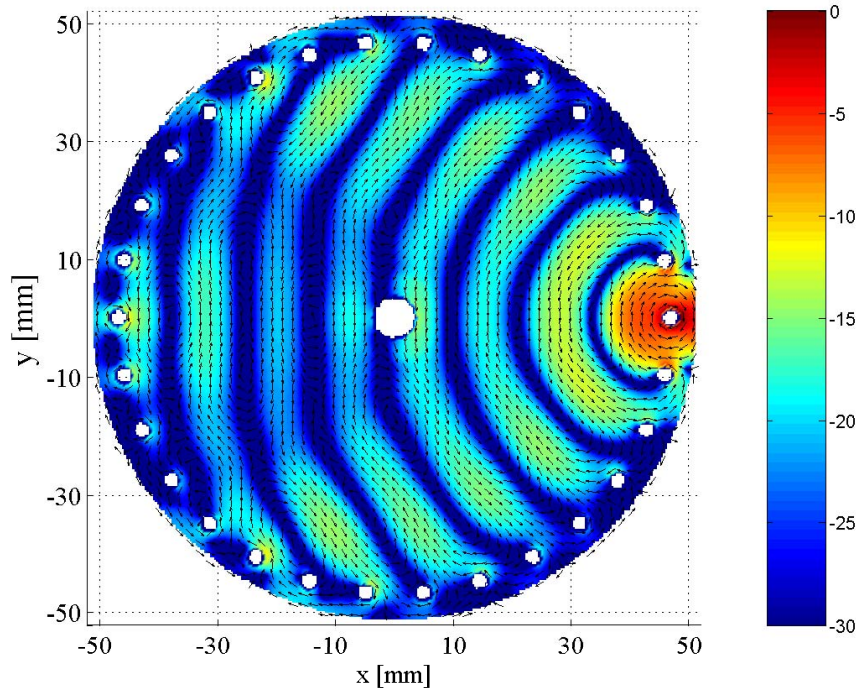


Fig. 5.18. Normalised absolute value (in dB) and direction of the simulated H-field at zero-time in a 30-way tapered line conical combiner at 12.5 GHz when port 2 (see Fig. 3.5) is driven and the other ports are terminated.

the normal TEM H-field in a coaxial line and they also have a high average value when compared to the fields in the vicinity of the other ports.

It is worth noting that, as expected from (3.6) and stated in [6], the isolation is much better than that of a 10-way combiner (see Figs. 3.21 and 4.21). The isolation results are somewhat worse than the isolation results in [3] for a similar 30-way radial combiner. It is not clear, however, if the isolation results given in [3] are for the minimum, average, maximum, or centre frequency isolation. As seen in the isolation plots in Figs. 3.21 and 4.21, and explained in Sections 3.8 and 4.6, the isolation can vary significantly with frequency over the operating band, and it is therefore impossible to properly compare the results if it is not known which isolation results are given in the literature.

## 5.6 Conclusion

In this chapter a general technique for the design of  $N$ -way conical transmission line combiners has been presented. The technique is developed by a detailed study of the main design parameters to find the limitations on the design of conical combiners. Designs of previous chapters are

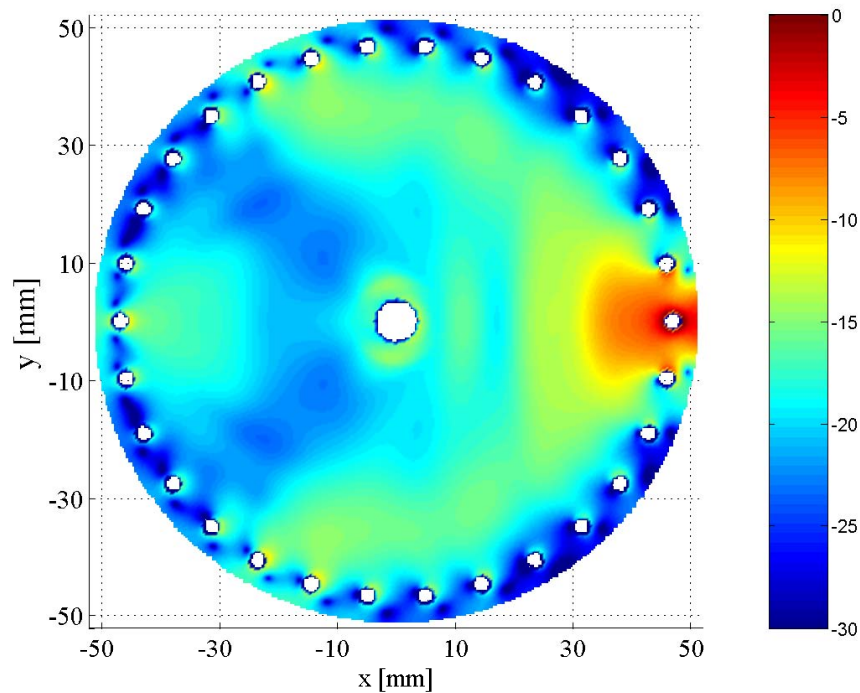


Fig. 5.19. Normalised absolute value (in dB) of the time averaged simulated H-field in a 30-way tapered line conical combiner at 12.5 GHz when port 2 (see Fig. 3.5) is driven and the other ports are terminated.

critically compared to these new guidelines.

A 30-way combiner was designed and simulated to show that the design techniques developed in this dissertation can be used with confidence to design combiners with many ports and excellent performance. The simulated results obtained for a 30-way conical combiner designed in this manner were compared to published results for a similar 30-way radial combiner, and the performance of the conical combiner is in the same order (in the case of the isolation), or better than (in the case of the reflection), that of the radial combiner. Much less design effort, and also fewer full wave simulations, are needed in the design of the conical combiner. Only analytical models have to be optimised to find the desired wide band performance, and excellent agreement between the analytical model and the full wave simulation is achieved.

# Chapter 6

## Conclusion

This dissertation presented a complete design technique for the design of reactive  $N$ -way conical transmission line power combiners. These combiners offer significant advantages over the more widely used radial line types in terms of design simplicity and performance.

A complete theoretical description of conical transmission lines is presented, starting with the analytical solutions of the Maxwell equations in spherical coordinates with conical boundary conditions. A method for the computation of the roots required for the evaluation of these equations is given. The phenomenon of a gradual cutoff wavelength of the higher order modes in conical lines is explained, and a simple proof is presented for the choice of the equation for the cutoff wavelength given by standard texts. Some plots of the analytical solutions of the modal fields are shown, as well as comparisons with simulated results.

Two  $X$ -band 10-way conical combiners were designed and manufactured. The first has a constant impedance conical line in the combining structure, matched by optimised stepped impedance coaxial lines on the input and output sides. A 74% bandwidth is achieved with a return loss of -14.5 dB. The second combiner has a tapered conical line in the combining structure and employs an optimised coaxial taper as the matching section in the output feed line. These changes were made to alleviate some construction difficulty encountered in the first design, and also to allow for higher peak power handling capability. The constructed combiner demonstrates a 47% bandwidth with a -18.5 dB return loss.

The final part of the dissertation concentrates on finding the limitations of the previously presented design techniques, and expands them to include the design of general  $N$ -way combiners. To demonstrate the technique, a 30-way combiner is designed at  $K_u$ -band, and simulated results show a -20 dB return loss bandwidth of 34%.

The design technique presented is simple to execute and requires minimal full wave analyses

of the structure. Only circuit models need to be optimised to achieve broadband operation. Simulated results are in good agreement with measurements, and the design technique can be used with confidence to design combiners with a large number of input ports ( $N \geq 8$ ) at microwave frequencies up to the  $K_u$ -band.

Expansions on this work anticipated by the author could include:

- A study on techniques for improving the isolation of mainly small combiners ( $N < 16$ ).

These will typically include introducing lossy materials into the structure to absorb higher order modes, or employing isolation resistors between the input ports. This will, however, probably reduce the operating bandwidth and power handling capability of the combiner.

- Introducing waveguide instead of coaxial ports.

For very high power applications the power handling capability of the combiner might be limited by the power handling capability of the coaxial connectors used at the input and output ports. Also, in many high power systems waveguide is used extensively as transmission medium, and transitions to coaxial lines can cause unwanted reflections and thus degrade system performance. The matching can still be done in coaxial lines, as described in the dissertation, but instead of using coaxial connectors as the input and output ports, the coaxial feed lines could transition directly into the required waveguide.

- Using back-to-back combiners in a high power amplifier system.

By placing two combiners back-to-back, and replacing the peripheral ports by amplifier modules, a fully integrated high power amplifier, such as the one described in [3], can be constructed.

# Appendix A

## Derivatives of Some Special Functions

### A.1 Derivatives of the Associated Legendre Functions

The first derivative of the associated Legendre functions, denoted by  $X_\nu^m(z)$  [for either  $P_\nu^m(z)$  or  $Q_\nu^m(z)$ ], is given by [25]

$$\frac{d}{dz}X_\nu^m(z) = \frac{1}{z^2-1} [\nu z X_\nu^m(z) - (\nu+m)X_{\nu-1}^m(z)]. \quad (\text{A.1})$$

When the argument is replaced by  $\cos \theta$ , the  $\theta$ -derivative can be found by using the chain rule of differentiation as

$$\frac{d}{d\theta}X_\nu^m(\cos \theta) = \frac{1}{\sin \theta} [\nu \cos \theta X_\nu^m(\cos \theta) - (\nu+m)X_{\nu-1}^m(\cos \theta)]. \quad (\text{A.2})$$

### A.2 Derivatives the Modified Spherical Bessel Functions

The first derivative of the Bessel or Hankel functions, denoted by  $B_\nu(\beta r)$  [for either  $J_\nu(\beta r)$ ,  $Y_\nu(\beta r)$ ,  $H_\nu^{(1)}(\beta r)$  or  $H_\nu^{(2)}(\beta r)$ ], is given by [21]

$$\frac{d}{dr}[B_\nu(\beta r)] = \beta B_{\nu-1}(\beta r) - \frac{\nu}{r}B_\nu(\beta r). \quad (\text{A.3})$$

Using the product rule for differentiation and (A.3), the first and second derivatives of the modified spherical Bessel functions are found, from the definition given by (2.64), as

$$\frac{d}{dr}\hat{B}_\nu(\beta r) = \sqrt{\frac{\pi\beta}{8r}}B_{\nu+1/2} + \sqrt{\frac{\pi\beta r}{2}} \left[ \beta B_{\nu-1/2}(\beta r) - \frac{\nu+1/2}{r}B_{\nu+1/2}(\beta r) \right] \quad (\text{A.4})$$

and

$$\begin{aligned}
\frac{d^2}{dr^2} \hat{B}_\nu(\beta r) &= -\sqrt{\frac{\pi\beta}{32r^3}} B_{\nu+1/2}(\beta r) + \sqrt{\frac{\pi\beta}{8r}} \frac{d}{dr} B_{\nu+1/2}(\beta r) + \sqrt{\frac{\pi\beta r}{2}} \beta \frac{d}{dr} B_{\nu-1/2}(\beta r) \\
&\quad - \sqrt{\frac{\pi\beta r}{2}} (\nu + 1/2) \left[ \frac{-1}{r^2} B_{\nu+1/2}(\beta r) + \frac{1}{r} \frac{d}{dr} B_{\nu+1/2}(\beta r) \right] \\
&\quad + \sqrt{\frac{\pi\beta}{8r}} \beta B_{\nu-1/2}(\beta r) - \sqrt{\frac{\pi\beta}{8r}} \frac{(\nu + 1/2)}{r} B_{\nu+1/2}(\beta r).
\end{aligned} \tag{A.5}$$

# Bibliography

- [1] Kenneth J. Russel, “Microwave power combining techniques,” *IEEE Transactions on Microwave Theory and Techniques*, vol. MTT-27, no. 5, pp. 472–478, May 1979.
- [2] Kai Chang and Cheng Sun, “Millimeter-wave power-combining techniques,” *IEEE Transactions on Microwave Theory and Techniques*, vol. MTT-31, no. 2, pp. 91–107, Feb. 1983.
- [3] Aly E. Fathy, S. W. Lee, and David Kalokitis, “A simplified design approach for radial power combiners,” *IEEE Transactions on Microwave Theory and Techniques*, vol. 54, no. 1, pp. 247–255, Jan. 2006.
- [4] Gerald W. Swift and David I. Stones, “A comprehensive design technique for the radial wave power combiner,” *IEEE MTT-S Int. Microwave Symp. Dig.*, pp. 279–281, May 1988.
- [5] Marek E. Bialkowski and V. P. Waris, “Electromagnetic model of a planar radial-waveguide divider/combiner incorporating probes,” *IEEE Transactions on Microwave Theory and Techniques*, vol. 41, no. 6/7, pp. 1126–1134, June/July 1993.
- [6] S. Nogi, F. Okazaki, and K. Fukui, “A broadband conical-radial wave power divider/combiner,” *Asia Pacific Microwave Conference*, pp. 507–510, Dec. 1994.
- [7] E. Belohoubek, R. Brown, H. Johnson, A. Fathy, D. Bechtle, D. Kalokitis, and E. Mykietyn, “30-way radial power combiner for miniature GaAs FET power amplifiers,” *IEEE MTT-S Int. Microwave Symp. Dig.*, pp. 515–518, June 1986.
- [8] N. Marcuvitz, *Waveguide Handbook*, Peter Peregrinus, London, 1986.
- [9] Simon Ramo, John R. Whinnery, and Theodore Van Duzer, *Fields and Waves in Communication Electronics*, John Wiley and Sons, 3rd edition, 1994.
- [10] Robert Lehmensiek and P.W. van der Walt, “A compact, high-power, low-loss, *L*-band coaxial 18-way power divider/combiner,” *Microwave and Optical Technology Letters*, vol. 16, no. 4, pp. 241–243, Nov. 1997.
- [11] Robert S. Harp and Kenneth J. Russel, “Conical power combiner,” U.S. Patent 4 188 590, Feb. 1980.

- [12] P. W. van der Walt, "A novel matched conical line to coaxial line transition," *Proceedings of the South African Symposium on Communications and Signal Processing*, pp. 431–434, Sept. 1998.
- [13] J. P. Quine, J. G. McMullen, and D. D. Khandelwal, "Ku-band IMPATT amplifiers and power combiners," *IEEE MTT-S Int. Microwave Symp. Dig.*, pp. 346–348, June 1978.
- [14] Dirk I. L. de Villiers, P.W. van der Walt, and Petrie Meyer, "Design of a ten-way conical transmission line power combiner," *IEEE Transactions on Microwave Theory and Techniques*, vol. 55, no. 2, pp. 302–308, Feb. 2007.
- [15] Dirk I.L. de Villiers, P.W. van der Walt, and Petrie Meyer, "Design of conical transmission line power combiners using tapered line matching sections," *Submitted to IEEE Transactions on Microwave Theory and Techniques*.
- [16] Dirk I.L. de Villiers, P.W. van der Walt, and Petrie Meyer, "Design constraints in conical line power combiners," *To be Submitted to the Microwave and Optical Technology Letters*.
- [17] Dirk I.L. de Villiers and Petrie Meyer, "On the numerical calculation of analytic solutions for higher-order modes in conical lines," *To be submitted to the International Journal of RF and Microwave Computer-Aided Engineering*.
- [18] S.A. Schelkunoff, "Transmission theory of spherical waves," *AIEE transactions*, vol. 57, pp. 744–750, 1938.
- [19] S. A. Schelkunoff, *Electromagnetic Waves*, Van Nostrand, Princeton, 1943.
- [20] R. F. Harrington, *Time-Harmonic Electromagnetic Fields*, McGraw-Hill, New York, 1961.
- [21] Constantine A. Balanis, *Advanced Engineering Electromagnetics*, John Wiley and Sons, New York, 1989.
- [22] C. M. Weil, B. F. Riddle, D. R. Novotny, and R. T. Johnk, "Modal cutoff in coaxial transmission lines of conical and cylindrical geometries," *IEEE MTT-S Int. Microwave Symp. Dig.*, vol. 2, pp. 1229–1232, May 2001.
- [23] S. A. Schelkunoff, "Theory of antennas of arbitrary size and shape," *Proceedings of the I.R.E.*, vol. 29, pp. 493–521, Sept. 1941.
- [24] Constantine A. Balanis, *Antenna Theory: Analysis and Design*, John Wiley and Sons, New York, 2nd edition, 1982.
- [25] M. Abramowitz and I.A. Stegun, Eds., *Handbook of Mathematical Functions with Formulas, Graphs and Mathematical Tables*, U.S. Gov. Printing Office, Washington D.C., 1966.

- [26] M. R. Spiegel, *Mathematical Handbook of Formulas and Tables*, Schaum's Outline Series. McGraw-Hill, 1968.
- [27] F.W.J. Olver, *Asymptotics and Special Functions*, Academic Press, Inc., 111 Fifth Avenue, New York, New York 10003, 1974.
- [28] F.W.J. Olver and J.M. Smith, "Associated Legendre functions on the cut," *Journal of Computational Physics*, vol. 51, pp. 502 – 518, 1983.
- [29] Shanjie Zhang and Jianming Jin, *Computation of Special Functions*, John Wiley and Sons, Inc., New York, 1996.
- [30] S. A. Schelkunoff, *Advanced Antenna Theory*, Applied Mathematics Series. John Wiley and Sons, New York, 1952.
- [31] C. H. Papas and R. King, "Input impedance of wide-angle conical antennas fed by a coaxial line," *Proceedings of the I.R.E.*, vol. 37, pp. 1269–1271, Nov. 1949.
- [32] L. J. Chu, "Physical limitations of omni-directional antennas," *Journal of Applied Physics*, vol. 19, no. 12, pp. 1163–1175, Dec. 1948.
- [33] L. B. Felsen and N. N. Marcuvitz, *Radiation and Scattering of Waves*, IEEE Press, 1994.
- [34] D. G. Zill and M. R. Cullen, *Advanced Engineering Mathematics*, Jones and Bartlett, Boston, 2nd edition, 2000.
- [35] C. R. Wylie and L. C. Barret, *Advanced Engineering Mathematics*, McGraw-Hill, 6th edition, 1995.
- [36] M. Cohn, B. D. Geller, and J. M. Schellenberg, "A 10 watt broadband FET combiner/amplifier," *IEEE MTT-S Int. Microwave Symp. Dig.*, pp. 292–297, June 1979.
- [37] I. Stones, J. Goel, and G. Oransky, "An 18 GHz 8-way radial combiner," *IEEE MTT-S Int. Microwave Symp. Dig.*, pp. 163–165, 1983.
- [38] A. E. Fathy and D. Kalokitis, "A simplified approach for the design of radial power combining structures," *IEEE MTT-S Int. Microwave Symp. Dig.*, vol. 1, pp. 73–76, 2004.
- [39] Marek E. Bialkowski and V. P. Waris, "Analysis of an N-way radial cavity divider with a coaxial central port and waveguide output ports," *IEEE Transactions on Microwave Theory and Techniques*, vol. 44, no. 11, pp. 2010–2016, Nov. 1996.
- [40] N. Okubo, Y. Kaneko, T. Saito, and Y. Tokumitsu, "A 6-GHz 80-W GaAs FET amplifier with TM-mode cavity power combiner," *IEEE MTT-S Int. Microwave Symp. Dig.*, pp. 276–278, 1983.

- [41] G. Matthaei, L. Young, and E. M. T. Jones, *Microwave Filters, Impedance Matching Networks, and Coupling Structures*, Artech House, 1980.
- [42] J. F. Liang, H. C. Chang, and K. A. Zaki, "Coaxial probe modeling in waveguide and cavities," *IEEE Transactions on Microwave Theory and Techniques*, vol. MTT-40, no. 12, pp. 2172–2180, 1992.
- [43] R. E. Collin, *Field Theory of Guided Waves*, IEEE Press, New York, 2nd edition, 1991.
- [44] D. M. Pozar, *Microwave Engineering*, John Wiley and Sons, New York, 2nd edition, 1998.
- [45] P. I. Somlo, "The computation of coaxial line step capacitances," *IEEE Transactions on Microwave Theory and Techniques*, vol. MTT-15, no. 1, pp. 48–53, Jan. 1967.
- [46] E. Weber, *Electromagnetic Fields: Theory and Applications*, vol. I—Mapping of Fields, John Wiley and Sons, New York, 1950.
- [47] R. W. Klopfenstein, "A transmission line taper of improved design," *Proceedings of the IRE*, vol. 44, pp. 31–35, Jan. 1956.
- [48] R. E. Collin, "The optimum tapered transmission line matching section," *Proceedings of the IRE*, vol. 44, no. 4, pp. 539–548, Apr. 1956.
- [49] Milton A. Grossberg, "Extremely rapid computation of the Klopfenstein impedance taper," *IEEE Proceedings*, vol. 56, no. 9, pp. 1629–1630, Sept. 1968.
- [50] Rudolf P. Hecken, "A near-optimum matching section without discontinuities," *IEEE Transactions on Microwave Theory and Techniques*, vol. MTT-20, no. 11, pp. 734–739, Nov. 1972.
- [51] Johannes H. Cloete, "Computation of the Hecken impedance function (Letters)," *IEEE Transactions on Microwave Theory and Techniques*, vol. MTT-25, no. 5, pp. 440–440, May 1977.
- [52] Huber+Suhner AG, Coaxial Connector Department, 9100 Herisau, Switzerland, *Suhner Coaxial Connectors General Catalogue*.